Non-steady-state photo-electromotive force effect induced by one-dimensional periodical light distributions and its applications to Talbot interferometry

by

M. C. Ileana Guízar Iturbide

Thesis submitted in partial fulfillment of the
requirement for the degree of

**DOCTOR EN CIENCIAS EN LA
ESPECIALIDAD DE ÓPTICA**

in

**Instituto Nacional de Astrofísica,
Óptica y Electrónica**

November 2011
Tonantzintla, Puebla.

Supervisors:
Dra. Svetlana Mansurova
Dr.Ponciano Rodríguez Montero

Dedicatoria

Dedico este trabajo a mi familia por todo el apoyo y los consejos que siempre me han dado.

Agradecimientos

Agradezco a mis asesores: Dra. Svetlana Mansurova y al Dr. Ponciano Rodríguez Montero quienes me apoyaron de manera incondicional durante todos estos años para realizar los experimentos que se explican en este trabajo y para la escritura del mismo.

Agradezco a mis sinodales, personal administrativo y demás personal que labora en este instituto, que de alguna manera u otra me ayudaron a la realización de este trabajo. En particular agradezco a las secretarias de la coordinación de óptica y de formación académica quienes siempre me ayudaron y fueron muy amables conmigo.

Agradezco a mis colegas y amigos el apoyo brindado (en lo profesional y lo personal), sus enseñanzas, el tiempo, la paciencia, sus comentarios y sus sugerencias.

Finalmente agradezco al Instituto Nacional de Astrofísica, Óptica y Electrónica (I.N.A.O.E.) y al Consejo Nacional de Ciencia y Tecnología (CONACyT) por el apoyo económico brindado a través de la beca No. 182787 para realizar esta Tesis de Doctorado.

Table of contents

Chapter 1

Introduction

1.1 Introduction ……………………………………………………………..1

1.2 References …………………………………………………………………6

Chapter 2

Literature review

2.1 Introduction ……………………………………………………………..9

2.2 Interference …………………………………………………………….9

2.1.1 Interference of two waves ………………………………………...10

2.3 Diffraction …………………………………………………………….…...12

2.3.1 Huygens-Fresnel principle ………………………………………..12

2.3.2 The Fresnel approximation ………………………………………..14

2.3.3 The Fraunhofer approximation …………………………………....14

2.3.4 Talbot effect …………………………………………………………15

2.4 CCD-based techniques for analysis of contrast ………………………..21

2.4.1 Contrast ……………………………………………………………...21

2.4.2 CCD-based methods ………………………………………………...22

2.4.2.1 Root Mean Square (RMS) ………………………………..22

2.4.2.2 Semivariogram method …………………………………...23

2.5 Basic principles of non-steady-state photo-electromotive force (photo-EMF) effect …………………………………………………………………...25

2.5.1 General description ……………………………………………………..25

2.5.2 Main equations of the theoretical description of the photo-EMF effect in monopolar photoconductor ……………………………………28

2.5.3 Photo-EMF current amplitude ……………………………………29

2.6 References ……………………………………………………………...34

Chapter 3

Experimental methods

3.1 Introduction ……………………………………………………………40

3.2 Description of experimental setup for self-images generation ………...40

3.3 Characterization of adaptive photodetectors …………………………..42

3.4 Description of detection system of self-images …………………………44

3.4.1 CCD ……………………………………………………………….45

3.4.2 Photo-EMF ……………………………………………………….46

3.4.2.1 Characterization of the piezo-electric ……………………47

3.5 Description of detection system of self-images for turbid media ……...50

3.6 Analysis of diffraction orders collected by system ……………………..51

3.7 References ……………………………………………………………...52

Chapter 4

Non-steady-state photo-EMF effect induced by an arbitrary periodical one-dimensional light pattern

4.1 Introduction ……………………………………………………………54

4.2 Theoretical analysis …………………………………………………...54

4.2.1 Incident light distribution …………………………………………54

4.2.2 Main equations of the theoretical description of the photo-EMF effect in monopolar photoconductor ……………………………………56

4.2.3 Solution in linear approximation …………………………………57

4.2.4 Steady-state solution ……………………………………………...57

4.2.5 Solution for the first temporal harmonics ………………………...58

4.2.6 Photo-EMF current density ………………………………………59

4.2.7 Analysis of the dynamics of photo-EMF current in the presence of multiple spatial harmonics ……………………………………………...60

4.3 Graphs of the limiting cases ……………………………………………..65

4.4 Theoretical analysis of axial distribution of the photo-EMF current produced by light pattern generated by diffraction on binary grating on near field …………………………………………………………………...67

4.5 Experimental results of axial distribution of the photo-EMF current produced by light pattern generated by diffraction on binary grating on near field detectors ………………………………………………...………72

4.5.1 Experimental results of adaptive photodetector …………………..73

4.6 References …………………………………………………………...80

Chapter 5

Comparative analysis: photo-EMF versus CCD methods

5.1 Introduction …………………………………………………………81

5.2 Theoretical comparison of axial dependence of contrast distribution evaluated by RMS, semivariogram, and photo-EMF effect ……………………………………………………………………………82

5.2.1 Numerical simulation of diffraction intensity distributions generated by binary grating …………………………………………………..82

5.2.2 Axial dependence of contrast using RMS and semivariogram methods ………………………………………………………………84

5.2.3 Axial dependence of contrast using photo-EMF effect ……………………………………………………………………...85

5.3 Experimental analysis of axial dependence of contrast distribution evaluated by RMS, semivariogram, and photo-EMF effect ……………………………………………………………………………86

5.3.1 Experimental intensity distributions generated by a binary grating ……………………………………………………………………...86

5.3.2 Experimental results in free space ………………………………...88

5.3.2.1 RMS and semivariogram methods ………………………..88

5.3.2.2 Photo-EMF ………………………………………………..90

5.3.2.3 Discussion ………………………………………………...93

5.3.3 Experimental results in turbid media ……………………………...94

5.4 References …………………………………………………………...97

Chapter 6

Displacement measurement using the adaptive photodetectors and the Talbot effect

6.1 Introduction ……………………………………………………………99
6.2 Displacement measurement by adaptive photodetector and Talbot effect ………………………………………………………………………100
6.3 Discussion ……………………………………………………………105
6.4 References ……………………………………………………………106

Chapter 7

Conclusions

7.1 Conclusions …………………………………………………………..108

List of figures

Fig. 2.1. Interference of two plane waves 10

Fig. 2.2. Intensity distribution generated for interference of two waves 11

Fig. 2.3. Diagram of Huygens-Fresnel principle 13

Fig. 2.4. Localization of Talbot image planes behind the grating 16

Fig. 2.5. Standard configuration for photo-EMF effect. Here I_1 and I_2 are the intensities of each wave, EOM is the electro-optical modulator, J^{Ω} is the photo-EMF current, U_{Ω} is the photo-EMF voltage, and R_L is the load resistor 26

Fig. 2.6. Diagram of space-charge electric field generation in non-steady-state photo-EMF effect 26

Fig. 2.7. Energy levels structure used for model of a monopolar photoconductor. The conduction band and the valence band are W_C and W_V respectively. Initial concentrations of donor and acceptor centers (for electrons) are N_D^0 and N_A^0 respectively 28

Fig. 2.8. Dependence of the photo-EMF signal versus the modulation frequency Ω 30

Fig. 2.9. Dependence of the photo-EMF signal versus the spatial frequency K ..31

Fig. 2.10. Dependence of the photo-EMF signal versus the modulation amplitude K at frequency $\Omega_0 << \Omega$ 32

Fig. 3.1. Geometry of a Ronchi grating 41

Fig. 3.2. Schematic diagram of experimental set-up for self-images generation .41

Fig. 3.3. Experimental setup for characterization of photo-EMF detectors. Here M_1 and M_2 are mirrors, BS_1 and BS_2 are beam splitters, and θ is the angle ..42

Fig. 3.4. Dimensions of adaptive photodetectors 43

Fig. 3.5 Dependence of the photo-EMF signal as a function of the beam crossing angle for crystal 1 43

Fig. 3.6. Dependence of the photo-EMF signal as a function of the beam crossing angle for crystal 2 ……………………………………………………………….44

Fig. 3.7. Schematic diagram of experimental set-up for CCD camera …………45

Fig. 3.8. Image of Talbot self-image for the binary grating recorded by CCD camera ………………………………………………………………………………46

Fig. 3.9. Details of photo-EMF based arrangement ………………………………...47

Fig. 3.10. Dependence of photo-EMF signal as a function of the Vpp. Here the wavelength $\lambda \approx 633nm$, the output power of $\approx 11mW$, and with a frequency of $600Hz$ ……………………………………………………………………………….48

Fig. 3.11. Dependence of photo-EMF signal as a function of the frequency. Here the wavelength $\lambda \approx 633nm$, the output power of $\approx 11mW$, and with amplitude of $11Vpp$ ……………………………………………………………………………..48

Fig. 3.12. Dependence of photo-EMF signal as a function of the output power. Here the wavelength $\lambda \approx 633nm$, with a frequency of $600Hz$, and with amplitude of $11Vpp$ …………………………………………………………………………..49

Fig. 3.13. Dependence of the distance between self-images versus position of the collimation lens. Here the wavelength $\lambda \approx 633nm$, the output power of $\approx 11mW$, with a frequency of $600Hz$, and with amplitude of $11Vpp$ ……………………...49

Fig. 3.14. Details of photo-EMF based arrangement with glass cell ……………51

Fig. 3.15. Diagram for calculation of the diffraction orders collected by the system ……………………………………………………………………………….52

Fig. 3.16. Diagram of the diffraction orders collected by the system …………..52

Fig. 4.1. Theoretical dependence of the photo-EMF current J_l^{Ω} amplitude versus modulation frequency Ω for different values of $KL_D = 0.1,3$ and different harmonic number $H = 1,3$ ………………………………………………………61

Fig. 4.2. Theoretical dependence of the total photo-EMF current $J_{photo-EMF}^{\Omega}$ amplitude versus modulation frequency Ω for different values of $KL_D = 0.1,3$ and different harmonic number $H = 1,3,10$ ………………………………………61

Fig. 4.3. Theoretical dependence of the photo-EMF total current $J_{photo-EMF}^{\Omega}$ versus number of harmonic l for different values of $KL_D = 0.03,0.1,1,10$ ……………...65

Fig. 4.4. Theoretical dependence of the photo-EMF total current versus spatial frequency K for different harmonic number $H=1,2,3,10$ where $L_D=1$ ………66

Fig. 4.5. Theoretical dependence of the photo-EMF current amplitude (a) versus axial position z/z_T and (b) versus KL_D for $H=1$ $(l=1)$ ………………………68

Fig. 4.6. Theoretical dependence of the photo-EMF current amplitude (a) versus axial position z/z_T and (b) versus KL_D for $H=2$ $(l=1,3)$ ……………………..69

Fig. 4.7. Theoretical dependence of the photo-EMF current amplitude versus axial position z/z_T for (a) $H=3$ $(l=1,3,5)$ and (b) $H=10$ $(l=1,3,5,\ldots 19)$ ……70

Fig. 4.8. Theoretical dependence of the photo-EMF total current versus axial position z/z_T for different values of harmonic number $H=1,2,3,10$ where $KL_D=0.1,1,3$ ……………………………………………………………...71

Fig. 4.9. Theoretical dependence of the photo-EMF current amplitude versus axial position z/z_T for different values of A_0 where $KL_D=10$ …………………72

Fig. 4.10. Experimental dependence of the photo-EMF signal versus axial position z for crystal 2 with $L_D\approx 3\mu m$. Here the wavelength $\lambda\approx 633nm$, the output power of $\approx 11mW$, with a frequency of $600Hz$, with amplitude of $11Vpp$, and the binary grating with a period of $\Lambda=100\mu m$ ……………………………74

Fig. 4.11. Experimental dependence of photo-EMF signal versus axial position z. Here the wavelength $\lambda\approx 633nm$, the output power of $\approx 11mW$, with a frequency of $600Hz$, with amplitude of $11Vpp$, and the binary grating with a period of $\Lambda=100\mu m$ ……………………………………………………………………..75

Fig. 4.12. Experimental dependence of photo-EMF signal versus axial position z in steps of $250\mu m$ for crystal 1 with $L_D\approx 40\mu m$. Here the wavelength $\lambda\approx 633nm$, the output power of $\approx 11mW$, with a frequency of $600Hz$, with amplitude of $11Vpp$, and the binary grating with a period of $\Lambda=100\mu m$ ……..76

Fig. 4.13. Experimental dependence of photo-EMF signal versus axial position z for crystal 1 with $L_D\approx 40\mu m$. Here the wavelength $\lambda\approx 633nm$, the output power of $\approx 11mW$, with a frequency of $600Hz$, with amplitude of $11Vpp$, and the binary grating with a period of $\Lambda=508\mu m$ ………………………………………………77

Fig. 4.14. Experimental dependence of the photo-EMF signal versus axial position z of two crystals with different inter-electrode distances: $1mm$ and

$2.5mm$. Here the wavelength $\lambda \approx 633nm$, the output power of $\approx 11mW$, with a frequency of $600Hz$, with amplitude of $11Vpp$, and the binary grating with a period of $\Lambda = 100\mu m$ ……………………………………………………………78

Fig. 5.1. Numerical simulations of intensity distributions generated by a binary grating which contains 3 harmonics at different positions of z-axis …………...83

Fig. 5.2. Contrast dependence versus axial position using (a) RMS and (b) semivariogram function ……………………………………………………………84

Fig. 5.3. Contrast dependence versus axial position using Eq. (4.33) for photo-EMF effect ……………………………………………………………………..85

Fig. 5.4. Experimental 1-D intensity distributions generated by a binary grating recorded by CCD at different positions of z-axis ………………………………87

Fig. 5.5. Experimental dependence of contrast estimated by (a) RMS and (b) semivariogram using the data generated by CCD camera as a function of the axial position z. Here the wavelength $\lambda \approx 633nm$, the output power of $\approx 11mW$, and the binary grating with a period of $\Lambda = 100\mu m$ ……………………………..89

Fig. 5.6. Experimental dependence of photo-EMF signal as a function of the axial position of the detector. Here the wavelength $\lambda \approx 633nm$, the output power of $\approx 11mW$, with a frequency of $600Hz$, with amplitude of $11Vpp$, and the binary grating with a period of $\Lambda = 100\mu m$ ………………………………………………92

Fig. 5.7. Experimental dependence of photo-EMF signal as a function of the axial position of the detector in turbid media. Here the wavelength $\lambda \approx 633nm$, the output power of $\approx 11mW$, with a frequency of $600Hz$ and with amplitude of $11Vpp$, and the binary grating with a period of $\Lambda = 100\mu m$ ……………………..95

Fig. 5.8. Behavior of the maximum obtained by photo-EMF signal, and the transmitted power versus milk concentration on the solution …………………..96

Fig. 6.1. Typical setup to measure distance (image from reference 11) ………..99

Fig. 6.2. The amplitude of photo-EMF signal as a function of the aperture of the diaphragm. Here the wavelength $\lambda \approx 633nm$, the output power of $\approx 11mW$, with a frequency of $600Hz$, with amplitude of $11Vpp$, and the binary grating with a period of $\Lambda = 100\mu m$ …………………………………………………………...101

Fig. 6.3. Experimental setup to measure distances or axial displacements of a mirror. Here BS is the beam splitter ……………………………………………102

Fig. 6.4. The amplitude of photo-EMF signal as a function of the mirror's position. Here the wavelength $\lambda \approx 633nm$, the output power of $\approx 11mW$, with a frequency of $600Hz$, with amplitude of $11Vpp$, and the binary grating with a period of $\Lambda = 100\mu m$ ……………………………………………………………...103

Fig. 6.5. The amplitude of photo-EMF signal as a function of the mirror's position. Here the wavelength $\lambda \approx 633nm$, the output power of $\approx 11mW$, with a frequency of $600Hz$, with amplitude of $11Vpp$, and the binary grating with a period of $\Lambda = 100\mu m$ ……………………………………………………………...104

Fig. 6.6. The amplitude of photo-EMF signal as a function of the mirror's position. Here the wavelength $\lambda \approx 633nm$, the output power of $\approx 11mW$, with a frequency of $600Hz$, with amplitude of $11Vpp$, and the binary grating with a period of $\Lambda = 100\mu m$ ……………………………………………………………...104

Chapter 1

Introduction

1.1 Introduction

The Talbot effect [1], also referred as a self-imaging phenomenon of periodic objects, states that any distribution, which is a periodic function of x and y, will be also periodic in the direction of propagation z due to Fresnel diffraction.

In recent years the Talbot effect [1] and Talbot self-images localization have received much attention, both as a fundamental optical phenomenon and because of its optical applications such as interferometry [2], nanolithography [3], spectrometry [4], and in optical metrology. In optical metrology the Talbot effect has been used for range sensing [5], for real-time depth measurement [6], for 3D contouring of diffuse objects [7], for displacement measurement [8], for profilometry by phase-shifted Talbot images [9], for measuring amplitude of vibration [10], and for evaluating focal lengths [11]. In all of these applications a grating is illuminated by monochromatic spatially coherent light in order to obtain information about range, depth or displacement.

The problem of localization and analysis of self-images is reduced to the finding the planes of maximal light pattern visibility and is the key issue in investigation of fundamental optics and proposed applications. The common approach to analyze the light pattern visibility is to use a CCD camera as an input sensor with the posterior processing of the acquired images. For a simplest case of a sinusoidal periodical pattern it is enough to know the maximum and the minimum intensity of the image in order to determine its visibility [12,13].

This standard definition of contrast has been used to analyze the effect of roughness in the self-imaging process of steel reflection grating. Talbot effect was theoretically analyzed when the grating is rough and experimentally was shown that the roughness of the surface makes the average intensity decrease exponentially with the distance [14].

There are several conventional techniques that determine the contrast of an intensity distribution generated by a periodical object, such as root mean square (RMS) method [15], histogram-based method [16,17] and semivariogram-based method [18].

The root mean square (RMS) method [15] is commonly used to evaluate the contrast in the case of a periodical pattern [19] or compound images [20] analyzing the data statistically [21]. The RMS method was employed in Ref. 21 to obtain the contrast of images, and their results support that the RMS contrast is a good indicator of the visibility of broadband images, which is in line with previous studies [20,22].

Other is the histogram-based method, which provides a global description of the statistical characters of an image. The histogram of a digital image can be represented by a graph that relations the pixels that are of the same gray level [17]. The histogram has been applied for contrast measurement of fringe patterns in the presence of noise and with patterns composed of fringes that are not straight. The method is based on fitting the histogram of the measured image to the histogram of a model function that depends on several parameters; these give information about contrast and noise level [16].

Another is the semivariogram [19] method based on estimation of the spatial variability of the intensity distribution. In the case of images obtained by CCD camera, the semivariogram function measures the spatial correlation of the image and has been employed to estimate the standard deviation of nonuniform images, besides this technique has been effectively used as a tool for determining the contrast of an intensity distribution in the presence of noise [18].

In all these techniques, a CCD camera is used to record the light patterns that are processed and analyzed in order to find the self-image position. Despite of their simplicity, all CCD–based methods share common weaknesses, namely, necessity of a filter for avoid the saturation of the camera and sensitivity to the environmental vibrations.

In this thesis only the root mean square (RMS) method and the semivariogram-based method are used to determine the contrast.

Recently it has been proposed to use the photodetector based on the non-steady-state photo-electromotive force (photo-EMF) effect for measuring the visibility and for localizing the Fresnel diffraction patterns (Talbot self-images) generated by a grating [23].

Photo-EMF effect [24] reveals itself as alternating current (ac) induced in a short-circuited photoconductive sample by a vibrating non-uniform light distribution. Standard theory developed for the simplest case of sinusoidal light pattern created by the interference of two plane waves (only one spatial harmonic being presented) predicts that the output current amplitude is proportional to the square of the light pattern visibility, which makes the photo-EMF based detector suitable for the direct measurements of the changes on the light pattern contrast.

Due to its temporal adaptability to the slow phase drifts [25], this detector posses additional robustness to the environmental vibrations. For these outstanding properties photo-EMF based detector has already been proposed for a number of practical applications such as for measuring the coherent length of several light sources [26], for sensing laser induced ultrasonic detection [27], for laser vibrometry [28], etc.

The photodetector based on photo-EMF effect was used in Ref. [23] for analyzing the Talbot effect, because it can produce an electrical current that is proportional to the square of the visibility of the Fresnel diffraction patterns. This method was employed to measure experimentally visibility in real time, with high spatial resolution, and without any signal processing.

However is necessary to perform the theoretical analysis of the photo-EMF effect induced by a periodical pattern that contains spatial harmonics, and to derive an analytical expression for complex amplitude of the photo-EMF current density in a general case of periodical light pattern containing only odd harmonics, because it does not exist, for understanding and analyzing the experimental results shown in Ref. [23].

The main objective of this thesis is the theoretical and experimental investigation of the non-steady-state photo-EMF effect induced by light distributions that contains spatial harmonics i.e. periodical one-dimensional (1-D) light patterns, and its applications to Talbot interferometry.

In order to fulfill this goal, first the theoretical analysis of non-steady-state photo-EMF current induced by an arbitrary 1-D periodical pattern using the model of monopolar photoconductor with a single impurity center is performed, and an analytical expression for complex amplitude of the photo-EMF current density in a general case of periodical light pattern containing only odd harmonics is derived.

Then, the experimental study of the non-steady-state photoelectromotive force (photo-EMF) effect in presence of spatial harmonics induced by diffraction light patterns generated by a Ronchi grating in near field is performed.

Here, the comparative analysis (theoretical and experimental) of the photo-EMF based-method against the conventional CCD-based methods (RMS and semivariogram techniques) for measuring contrast distribution is realized.

Finally, experimental demonstration of the possibility for measuring the distance of a mirror-like target by using the adaptive photodetector based on the non-steady-state photoelectromotive force effect, and the Talbot effect.

Present Ph. D. Thesis is structured on 7 Chapters:

Chapter 2 contains the literature review of the basic concepts of interference, coherence, diffraction, RMS and semivariogram based-methods, as well as that the non-steady-state photo-EMF effect.

Chapter 3 includes brief description of the detection system (experimental setups) of self-images for experiments with photo-EMF detector and CCD-based methods used in this work.

Chapter 4 is devoted to the original theoretical model for the non-steady-state photo-EMF effect induced by a periodical one-dimensional light pattern in a photoconductive sample. The expression for photo-EMF current density induced by light distribution containing only odd harmonics is derived and it is used to analyze an axial distribution of photo-EMF signal produced by light pattern generated by diffraction in binary grating on near field. Besides, experimental results of photo-EMF effect induced by light patterns produced by Fresnel diffraction on Ronchi grating using *GaAs* detector at different experimental conditions are presented.

The first part of Chapter 5 consists of the experimental results obtained with photo-EMF detector and CCD-based methods. Then numerical simulations of light patterns created in near field by the diffraction on binary grating object are performed in order to generate an input data for the three proposed methods. These data have been processed using RMS and semivariogram algorithms. In case of the photo-EMF technique the ac current induced by a specific light distribution is analytically calculated on base of the theory developed by us. Finally, the comparative analysis of the performance of the proposed method against conventional CCD-based techniques has been accomplished.

In Chapter 6 the technique based on the adaptive photo-detectors and the Talbot effect are used to measure distance or the axial shifts of a mirror-like target.

Finally in Chapter 7 the conclusions are presented.

1.2 References

---

[1] H. F. Talbot, “Facts relating to optical science No. IV”, Philos. Mag. 9, 401-407 (1836).

[2] S. P. Trivedi, S. Prakash, S. Rana, and O. Sasaki, “Real-time slope mapping and defect detection in bent plates using Talbot interferometry”, Appl. Opt. 49 (5), 897-903 (2010).

[3] X. Wan, Q. Wang, and H. Tao, “Nanolithography in the quasi-far field based on the destructive interference effect of surface plasmon polaritons”, JOSA A 27 (5), 973-976 (2010).

[4] H. L. Kung, A. Bhatnagar, and D. A. B. Miller, “Transform spectrometer based on measuring the periodicity of Talbot self-images”, Opt. Lett. 26, 1645-1647 (2001).

[5] P. Chavel P. and T. C. Strand, “Range measurement using Talbot diffraction imaging of gratings”, Appl. Opt. 26(3), 862-871 (1984).

[6] J. R. Leger and M. A. Snyder, “Real-time depth measurement and display using Fresnel diffraction and white-light processing”, Appl. Opt. 23, 1655-1670 (1984).

[7] R. Rodriguez-Vera, D. Kerr, and F. Mendoza-Santoyo, “3D contouring of diffuse objects by Talbot-projected fringes”, J. Mod. Opt. 38, 1935-1945 (1991).

[8] G. S. Spagnolo, D. Ambrosini, and D. Paoletti, “Displacement measurement using the Talbot effect with a Ronchi grating”, J. Opt. A: Pure Appl. Opt. 4, S376-S380 (2002).

[9] B. F. Oreb and R. G. Dorsch, “Profilometry by phase-shifted Talbot images”, Appl. Opt. 33, 7955-7962 (1994).

[10] S. Prakash, S. Upadhyay, and C. Shakher, “Real-time out-of-plane vibration measurement/monitoring using Talbot interferometry”, Opt. Lasers Eng. 33, 251-259 (2000).

[11] P. Singh P, M. S. Faridi, C. Shakher, and R. S. Sirohi, “Measurement of focal length with phase-shifting Talbot interferometry”, Appl. Opt. 44, 1572-1576 (2005).

[12] E. Hetch, *Optics*, Addison Wesley, 4th ed., San Francisco CA, 2002.

[13] M. Born and E. Wolf, *Principles of optics*, Cambridge University Press, 7th. ed., Cambridge, 1999.

[14] F. J. Torcal-Milla, L. M. Sanchez-Brea, and E. Bernabeu, “Talbot effect with rough reflection gratings”, Appl. Opt. 46 (18), 3668-3673 (2007).

---

[15] E. Peli, “Contrast in complex images”, J. Opt. Soc. Am. A 7 (10), 2032-2040 (1990).

[16] L. M. Sanchez-Brea, J. A. Quiroga, A. Garcia-Botella, and E. Bernabeu, “Histogram-based method for contrast measurement”, Appl. Opt. 39 (23), 4098-4106 (2000).

[17] S. Lai, and G. von Bally, “Fringe contrast evaluation by means of histograms”, in *OPTIKA ’98: 5th Congress on Modern Optics*, Proc. SPIE 3573, 384-387 (1998).

[18] L. M. Sanchez-Brea, F. J. Torcal-Milla, and E. Bernabeu, “On the standard deviation in charge-coupled device cameras: A variogram-based technique for nouniform images”, J. Electron. Imaging 11 (2), 121-126 (2002).

[19] L. M. Sanchez-Brea, F.J. Torcal-Milla, and E. Bernabeu, “Variogram-based method for contrast measurement,” Appl. Opt. 47 (22), 5027–5033 (2007).

[20] K. Tiippana, R. Nasanen, and J. Rovamo, “Contrast matching of two-dimensional compund gratings,” Vision Res. 34, 1157-1163 (1994).

[21] P. Bex and W. Makous, “Spatial frequency, phase, and the contrast of natural images”, J. Opt. Soc. Am. A. 19 (6), 1096-1106 (2002).

[22] B. Moulden, F. Kingdom, and L. F. Gatley, “The standard deviation of luminance as a metric for contrast in random-dot images”, Perception 19 (1), 79-101 (1990).

[23] P. Rodriguez-Montero, C. M. Gomez-Sarabia, and J. Ojeda-Castañeda, “Adaptive photodetector for assisted Talbot effect”, Appl. Opt. 47 (21), 3778-3783 (2008).

[24] M. Petrov, S. Stepanov, and A. Khomenko, “Photorefractive crystals in coherent optics”, Springer, Berlin, 1991.

[25] S. Stepanov, “Photo-electromotive-force in semiconductors”, in Handbook of Advanced Electronic and Photonics Materials and Devices, H. S. Nalwa, ed. Academic, 2001, Vol. 2.

[26] M. L. Arroyo-Carrasco, P. Rodriguez-Montero, and S. Stepanov, “Measurement of the coherence length of diffusely scattered laser beams with adaptive photodetectors”, Opt. Commun. 157 (1-6), 105-110 (1998).

[27] S. Stepanov, P. Rodriguez-Montero, S. Trivedi, and C. C. Wang, “Effective broadband detection of nanometer laser-induced ultrasonic surface displacements by

---

CdTe:V adaptive photoelectromotive force detector," Appl. Phys. Lett. 84 (3), 446-448 (2004).

[28] P. Rodriguez-Montero, S. Trivedi, F. Jin, C. C. Wang, S. Stepanov, G. Elliott, J. F. Meyers, J. Lee, and J. Khurgin, "Pulsed-laser vibrometer using photoelectromotive-force sensors", Appl. Phys. Lett. 83 (9), 1893-1895 (2003).

Chapter 2 Literature review

2.1. Introduction

In this chapter a review of the fundamental concepts used in this thesis is given. In the first and second sections the phenomena of interference and diffraction are briefly described. The third section is dedicated to the description of the contrast and the techniques that are used to measure it. In the last section the theoretical model and the typical features of the photo-EMF effect are reviewed.

2.2. Interference

Interference is the result of the superposition of two or more waves in the space, generating an intensity pattern that does not corresponds to the sum of the intensities of each wave [1,2].

Interference is derived from the superposition principle [1,3]. In agreement with this principle, the intensity of the electric field $\boldsymbol{E}$, produced by several different sources is equal to:

$$\boldsymbol{E} = \boldsymbol{E}_1 + \boldsymbol{E}_2 + \ldots \quad \textbf{(2. 1)}$$

In order to observe the interference pattern, the two interfering waves must meet the following conditions [1, 4]: the waves should be monochromatic, the waves ought to have the same polarization, and the phase differences between the two waves need to constant, i.e. the waves should exhibit coherence.

2.2.1 Interference of two waves

Hence, considering two plane linearly polarized waves and assuming that the waves have the same frequency [5,6], so that:

$$\boldsymbol{E}_1 = \boldsymbol{E}_{01} \exp\left[i(\boldsymbol{k}_1 \cdot \boldsymbol{r} - \omega t + \varphi_1)\right], \qquad \textbf{(2. 2)}$$

$$\boldsymbol{E}_2 = \boldsymbol{E}_{02} \exp\left[i(\boldsymbol{k}_2 \cdot \boldsymbol{r} - \omega t + \varphi_2)\right], \qquad \textbf{(2. 3)}$$

where $\boldsymbol{E}_{01}$ and $\boldsymbol{E}_{02}$ are the amplitudes of each wave, $\boldsymbol{k} = 2\pi/\lambda$ is the propagation vector or the wave's vector, $\boldsymbol{r}$ is the position vector, ω is the angular frequency, and the quantities φ_1 and φ_2 have been introduced to allow any phase difference.

The resultant wave's intensity I is proportional to the square of the amplitude of the field. So the superposition of the two monochromatic plane waves, neglecting the constants of proportionality [7,8], results in:

$$I = |\boldsymbol{E}|^2 = \boldsymbol{E} \cdot \boldsymbol{E}^* = (\boldsymbol{E}_1 + \boldsymbol{E}_2) \cdot (\boldsymbol{E}_1^* + \boldsymbol{E}_2^*), \qquad \textbf{(2. 4)}$$

$$= |\boldsymbol{E}_1|^2 + |\boldsymbol{E}_2|^2 + 2\mathrm{Re}(\boldsymbol{E}_1 \boldsymbol{E}_2^*), \qquad \textbf{(2. 5)}$$

$$= |\boldsymbol{E}_1|^2 + |\boldsymbol{E}_2|^2 + 2\boldsymbol{E}_1 \boldsymbol{E}_2 \cos[(\boldsymbol{k}_1 - \boldsymbol{k}_2) \cdot \boldsymbol{r} + (\varphi_1 - \varphi_2)], \qquad \textbf{(2. 6)}$$

$$= I_1 + I_2 + 2\sqrt{I_1 I_2} \cos \vartheta. \qquad \textbf{(2. 7)}$$

I_1 and I_2 are the intensities of each wave where $I = I_1 + I_2$ is the average intensity; and the phase difference between the two waves is defined as $\vartheta = (\boldsymbol{k}_1 \cdot \boldsymbol{r} - \boldsymbol{k}_2 \cdot \boldsymbol{r} + \varphi_1 - \varphi_2)$. In the third term of the equation, $2\sqrt{I_1 I_2} \cos \delta$, all the information about the interference is contained.

Considering two plane waves whose phase difference is constant and whose wave vectors are in the plane $x\,z$:

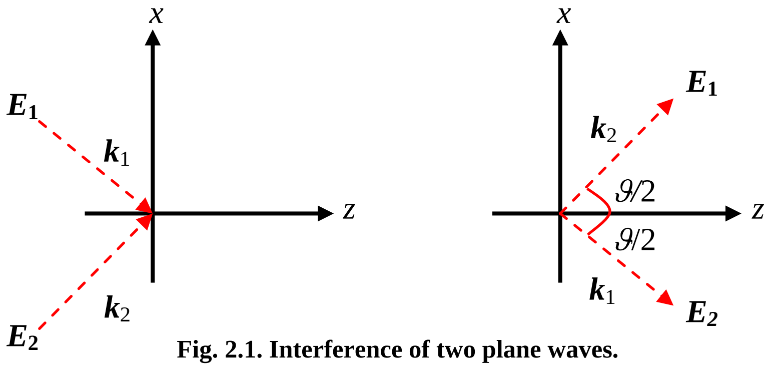

Fig. 2.1. Interference of two plane waves.

where the wave vectors ($\boldsymbol{k}_1$ and $\boldsymbol{k}_2$) and its difference are define as:

$$\boldsymbol{k}_1 = \left(-\boldsymbol{k}\sin\frac{\vartheta}{2}, 0, \boldsymbol{k}\cos\frac{\vartheta}{2}\right), \tag{2. 8}$$

$$\boldsymbol{k}_2 = \left(\boldsymbol{k}\sin\frac{\vartheta}{2}, 0, \boldsymbol{k}\cos\frac{\vartheta}{2}\right), \tag{2. 9}$$

$$\boldsymbol{k}_2 - \boldsymbol{k}_1 = \left(2\boldsymbol{k}\sin\frac{\vartheta}{2}, 0, 0\right). \tag{2. 10}$$

Evaluating the result in the plane where the interference is observed, Eq. (2.7) becomes:

$$I = I_1 + I_2 + 2\sqrt{I_1 I_2}\cos\left[2\,\boldsymbol{k}\,x\sin\left(\frac{\vartheta}{2}\right)\right], \tag{2. 11}$$

$$= I_1 + I_2 + 2\sqrt{I_1 I_2}\cos\left(\frac{2\pi x}{\Lambda}\right), \tag{2. 12}$$

where $\Lambda = \lambda/2\sin(\vartheta/2)$ is the period of the interference pattern. Eq. (2.12) can be rewritten as:

$$I = I_0\left[1 + V\cos\left(\frac{2\pi x}{\Lambda}\right)\right] = I_0 + A\cos\left(\frac{2\pi x}{\Lambda}\right), \tag{2. 13}$$

where $I_0 = I_1 + I_2$ is the average intensity, V is the interference pattern visibility. [9,10] or contrast, and A is the amplitude of the pattern. The intensity distribution generated for the interference of two waves [Eq. (2.13)] is shown in Fig. 2.2:

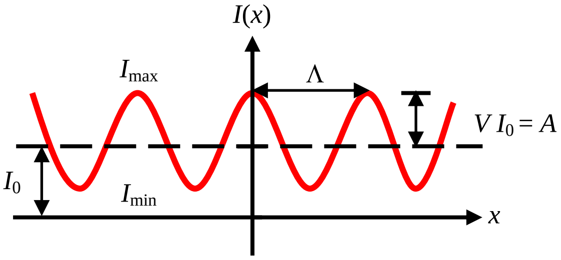

Fig. 2.2. Intensity distribution generated for interference of two waves.

The visibility V is useful for describing the quality of the interference pattern and it can be described using the Michelson definition [11]:

$$V = \frac{A}{I_0} = \frac{I_{\max} - I_{\min}}{I_{\max} + I_{\min}} = \frac{2\sqrt{I_1 I_2}}{I_1 + I_2}. \tag{2. 14}$$

In order to know the visibility V is enough with to calculate $I_{\max}$ and $I_{\min}$. Besides, one can see that V also can be expressed in terms of average intensity and amplitude.

For a simplest case of sinusoidal light distribution the possible values of the visibility or contrast are between 0 and 1 [12]. In the case of $V = 1$, the interference fringes have the maximum contrast, and when $V = 0$, the interference fringes cannot be observed.

2.3. Diffraction

The essential feature of diffraction is a deviation from rectilinear propagation arising when a wave is obstructed in some way. If the amplitude or phase of a portion of the wave is altered by transparent or opaque obstacle, the diffraction phenomena will be observed [1].

The application of the rigorous diffraction theory is very difficult and for of the most problems an approximate scalar theory is used resulting in an integral called the Huygens- Fresnel integral (see Ref. 1 and Ref. 13). Approximate analytic solutions of this integral are usually obtained using one of the two approximations: Fresnel and Fraunhofer approximations [14].

2.3.1 Huygens-Fresnel principle

The diffraction phenomena can be explained phenomenologically by Huygens' principle [15,16]. The Huygens' principle affirms that the propagation of a light wave can be predicted by assuming that every unobstructed point of the wavefront, at a given instant, can be treated as a source of spherical secondary wavelets (with the same frequency as that of the primary wave) that spreads out in all directions (see Ref. 13 and Ref. 17). Therefore, at any particular time, the new wavefront is supposed to be the envelope of all the secondary waves.

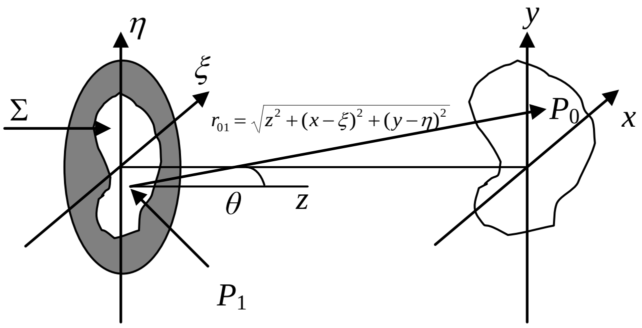

Fig. 2.3. Diagram of Huygens-Fresnel principle.

In Fig. 2.3 the diffraction aperture is assumed to lie in the (ξ,η) plane, and its illuminated in the positive direction of z. The wavefield across the (x,y) plane, which is parallel to the (ξ,η) plane, can be calculated. The Huygens-Fresnel principle [18] can be represented mathematically as:

$$U(P_0) = \frac{1}{i\lambda} \iint_{\Sigma} U(P_1) \frac{\exp(ikr_{01})}{r_{01}} \cos\theta ds, \qquad \textbf{(2. 15)}$$

where θ is the angle between the normal $\hat{n}$ and the vector r_{01} pointing from P_0 to P_1, and $\cos\theta = z/r_{01}$ (see Fig. 2.3). The Huygens-Fresnel principle can be rewritten as:

$$U(x,y) = \frac{z}{i\lambda} \iint_{\Sigma} U(\xi,\eta) \frac{\exp(ikr_{01})}{r_{01}} d\xi d\eta, \qquad \textbf{(2. 16)}$$

where $U(x,y)$ represents the field P_0 in the (x,y) plane at a distance z of the (ξ,η) plane. Eq. (2.16) shows us: that the distribution in the (ξ,η) plane is considered a set of sources, where in every point of the source emerge a spherical wave, and that in the case of the distribution in the (x,y) plane it consists in contributions of the group of irradiated fields from all the sources. Besides, the distance r_{01} is stated by:

$$r_{01} = \sqrt{z^2 + (x-\xi)^2 + (y-\eta)^2} = z\sqrt{1 + \frac{1}{2}\left(\frac{x-\xi}{z}\right)^2 + \frac{1}{2}\left(\frac{y-\eta}{z}\right)^2}. \qquad \textbf{(2. 17)}$$

To resolve Eq. (2.16) that corresponds to the Huygens-Fresnel integral is necessary to apply additional approximations: Fresnel and Fraunhofer approximations. In the next sections these are described.

2.3.2 The Fresnel approximation

Considering that the angle between $\hat{n}$ and r_{01} is small $[\leq (\pi/10)rad]$, it means that the inclination factor can be approximated to 1 $(\cos\theta \approx 1)$. This first consideration is called paraxial approximation. Therefore, the approximation $1/r_{01} \approx 1/z$ is introduced into Eq. (2.16) [19].

On the other side, considering the binomial expansion [20,21]:

$$x = (1+b)^{1/2} = 1 + \frac{1}{2}b - \frac{1}{8}b^2 + \ldots \qquad \textbf{(2. 18)}$$

and applying this expansion into Eq. (2.17), r_{01} in paraxial approximation can be represented as [22]:

$$r_{01} = z + \frac{(x-\xi)^2 + (y-\eta)^2}{2z} - \frac{[(x-\xi)^2 + (y-\eta)^2]^2}{8z^3} + \ldots \qquad \textbf{(2. 19)}$$

Thus, substituting Eq. (2.19) into Eq. (2.16) [only the first two terms] the contribution of the source point P_1 located in the (ξ,η) plane to the point P_0 can be expressed as:

$$U(x,y) = \frac{\exp(ikz)}{i\lambda z} \int\int_{-\infty}^{\infty} U(\xi,\eta) \exp\left\{ i\frac{k}{2z}[(x-\xi)^2 + (y-\eta)^2] \right\} d\xi\, d\eta, \qquad \textbf{(2. 20)}$$

this equation is known as the Fresnel diffraction integral in the paraxial approximation, and when this approximation is valid, the observer is said to be in the near field of the aperture [18]. This equation represents a superposition of spherical waves in the paraxial approximation and the amplitude for these waves is proportional to the complex amplitude of the incident field in the diffracted aperture.

2.3.3 The Fraunhofer approximation

Another form of the Eq. (2.20) is [18]:

$$U(x,y)=\frac{e^{ikz}}{i\lambda z}e^{i\frac{k}{2z}(x^2+y^2)}\int_{-\infty}^{\infty}\int_{-\infty}^{\infty}\left\{U(\xi,\eta)e^{i\frac{k}{2z}(\xi^2+\eta^2)}\right\}e^{-i\frac{k}{2z}(x\xi+y\eta)}d\xi\,d\eta, \qquad \textbf{(2. 21)}$$

in this case if the condition $z >> k(\xi^2+\eta^2)/2$ is satisfied, then the quadratic phase factor is approximately 1, and substituting $k = 2\pi/\lambda$ therefore:

$$U(x,y)=\frac{e^{ikz}}{i\lambda z}e^{i\frac{k}{2z}(x^2+y^2)}\int_{-\infty}^{\infty}\int_{-\infty}^{\infty}U(\xi,\eta)\,e^{-i\frac{2\pi}{\lambda z}(x\xi+y\eta)}d\xi\,d\eta, \qquad \textbf{(2. 22)}$$

this result is known as the Fraunhofer diffraction, and when this approximation is valid, the observer is said to be in the far field of the aperture. In this case, the observation plane is far compared with the size of the diffracting aperture.

Comparing Eq. (2.22) with the definition of Fourier transform the diffracted field can be expressed as:

$$U(x,y)=\frac{e^{ikz}}{i\lambda z}e^{i\frac{k}{2z}(x^2+y^2)}F[U(\xi,\eta)]. \qquad \textbf{(2. 23)}$$

In conclusion, the complex amplitude of the Fraunhofer diffraction is proportional to the Fourier transform of the aperture distribution in the (ξ,η) plane.

2.3.4 Talbot effect

The Talbot effect [23], also referred as a self-imaging phenomenon of periodic objects, states that any distribution, which is a periodic function of x and y, will be also periodic in the direction of propagation z. H. F. Talbot [23] described such effect in 1836, whereas Lord Rayleigh [24] rediscovered the effect, provided a theoretical explanation, and showed that the Talbot effect is a natural consequence of Fresnel diffraction.

Considering a grating (one-dimensional) with amplitude transmittance $t(x)$ of a period Λ, illuminated by an on-axis plane wave of wavelength λ, the diffracted intensity will reproduce an exact image of the grating in a series of equally spaced planes [25]. These planes, usually called Talbot planes, are located at distances from the grating that are integer multiples of the Talbot distance (see Fig. 2.4):

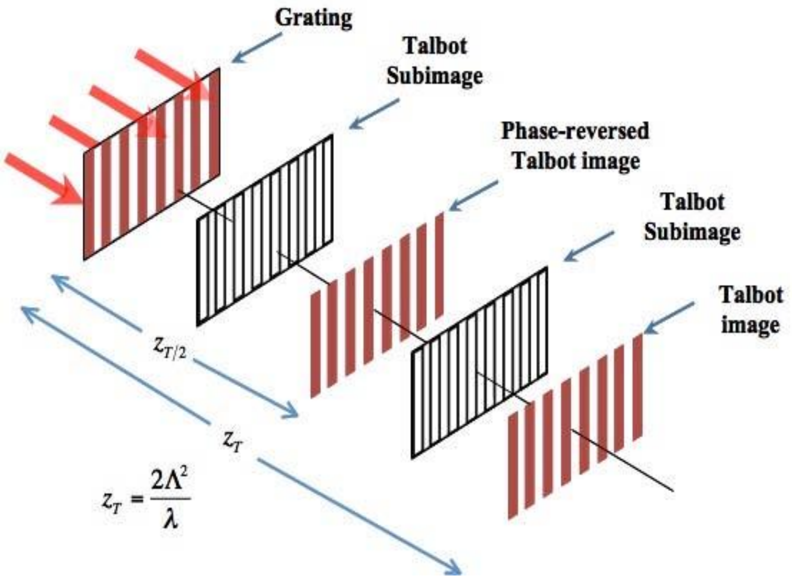

Fig. 2.4. Localization of Talbot image planes behind the grating.

First, the effect for a simplest case of sinusoidal grating is analyzed. Assuming that a uniform wave plane illuminates a sinusoidal amplitude grating, the field immediately behind the grating is equal to its amplitude transmittance. Then, the standard notation for the complex amplitude transmittance $t(\xi)$ of the grating can be expressed as [18]:

$$t(\xi,\eta) = \frac{1}{2}\left[1 + m\cos\left(\frac{2\pi\xi}{\Lambda}\right)\right], \tag{2. 24}$$

where Λ is the period of the grating, and m represents the peak to peak change of amplitude transmittance.

Employing the Fresnel formulation [Eq. (2.20)], the next expression is obtained:

$$U(x,y) = \frac{\exp(ikz)}{i\lambda z}\int_{-\infty}^{\infty}\int U(\xi)\exp\left\{i\frac{k}{2z}[(x-\xi)^2]\right\}d\xi, \tag{2. 25}$$

substituting the complex amplitude transmittance of the grating:

$$U(x,z) = \frac{1}{2}\frac{\exp(ikz)}{i\lambda z}\int_{-\infty}^{\infty}\left[1 + m\cos\left(\frac{2\pi\xi}{\Lambda}\right)\right]\exp\left\{i\frac{\pi}{\lambda z}[(x-\xi)^2]\right\}d\xi, \tag{2. 26}$$

therefore if $\cos(z) = [\exp(iz) + \exp(-iz)]/2/2$ [26], Eq. (2.26) can be represented by:

$$U(x,z)=\frac{1}{2}\frac{\exp(ikz)}{i\lambda z}\int_{-\infty}^{\infty}\left\{1+\frac{m}{2}\exp\left(\frac{i2\pi\xi}{\Lambda}\right)+\frac{m}{2}\exp\left(-\frac{i2\pi\xi}{\Lambda}\right)\right\}$$
$$\cdot\exp\left(\frac{i\pi x^2}{\lambda z}-\frac{i2\pi x\xi}{\lambda z}+\frac{i\pi\xi^2}{\lambda z}\right)d\xi. \tag{2. 27}$$

To calculate the Fresnel diffraction integral, each term is evaluated:

$$\int_{-\infty}^{\infty}\exp\left(\frac{i\pi x^2}{\lambda z}-\frac{i2\pi x\xi}{\lambda z}+\frac{i\pi\xi^2}{\lambda z}\right)d\xi=\sqrt{i\lambda z}. \tag{2. 28}$$

$$\int_{-\infty}^{\infty}\left[\frac{m}{2}\exp\left(\frac{i2\pi\xi}{\Lambda}\right)\right]\exp\left(\frac{i\pi x^2}{\Lambda z}-\frac{i2\pi x\xi}{\lambda z}+\frac{i\pi\xi^2}{\lambda z}\right)d\xi=$$
$$=\frac{m}{2}\sqrt{i\lambda z}\exp\left(\frac{i2\pi x}{\Lambda}\right)\exp\left(-\frac{i\pi\lambda z}{\Lambda^2}\right). \tag{2. 29}$$

$$\int_{-\infty}^{\infty}\left[\frac{m}{2}\exp\left(-\frac{i2\pi\xi}{\Lambda}\right)\right]\exp\left(\frac{i\pi x^2}{\Lambda z}-\frac{i2\pi x\xi}{\lambda z}+\frac{i\pi\xi^2}{\lambda z}\right)d\xi=$$
$$=\frac{m}{2}\sqrt{i\lambda z}\exp\left(-\frac{i2\pi x}{\Lambda}\right)\exp\left(-\frac{i\pi\lambda z}{\Lambda^2}\right). \tag{2. 30}$$

Eq. (2.27) can be rewritten as:

$$U(x,z)=\frac{1}{2}\frac{\exp(ikz)}{i\lambda z}\left[\sqrt{i\lambda z}+\frac{m}{2}\sqrt{i\lambda z}\exp\left(\frac{i2\pi x}{\Lambda}\right)\exp\left(-\frac{i\pi\lambda z}{\Lambda^2}\right)\right.$$
$$\left.+\frac{m}{2}\sqrt{i\lambda z}\exp\left(-\frac{i2\pi x}{\Lambda}\right)\exp\left(-\frac{i\pi\lambda z}{\Lambda^2}\right)\right]=$$
$$=\frac{\exp(ikz)}{\sqrt{i\lambda z}}\left[\frac{1}{2}+\frac{m}{4}\exp\left(\frac{i2\pi x}{\Lambda}\right)\exp\left(-\frac{i\pi\lambda z}{\Lambda^2}\right)\right.$$
$$\left.+\frac{m}{4}\exp\left(-\frac{i2\pi x}{\Lambda}\right)\exp\left(-\frac{i\pi\lambda z}{\Lambda^2}\right)\right]. \tag{2. 31}$$

Thus, the Fourier transform of Eq. (2.24), at distance z from the grating is [18]:

$$U(x,z)=\frac{1}{2}\left[1+m\exp\left(-\frac{i\pi\lambda z}{\Lambda^2}\right)\cos\left(\frac{2\pi x}{\Lambda}\right)\right], \tag{2. 32}$$

where the term $\exp(ikz)/\sqrt{i\lambda z}$ was omitted.

Finally, the intensity distribution of Fresnel diffraction pattern can be evaluated as [18]:

$$I(x,z)=\frac{1}{4}\left[1+2m\cos\left(\frac{\pi\lambda z}{\Lambda^2}\right)\cos\left(\frac{2\pi x}{\Lambda}\right)+m^2\cos^2\left(\frac{2\pi x}{\Lambda}\right)\right]. \tag{2. 33}$$

Considering three special cases of this result, some expressions of intensity distribution of Fresnel diffraction patterns (Talbot images) that are formed behind of the grating are obtained:

(a) Propagation to $z = \dfrac{2n\Lambda^2}{\lambda}$

Substituting z into Eq. (2.33) the intensity distribution can be rewritten as [18]:

$$I(x,z) = \frac{1}{4}\left[1 + m\cos\left(\frac{2\pi x}{\Lambda}\right)\right]^2. \qquad \textbf{(2. 34)}$$

Eq. (2.34) can be interpreted as an exact image (Talbot image) of the intensity that would be observed behind the grating (see Fig. 2.4).

(b) Propagation to $z = \dfrac{(2n+1)\Lambda^2}{\lambda}$

If the distance satisfies $z = \dfrac{(2n+1)\Lambda^2}{\lambda}$ the intensity distribution is given by [18]:

$$I(x,z) = \frac{1}{4}\left[1 - m\cos\left(\frac{2\pi x}{\Lambda}\right)\right]^2. \qquad \textbf{(2. 35)}$$

At this length, one can observe that the image of the grating has reversed visibility or that the intensity distribution has a 180° spatial phase shift (see Fig. 2.4). This image is called Talbot negative self-image [27].

(c) Propagation to $z = \dfrac{(2n-1)\Lambda^2}{2\lambda}$

If the observation distance now satisfies $z = \dfrac{(2n-1)\Lambda^2}{2\lambda}$ the intensity distribution is [18]:

$$I(x,z) = \frac{1}{4}\left[1 + m^2\cos^2\left(\frac{2\pi x}{\Lambda}\right)\right] = \frac{1}{4}\left[\left(1 + \frac{m^2}{2}\right) + \frac{m^2}{2}\cos\left(\frac{4\pi x}{\Lambda}\right)\right]. \qquad \textbf{(2. 36)}$$

At this length, i.e. at smaller regular fractions of the Talbot length, the intensity distribution is almost uniform and subimages can also be observed. Here, the visibility is minimal and the subimages have reduced contrast.

Next, the effect for a binary grating is analyzed. In principle, assuming that a uniform wave plane illuminates the binary grating, the field immediately behind the grating is equal to its amplitude transmittance. Then, the complex amplitude transmittance $t(\xi)$ of the grating can be expressed by Fourier series as [28,29]:

$$t(\xi) = \sum_{n=-\infty}^{\infty} a_n \exp\left(\frac{i2\pi\xi\, n}{\Lambda}\right), \tag{2. 37}$$

where $n = 2m-1$, $m = 0,1,2,3\ldots$, is the period of the grating, and a_n are Fourier coefficients.

Employing the Fresnel formulation [Eq. (2.20)], the next expression is obtained:

$$U(x,z) = \int_{-\infty}^{\infty} U(\xi) \exp\left[\frac{i\pi(x-\xi)^2}{\lambda z}\right] d\xi. \tag{2. 38}$$

Eq. (2.38) can be rewritten as [30]:

$$U(x,z) = \int_{-\infty}^{\infty} U(v) \exp[-i\pi\lambda z v^2]\, \exp[i2\pi x v]\, dv, \tag{2. 39}$$

where $U(v)$ is the Fourier transform of $U(\xi)$. Here:

$$\begin{aligned} U(v) &= \int_{-\infty}^{\infty} t(\xi)\, \exp[-i2\pi v\xi]\, d\xi, \\ &= \int_{-\infty}^{\infty} \sum_{n=-\infty}^{\infty} a_n \exp\left[\frac{i2\pi\xi\, n}{\Lambda}\right] \exp[-i2\pi v\xi]\, d\xi, \\ &= \sum_{n=-\infty}^{\infty} a_n\, \delta\left[v - \frac{1}{\Lambda}\right]. \end{aligned} \tag{2. 40}$$

Substituting the value of $U(v)$ into Eq. (2.39):

$$U(x,z) = \int_{-\infty}^{\infty} \sum_{n=-\infty}^{\infty} a_n\, \delta\left[v - \frac{1}{\Lambda}\right] \exp[-i\pi\lambda z v^2] \exp[i2\pi x v]\, dv, \tag{2. 41}$$

applying a property of the delta function [31], the complex amplitude of the Fresnel diffraction pattern of a binary grating can be rewritten as:

$$U(x,z) = \sum_{n=-\infty}^{\infty} a_n \exp\left[-i\pi\lambda z\left(\frac{n^2}{\Lambda^2}\right)\right] \exp\left(\frac{i2\pi x\, n}{\Lambda}\right). \tag{2. 42}$$

Thus, the intensity distribution of the Fresnel diffraction pattern is given by [28]:

$$\begin{aligned} I(x,z) &= \left|U(x,z)\right|^2 = U(x,z)\cdot U^*(x,z) = \\ &= \sum_{n=-\infty}^{\infty} a_n \exp\left[-i\pi\lambda z\left(\frac{n^2}{\Lambda^2}\right)\right]\exp\left(\frac{i2\pi\, x n}{\Lambda}\right)\cdot \sum_{n=-\infty}^{\infty} a_n^* \exp\left[i\pi\lambda z\left(\frac{n^2}{\Lambda^2}\right)\right]\exp\left(-\frac{i2\pi\, x n}{\Lambda}\right), \\ &= \sum_{r=-\infty}^{\infty} a_r \exp\left[-i\pi\lambda z\left(\frac{r^2}{\Lambda^2}\right)\right]\exp\left(\frac{i2\pi\, x r}{\Lambda}\right)\cdot \sum_{n=-\infty}^{\infty} a_n^* \exp\left[i\pi\lambda z\left(\frac{n^2}{\Lambda^2}\right)\right]\exp\left(-\frac{i2\pi\, x n}{\Lambda}\right), \\ &= \sum_{r=-\infty}^{\infty}\sum_{n=-\infty}^{\infty} a_r a_n^* \exp\left[-i\pi\lambda z\left(\frac{r^2-n^2}{\Lambda^2}\right)\right]\exp\left[i2\pi x\left(\frac{r-n}{\Lambda}\right)\right]. \end{aligned} \tag{2. 43}$$

With the following change of variable $l = r - n$, Eq. (2.43) can be rewritten as [28]:

$$\begin{aligned} I(x,z) &= \sum_{l=-\infty}^{\infty}\sum_{n=-\infty}^{\infty} a_{l+n} a_n^* \exp\left[-i\pi\lambda z\left(\frac{l^2+2l\,n}{\Lambda^2}\right)\right]\exp\left[i2\pi x\left(\frac{l}{\Lambda}\right)\right], \\ &= \sum_{l=-\infty}^{\infty}\left[\exp\left(-\frac{i\pi\lambda\, z\, l^2}{\Lambda^2}\right)\sum_{n=-\infty}^{\infty} a_{l+n} a_n^* \exp\left(-\frac{i2\pi\lambda\, z\, l\, n}{\Lambda^2}\right)\right]\exp\left(\frac{i2\pi\, x l}{\Lambda}\right), \\ &= \sum_{l=-\infty}^{\infty} a_l(z) \exp\left(\frac{i2\pi\, x l}{\Lambda}\right), \end{aligned} \tag{2. 44}$$

where $A_l(z)$ is the complex amplitude of the $l\,th$ harmonic, and can be represented as [28]:

$$A_l(z) = \exp\left(-\frac{i2\pi\, l^2 z}{z_T}\right)\sum_{n=-\infty}^{\infty} a_{l+n} a_n^* \exp\left(-\frac{i2\pi\, l\, n\, 2z}{z_T}\right), \tag{2. 45}$$

where $z_T = 2\Lambda^2/\lambda$ is the Talbot distance.

Finally, for a binary grating, if the observation distance satisfies $z = z_T/4$, i.e. at one quarter of the Talbot distance, the intensity distribution of the Fresnel diffraction pattern is uniform. Thus, if the observation distance now satisfies $z = z_T/2$, the intensity distribution of the grating has reversed visibility [28].

2.4 CCD-based techniques for analysis of contrast

2.4.1 Contrast

Contrast is an essential perceptual attribute of an image or an object, i.e. is the variation in visual properties that makes an image or an object noticeable from other images or objects and their surroundings [32].

In recent years the contrast measurement have received much attention and numerous techniques have been developed to determine it because is a useful tool in several optics applications, such as metrology [33,34], interferometry [35,36], and biomedical optics [37,38].

In case when the intensity distribution presents only one spatial harmonics e.g. in case of interference of two waves, it is enough to know the maximum and the minimum intensity ($I_{\max}$ and $I_{\min}$) of the pattern in order to determine its contrast or visibility V using the Michelson definition [Eq. (2.14)] [11].

However, evaluation of contrast using Michelson definition presents a disadvantage: the contrast is evaluated only by the maximum and the minimum intensity of the signal, which can be ambiguous for complex intensity distribution, e.g. when more than one spatial harmonic is present, when the interference fringes are distorted, or in the presence of noise, etc. In this case, statistical techniques or more complex algorithms of image processing should be applied in order to evaluate the contrast.

To date there are several conventional techniques that determine the contrast of an intensity distribution, being the root mean square (RMS) method [32], histogram-based method [39,40] and semivariogram-based method [41] most representative of them. All this techniques share the common feature: a CCD camera is used as an input sensor, the image of the intensity patterns is recorded, and then processed and analyzed, in order to find the contrast value. Next, the most characteristic features of these techniques will be described.

2.4.2 CCD–based techniques

2.4.2.1 Root Mean Square (RMS)

The root mean square (RMS), also known as the quadratic mean, is the square root of the mean of the squares of the sample values and it is a useful tool in many fields, including physics and electric engineering [42].

In RMS method all the signal data are considered and analyzed statistically, and the ratio of standard deviation and average signal is found, and it is a common way to evaluate the contrast in the case of a periodical pattern [43] or compound images [44].

Therefore, the RMS contrast C_{RMS} calculation is the standard deviation [45,46] of the n pixels intensities from the average level $\bar{I}$ (see Ref. 32 and 43) and results in:

$$C_{RMS} = \frac{\left[\frac{1}{n-1}\sum_{i=1}^{n}(I_i - \bar{I})^2\right]^{1/2}}{\bar{I}} = \frac{I_{RMS}}{\bar{I}}, \tag{2. 46}$$

where n is the total number of pixels in the input image. Intensities I_i are normalized to a maximum value of 1, and $\bar{I}$ is the average intensity across the image [47]. This quantity is relative easy to calculate for a simple (one-dimensional) periodical pattern.

The RMS method was employed in Ref. 47 to obtain the contrast of images, and their results support that the RMS contrast is a good indicator of the visibility of images, which is in line with previous studies [44,48].

However, the disadvantage of this technique is that the amplitude of the signal can be affected in presence of noise [43]. In order to avoid this problem other techniques more robust to evaluate the contrast have been developed.

2.4.2.2 Semivariogram method

The semivariogram [49,50] describes the magnitude, spatial scale, and general form of the variation in a given set of data [51], and has been used widely to quantify and to characterize the spatial variability the phenomenon under study [52]. The semivariogram is used in geostatistics [53,54] in applications as mining [55], geology [56,57], ecology [58], texture classification of satellite images [59,60], etc.

Semivariogram [61,62] is a graphical representation of a spatial variability and provide a means of measuring the spatial dependency of continuously varying phenomenon [63] by a function that relates semivariance with distance or spatial separation [64,65].

Spatial dependence describes the phenomenon that attributes at locations close to each other are probable to have similar values while those that are far apart are probable to have different values [66,67], and semivariance is frequently applied to image processing [68] because expresses the degree of relationship between pixels in an image [63]. Therefore, if there is a strong spatial dependence, pixels that are closer together will have a smaller semivariance.

In the case of images obtained by CCD camera, the semivariogram function $\gamma(h)$ measures the spatial correlation of the image and has been employed to estimate the standard deviation of nonuniform images [41].

The semivariogram function [69] of a given one-dimensional periodical intensity distribution $I(x)$ can be defined as [43]:

$$\gamma(h) = \frac{1}{2}\left\langle [I(x+h) - I(x)]^2 \right\rangle, \qquad \textbf{(2. 47)}$$

where $\langle * \rangle$ means averaging with respect to x and h means a displacement along x axis. The semivariogram captures the variations of spatial dependence of signals $I(x+h)$ and $I(x)$. Clearly, the value of γ is maximum when h is equal to a half of the period $p/2$ of a signal $I(x)$.

To determine the semivariogram of a sampled signal, it is necessary that the periodical pattern in the image should be aligning with the y axis for averaging the values of the intensities in each column, and therefore a one-dimensional signal $I(x)$ is obtained.

The semivariogram function [Eq. (2.47)] was used in Ref. 43 for measuring the contrast of sinusoidal intensity distribution in presence of noise, and it was demonstrated that this technique is quite robust since the semivariogram is obtained as an average process (as RMS method) and noise affects hardly any to the contrast estimation. Besides, experimentally was showed the advantage of using it for the Talbot effect because the results obtained are better compared with other techniques [43].

It was demonstrated [43] that the difference between the maximum and minimum values of the semivariogram is equal to the square of the amplitude of the signal A:

$$A^2 = [\gamma(p/2 - \hat{\gamma}(0))]. \tag{2. 48}$$

Therefore the contrast or visibility can be represented by [43]:

$$V_\gamma = \frac{[\gamma(p/2 - \hat{\gamma}(0))]^{1/2}}{\bar{I}} = \frac{A}{\bar{I}}. \tag{2. 49}$$

where $\hat{\gamma}$ means that the value has been obtained by an extrapolation. The semivariogram is a measure of contrast as a function of distance and, this quantity coincides with Michelson’s equation for sinusoidal patterns [see Eq. (2.14)].

However, the contrast estimation using semivariogram function for more complicated light intensity distribution, which includes higher spatial harmonics, has not been done yet.

Despite of their simplicity, all CCD–based methods share common weaknesses, namely, the necessity for image processing, necessity of a filter for avoid the saturation of the camera, and sensitivity to the environmental vibrations.

2.5 Basic principles of non-steady-state photo-electromotive force (photo-EMF) effect

Non-steady-state photo-electromotive force (photo-EMF) effect was described by Petrov *et al*. [70] in 1990's.

The photo-EMF effect manifests itself as an alternating current (ac) through a short-circuited photoconductive sample illuminated by an oscillating non-uniform light distribution $I(x,t)$.

The adaptive photodetectors [71] based on the photo-EMF effect [72] have already been proposed for a number of practical applications. In particular are used for detecting vibrations of diffusely scattering objects [73], measuring the coherent length of several light sources [74], for sensing laser-generated ultrasonic displacements [75,76], for laser vibrometry [77], for characterizing femtosecond pulses [78], for determining photoelectric parameters of organic photoconductors [79], etc.

A detailed analysis of photo-EMF effect for sinusoidal light distribution can be found in Ref. 80, and here it is only briefly discussed.

2.5.1 General description

The standard configuration for observing the photo-EMF effect is shown in Fig. 2.5. Under illumination by two coherent plane waves one of which is periodically modulated in phase with the frequency $\Omega = 2\pi f$ and amplitude Δ an oscillating sinusoidal light distribution is created inside photoconductive material [81]:

$$I(x,t) = I_0 + I_0 V \cos[Kx - \Delta \sin(\Omega t)], \qquad \textbf{(2. 50)}$$

generating spatially non-uniform distribution of the mobile carriers $n(x,t)$. Here I_0 is the average light intensity, V is the visibility or contrast, $K = 2\pi/\Lambda$ is the spatial frequency of the interference pattern, and Λ is the fringe spacing.

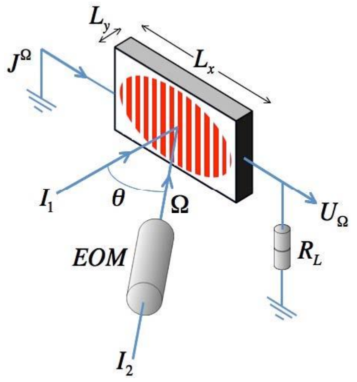

Fig. 2.5. Standard configuration for photo-EMF effect. Here I_1 and I_2 are the intensities of each wave, EOM is the electro-optical modulator, J^Ω is the photo-EMF current, U_Ω is the photo-EMF voltage, and R_L is the load resistor.

Mobile charge redistribution due to the diffusion/drift and its subsequent trapping gives rise to a relatively stable space charged electric field $E_{sc}(x,t)$.

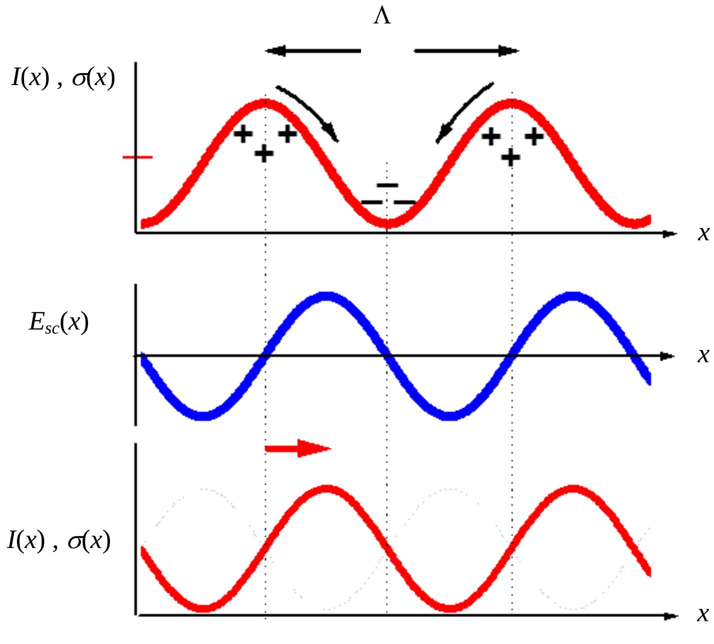

Fig. 2.6. Diagram of space-charge electric field generation in non-steady-state photo-EMF effect.

The expression for the total current density flowing through the sample is:

$$J_\Sigma(x,t) = e\mu n(x,t) E_{sc}(x,t) + eD\frac{\partial n(x,t)}{\partial x} + \varepsilon\varepsilon_0 \frac{\partial E_{sc}(x,t)}{\partial x}, \qquad \textbf{(2. 51)}$$

where e is the electronic charge, μ the mobility, $n(x,t)$ is the density of the mobile photoelectrons in the conduction band, D is the diffusion coefficient, ε is the permittivity, and ε_0 is the vacuum permittivity.

If the Eq. (2.51) is integrated in the interval of 0 to L and due to the boundary conditions $n(0,t) = n(L,t)$ the averaged diffusion current [the second term of the Eq. (2.51)] caused by the nonuniform photocarriers density, has to be equal to zero [82]:

$$\int_0^L \frac{\partial n(x,t)}{\partial x} dx = n(L,t) - n(0,t) \equiv 0. \qquad \textbf{(2. 52)}$$

Because of the potential nature of the electric field, the averaged displacement current through the sample represented by the third term of the Eq. (2.51) is equal to zero. Therefore, the density of the total current thought the sample is equal to drift current:

$$J_\Sigma(x,t) = \frac{e\mu}{\Lambda} \int_0^\Lambda E(x,t)\, n(x,t) dx. \qquad \textbf{(2. 53)}$$

Under the steady state conditions, the diffusion-driven sinusoidal distribution of E_{sc} is shifted by $\Lambda/4$ with respect to $\sigma(x)$, (see Fig. 2.6), therefore the photo-EMF current is zero.

However, if the intensity distribution moves, the situation is different. It is assumed that the photoconductivity $\sigma(x,t)$ follows the vibrations of the illuminating intensity distribution $I(x,t)$ almost instantaneously, while the distribution $E_{sc}(x,t)$ possesses certain inertia with response time τ_{sc}. As a result of the phase shift between $\sigma(x,t)$, concentration distributions $n(x,t)$, and space charge field $E_{sc}(x,t)$ is different from $\Lambda/4$, the non-steady-state photo-electromotive force (photo-EMF) is created giving rise to alternating current through the short-circuited semiconductor [81, 83].

In order to calculate the photo-EMF current amplitude, first the complex amplitudes of space charge field distribution, as well as the carriers concentration should be found, solving the standard set of equations, described e.g. in [80].

2.5.2 Main equations of the theoretical description of the photo-EMF effect in monopolar photoconductor

Next, let us consider the main equations, which describe the process of photo-EMF current formation. For the simplicity the widely assumed model of a monopolar (*n*-type) photoconductor with a single deep impurity level is used. The recombination that occurs through the same deep trap level is used. Dark conductivity (due to the thermal excitation) and saturation of the impurity centers are neglected. Besides, no external bias is applied to the sample $(E_0 = 0)$.

In this model, absorption of light photon leads to the excitation of the mobile electron from the impurity center with the generation rate g. The mobile carriers are driven by drift and/or diffusion and they are redistributed on the conduction band. After some time, defined as a recombination time τ, their recombine on available acceptor level.

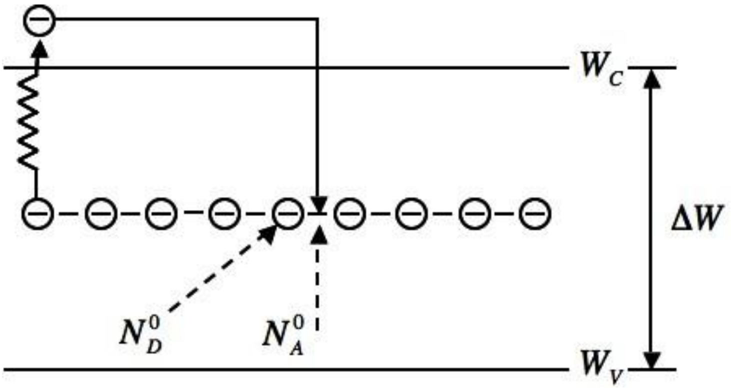

Fig. 2.7. Energy levels structure used for model of a monopolar photoconductor. The conduction band and the valence band are W_C and W_V respectively. Initial concentrations of donor and acceptor centers (for electrons) are N_D^0 and N_A^0 respectively.

The balance equation for mobile carriers (with concentration $n(x,t)$) in the conduction band and for ionized deep impurities (with concentration $N^+(x,t)$) can be written as follows:

$$\frac{\partial n(x,t)}{\partial t} = g(x,t) - \frac{n(x,t)}{\tau} + \frac{1}{e}\frac{\partial j_\Sigma(x,t)}{\partial x}, \qquad \textbf{(2. 54)}$$

hence

$$\frac{\partial N^{+}(x,t)}{\partial t}=g(x,t)-\frac{n(x,t)}{\tau}, \tag{2. 55}$$

where e is the electronic charge. The expression for current density $J_{\Sigma}(x,t)$ [80]:

$$J_{\Sigma}(x,t)=e\mu n(x,t)E_{sc}(x,t)+eD\frac{\partial n(x,t)}{\partial x}, \tag{2. 56}$$

includes two main contributions: drift (with the mobility μ) driven by a space-charge field E_{sc} and diffusion (with the diffusion coefficient D) driven by carriers' concentration gradient.

The space-charge field E_{sc} is created by a nonuniform distribution of charges with the density $\rho=e\left(N^{+}-n\right)$ and both are related through the Poisson's equation:

$$\frac{\partial E(x,t)}{\partial x}=\frac{1}{\varepsilon\varepsilon_0}\rho(x,t). \tag{2. 57}$$

Finally, the continuity equation which relates the current density $J_{\Sigma}(x,t)$ and the space-charge density $\rho(x,t)$, can be written as [80]:

$$\frac{\partial\rho(x,t)}{\partial t}=-\frac{\partial J_{\Sigma}(x,t)}{\partial x}. \tag{2. 58}$$

2.5.3 Photo-EMF current amplitude

The solution of Eq. (2.53) can be obtained in the approximation of low amplitude of oscillations $(\Delta<<1)$ and low contrast $(V<<1)$ of the illuminating interference pattern.

As a result of this solution the amplitude of the first harmonic of photo-EMF current can be expressed as [80]:

$$\begin{aligned}J_{\Sigma}^{\Omega}&=J_0(\Delta)\,J_1(\Delta)\frac{V^2}{4}\sigma_0\\&\cdot\left[\frac{2iE_0-\Omega\tau_{di}(iE_D+E_0)}{1+i\Omega\tau_{di}(1+K^2L_D^2+iKL_0)}+\frac{-2iE_0-\Omega\tau_{di}(iE_D-E_0)}{1+i\Omega\tau_{di}(1+K^2L_D^2-iKL_0)}\right],\end{aligned} \tag{2. 59}$$

where σ_0 is the average photoconductivity, E_0 is the external electric field applied to the sample, $\tau_{di} = \varepsilon\varepsilon_0 / \sigma_0$ is the dielectric relaxation time due to the average photoconductivity, $E_D = KD/\mu$ is the diffusion electric field, $L_D = \sqrt{D\tau}$ is the diffusion length, and $L_0 = \mu\tau E_0$ is the drift length of the charge carriers.

For the simplest case of zero external electric field $(E_0, L_0 = 0)$, the amplitude of the first harmonic of the photo-EMF current can be expressed as [80,84]:

$$J_\Sigma^\Omega = \frac{\Delta V^2}{4} \frac{\sigma_0}{1+K^2L_D^2} E_D \frac{-i\Omega/\Omega_0}{1+i\Omega/\Omega_0}, \qquad \textbf{(2. 60)}$$

where the characteristic cutoff frequency Ω can be defined as:

$$\Omega_0 = \tau_{sc}^{-1} = [\tau_{di}(1+K^2L_D^2)]^{-1}, \qquad \textbf{(2. 61)}$$

here τ_{sc} is equal to the recording/erasure time of the electric field grating [85].

There are some dependencies of the effect that are important to mention. First, the frequency transfer function of J_Σ^Ω is similar to the transfer function of RC circuit [86], i.e. at low frequencies $\Omega << \Omega_0$ the signal grows up to the cutoff frequency Ω_0, and then has a constant level at frequencies $\Omega_0 << \Omega$ (see Fig. 2.8).

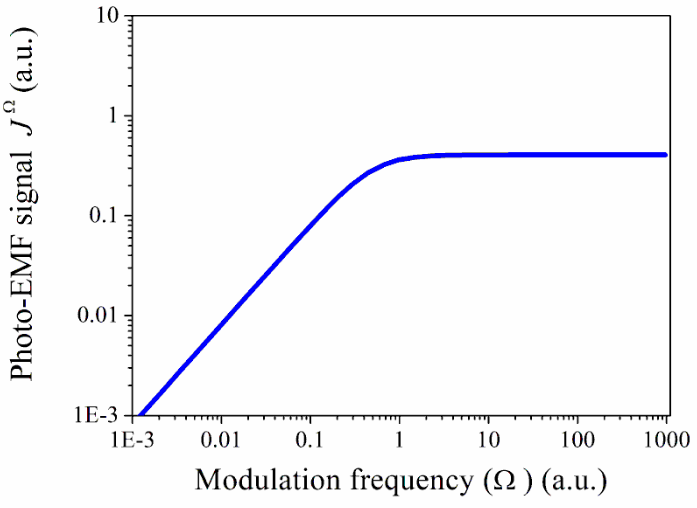

Fig. 2.8. Dependence of the photo-EMF signal versus the modulation frequency Ω.

This kind of transfer function of J_{Σ}^{Ω} is responsible for the inherent adaptive properties of the photo-EMF effect for detection of phase-modulated signals. In other words, by the nature of the photo-EMF effect the photodetector has the ability to compensate slow environmental phase drifts [81], i.e. possess additional robustness to the environmental vibrations.

In addition the effect possess spatial adaptability to the wavefront irregularities in the interfering beams, since the space charge field and concentration distribution are the exact replica of the intensity distributions, i.e. the detection can be performed in presence of speckle or aberrations.

For these outstanding properties photo-EMF based detector has already been proposed for a number of practical applications such as it was mentioned before.

Another is the dependence of the photo-EMF signal in function of the spatial frequency K of the interference pattern, and it is shown in Fig. 2.9.

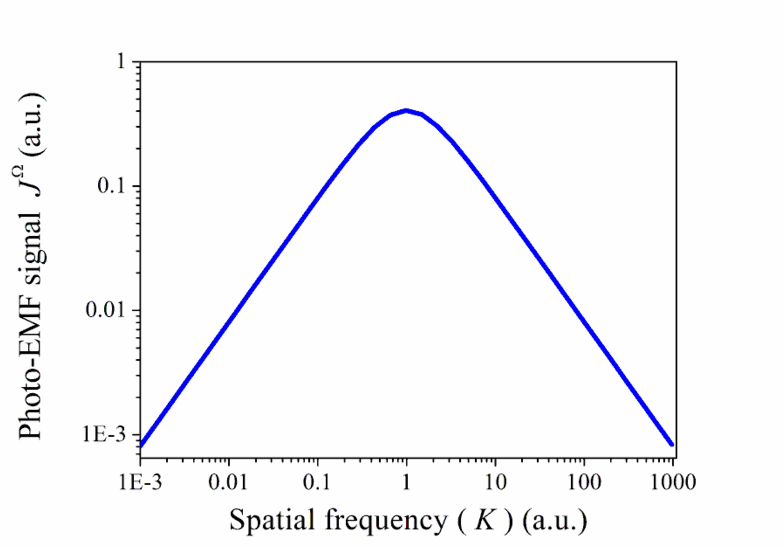

Fig. 2.9. Dependence of the photo-EMF signal versus the spatial frequency K .

One can see that the signal grows linearly with the increasing spatial frequency, reach some maximum and then decays. The linear growth is determined by the increasing with spatial frequency diffusion field $E_D = KD/\mu$, while the decay is produced by the reduced effective contrast when the transport length of the carriers are greater than the spatial period of the interference pattern. The maximum of this dependence corresponds to a spatial frequency equal to the inverse carriers' diffusion length:

$$K_{opt} = L_D^{-1}. \tag{2. 62}$$

This spatial frequency is considered to be an optimum one when using the photo-EMF effect for the detection purposes since the maximal value of the signal-to-noise ratio is observed.

The theoretical dependence of the photo-EMF signal amplitude J_Σ^Ω [Eq. (2.60)] as a function of modulation amplitude Δ is shown in Fig. 2.10. One can see that for arbitrary modulation amplitudes the photo-EMF signal is proportional to the product of two Bessel functions [87]:

$$J(\Delta) \propto J_0(\Delta) J_1(\Delta), \tag{2. 63}$$

where $J_0(\Delta)$ and $J_1(\Delta)$ are the zero-order and the first-order Bessel functions respectively. At small vibration amplitude $(\Delta << 1)$ the photo-EMF signal grows linearly with the amplitude of the phase modulation $J_\Sigma^\Omega \propto \Delta$. This property of photo-EMF effect allows its use as an adaptive detector of the vibrations amplitudes in laser vibrometry, and ultrasound detection.

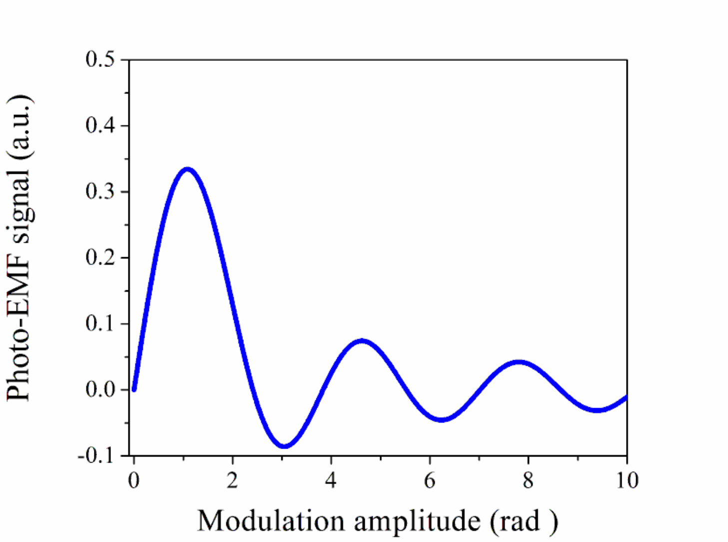

Fig. 2.10. Dependence of the photo-EMF signal versus the modulation amplitude K at frequency $\Omega_0 << \Omega$.

Finally, Eq. (2.60) shows that the output current amplitude is proportional to the square of the light pattern visibility or contrast $J_{\Sigma}^{\Omega} \propto V^{2}$, which makes the photo-EMF effect suitable for the direct measurements of the changes on the light pattern visibility.

Because of this property, the photodetector based on photo-EMF effect was used in Ref. 88 for analyzing the Talbot effect, since an electrical current that is proportional to the square of the visibility of the Fresnel diffraction patterns can be produced directly. It was demonstrated that photo-EMF effect can be used for Talbot self-images localization in real time, with high spatial resolution, and without any signal processing.

However, the direct application of the photo-EMF effect for the general problem of measurement of contrast distribution and related Talbot self-images localization requires solving several problems.

First of all, most of the practical applications of Talbot effect use the diffraction on a binary grating, which means that more than one spatial harmonic is involved in intensity distribution on photo-EMF detector. However, the widely used theoretical model of photo-EMF effect available up to now is based on the assumption that the intensity distribution is a sinusoidal one.

The details of photo-EMF current formation in the presence of additional spatial harmonics are not clear. It is necessary to verify also how the dynamics of space charge grating formation is affected in such a case. And, the most important, the global question of “what is the visibility which is measured in such condition” should be answered.

In addition, the comparative analysis of the photo-EMF effect with the already existent techniques which are currently used for a measurement of contrast is still absent.

Therefore, the main objective of this thesis is the theoretical and experimental investigation of the non-steady-state photo-EMF effect induced by light distributions that contains spatial harmonics i.e. periodical one-dimensional (1-D) light patterns, and its applications to Talbot interferometry.

2.6 References

---

[1] E. Hetch, *Óptica*, Addison Wesley Iberoamericana, 3ra ed., Madrid, 2000.

[2] R. H. Webb, *Elementary wave optics*, Dover publications, INC., 2nd ed., New York, 2005.

[3] A. Ghatak, *Optics*, Mc Graw Hill, 4th ed., New Delhi, 2009.

[4] E. Hetch, *Optics*, Addison Wesley, 4th ed., San Francisco CA, 2002.

[5] G. R. Fowles, *Introduction to modern optics*, Dover publications, INC., 2nd ed., New York, 1989.

[6] P. Drude, *The theory of optics*, Dover publications, INC., 1st. ed., New York, 1959.

[7] E. Hetch, *Optics*, Schaum’s outline of theory and problems of optics, McGraw-Hill, USA, 1975.

[8] K. D. Moller, *Optics*, University Science Books, California, 1st. ed., 1988.

[9] M. Born and E. Wolf, *Principles of optics*, Cambridge University Press, 7th. ed., Cambridge, 1999.

[10] J. R. Meyer-Arendt, *Introduction to classical and modern optics*, Prentice Hall, 1st Ed, N. J., 1972.

[11] A. A. Michelson, *Studies in Optics*, U. Chicago Press, Chicago, Ill., 1927.

[12] W. T. Silfvast, *Laser fundamentals*, Cambridge University Press, 2nd ed., 2004.

[13] R. D. Guenter, *Modern optics*, John Wiley & Sons, Canada, 1990.

[14]G. B. Parrent, and B. J Thompson, *Physical optics notebook*, Society of Photo-optical Instrumentation Engineers, California, 1969.

[15] D. Malacara, *Óptica básica*, Fondo de Cultura Económica, 2a ed., México, 2004.

[16] J. Strong, *Concepts of classical optics*, W. H. Freeman & Company, San Francisco, 1958.

[17] C. Huygens, *Treatise on light*, Dover publications, New York, 1962 (1690).

[18] J. W. Goodman, *Introduction to Fourier Optics*, McGraw-Hill international editions, 2nd ed., 1996.

[19] C E. J. Carreón González, “Síntesis de rejillas de fase bidimensionales mediante holografía binaria”, Tesis de maestría, INAOE, 1997.

[20] M. Abramowitz, and I. A. Stegun, *Handbook of mathematical functions with formulas, graphs, and mathematical tables*, Dover publications, INC., 9th ed., New York, 1972.

[21] E. Kreysig, *Matemáticas avanzadas para ingeniería Vol. II*, Limusa Wiley, 3a ed., México, 2000.

[22] K. Iizuka, *Elements of photonics Vol. 1*, Wiley-Interscience, New York, 2002.

[23] H. F. Talbot, “Facts relating to optical science No. IV”, Philos. Mag. 9, 401-407 (1836).

[24] H. Lord Rayleigh, “On copying diffraction gratings and on some phenomenon and its applications”, Philos. Mag. 11, 196-205 (1881).

[25] H A. W. Lohmann, *Optical information processing*, 2nd ed., Germany, 1978.

[26] J. W. Brown and R. V. Churchill, *Variable compleja y aplicaciones*, McGraw-Hill, 7a. ed., España, 2004.

[27] J. T. Winthrop and C. R. Worthington, “Theory of fresnel images. I. Plane periodic objects in monochromatic light”, J. Opt. Soc. Am. 55, 373-381 (1965).

[28] J. Ibarra and J. Ojeda-Castañeda, “Talbot interferometry: a new geometry”, Opt. Comm. 96, 294-301 (1993).

[29] J. C. Barreiro-Hervás, “Autoimágenes con luz espacialmente coherente e incoherente. Aplicaciones al procesado óptico de información”, Tesis de doctorado, Universitat de Valencia, Departamento de óptica, 1992.

[30] C. Frausto-Reyes, “Efecto Lau en la reducción de ruido multiplicativo”, Tesis de doctorado, INAOE, 1999.

[31] H. P. Hsu, *Análisis de Fourier*, Prentice Hall, 1st ed., México, 1998.

[32] E. Peli, “Contrast in complex images”, J. Opt. Soc. Am. A 7 (10), 2032-2040 (1990).

[33] G. C. Holts, *CCD Arrays, cameras and displays*, Society for photo-optical instrumentation engineers, 1996.

[34] E. Cuche, P. Marquet, and C. Depeursinge, “Simultaneous amplitude-contrast and quantitative phase-contrast microscopy by numerical reconstruction of Fresnel

off-axis holograms", Appl. Opt. 38 (34), 6994-7001 (1999).

[35] P. Hariharan, *Optical interferometry*, Academic, 1989.

[36] H. C. Hsieh, W. T. Wu, W. Y. Chang, Y. L. Chen, and D. C. Su, "Optimal sampling conditions for a commonly used charge-coupled device camera in the full-field heterodyne", Opt. Eng. 50 (4), 045601-045601-4 (2011).

[37] J. D. Briers, G. Richards, and X. W. He, "Capillary blood flow monitoring using laser speckle contrast analysis (LASCA)", J. Biomed. Opt. 4 (01), 164-175 (1999).

[38] P. Marquet, B. Rappaz, P. J. Magistretti, E. Cuche, Y. Emery, T. Colomb, and C. Depeursinge, "Digital holographic microscopy: a non-invasive contrast imaging technique allowing quantitative visualization of living cells with subwavelength axial accuracy", Opt. Lett. 30 (5), 468-470 (2005).

[39] L. M. Sanchez-Brea, J. A. Quiroga, A. Garcia-Botella, and E. Bernabeu, "Histogram-based method for contrast measurement", Appl. Opt. 39 (23), 4098-4106 (2000).

[40] S. Lai, and G. von Bally, "Fringe contrast evaluation by means of histograms", in *OPTIKA '98: 5th Congress on Modern Optics*, Proc. SPIE 3573, 384-387 (1998).

[41] L. M. Sanchez-Brea, F. J. Torcal-Milla, and E. Bernabeu, "On the standard deviation in charge-coupled device cameras: A variogram-based technique for nouniform images", J. Electron. Imaging 11 (2), 121-126 (2002).

[42] J. D. Irwin, *Análisis básico de circuitos en ingeniería*, Editorial Mc Graw Hill, 1988.

[43] J L. M. Sanchez-Brea, F.J. Torcal-Milla, and E. Bernabeu, "Variogram-based method for contrast measurement," Appl. Opt. 47 (22), 5027–5033 (2007).

[44] K. Tiippana, R. Nasanen, and J. Rovamo, "Contrast matching of two-dimensional compund gratings," Vision Res. 34, 1157-1163 (1994).

[45] D. C. Montgomery y G. C. Runger, *Probabilidad y estadística aplicadas a la ingeniería*, Editorial Mc Graw Hill, México,1994.

[46] D. C. Montgomery and G. C. Runger, *Applied statistics and probability for engineers*, Jonh Wiley & Sons, Inc., 3rd ed., New Jersey, 2003.

[47] P. Bex and W. Makous, "Spatial frequency, phase, and the contrast of natural images", J. Opt. Soc. Am. A. 19 (6), 1096-1106 (2002).

---

[48] B. Moulden, F. Kingdom, and L. F. Gatley, “The standard deviation of luminance as a metric for contrast in random-dot images”, Perception 19 (1), 79-101 (1990).

[49] G. Matheron, “Principles of geostatistics”, Econ. Geo. 58 (8), 1246-1266 (1963).

[50] H. Wackernagel, *Multivariate geostatistics. An introduction with applications*, Springer, 3rd ed., New York, 2003.

[51] G. Ramstein, and M. Raffy, “Analysis of the structure of radiometric remotely sensed images”, Int. J. Rem. Sens. 10 (6), 1049-1073 (1989).

[52] R. Barnes, “Variogram Tutorial”, Golden Software, Inc.

[53] I. Clark, *Practical geostatistics*, Applied Science Publishers Ltd., London, 1979.

[54] M. Armstrong, *Basic linear geostatistics*, Springer-Verlag, New York, 1997.

[55] A. G. Journel, and G. H. Huijbregts, *Mining geostatistics*, Academic Press, New York, 1978.

[56] O. Dubrule, *Geostatistics in petroleum geology*, American Association of Petroleum Geologists, Tulsa, Oklahoma, 1998.

[57] M. E. Hohn, *Geostatistics and petroleum geology*, Kluwer Academic Publishers, 2nd ed., Norwell, MA, U.S.A., 1998.

[58] R. E. Rossi, D. J. Mulla, A. G. Journel, and E. H. Franz, “Geostatistical tools for modelling and interpreting ecological spatial dependence”, Ecologycal Monographs 62 (2), 277-314 (1992).

[59] M. Durrieu, L. A. Ruiz, and A. Balanguer, “Analysis of geostatistical parmeters for texture classification of satellite images”, Procceedings of the 25th EARSeL Symposium, Porto, Portugal, 11-18 (2005).

[60] M. Chica-Olmo, and F. Abarca-Hernández, “Computing geostatistical image texture for remotely sensed data classification”, Computers and Geosciences 26 (4), 373-383 (2000).

[61] J. R. Carr, “The semivariogram in comparison of the co-occurrence matrix for classification of image texture”, IEEE Transactions on Geoscience and Remote Sensing 36 (6), 1945-1952 (1998).

[62] J E. H. Isaaks, and R. M. Srivastava, *An introduction to applied geostatistics*, Oxford University Press, New York, 1989.

[63] N. M. A. Daley, C. N. Burnett, M. Wulder, K. O. Niemann, and D. G. Goodenough, “Comparison of fixed-size and variable-sized windows for the

estimation of tree crown position", IEEE International Geoscience and Remote Sensing Symposium, 1323-1325 (1998).

[64] P. J. Curran, "The semivariogram in remote sensing: An introduction", Rem. Sens. Env. 24 (3), 493-507 (1988).

[65] P. M. Atkinson, "The effect of spatial resolution on the experimental variogram of airborne MSS imagery", Int. J. Rem. Sens. 14 (5), 1005-1011 (1993).

[66] M. F. Goodchild, *Spatial autocorrelation*, Concepts and Techniques in Modern Geography, Geo Books, Norwich, 1986.

[67] L. Bian, and Z. Xie, "A spatial dependence approach to retrieving industrial complexes from digital images", the Professional Geographer 56 (3), 381-393 (2004).

[68] S. Franklin, M. Wulder, and M. Laigne, "Automated derivation of geographic windows sizes for use in remote sensing digital image texture analysis", Computers & Geosciences 22 (6), 665-673 (1996).

[69] N. A. Cressie, *Statistics for Spatial Data*, John Wiley and Sons, New York, 1991.

[70] M. Petrov, S. Stepanov, and A. Khomenko, *Photorefractive crystals in coherent optics*, Springer, Berlin, 1991.

[71] P. V. Mitchell, S. W. McCahon, M. B. Klein, T. R. O'Meara, G. J. Dunning, D. M. Pepper, Tech. Digest of Photorefractive Materials, Effects and Applications, Conference Aspen, Lodge, USA (1995). .

[72] S. Stepanov, "Sensitivity of non steady-state photo electromotive force-based adaptive photodetector and characterization techniques", Appl. Opt. 33 (6), 915-917 (1994).

[73]. I. Sokolov, S. Stepanov and G. Trofimov, "Measurements of small vibration amplitudes of the diffuse objects using adaptive *GaAs:Cr* photodetectors", Sov. Acoustic J. 37 (5), 519-521 (1991).

[74] M. L. Arroyo-Carrasco, P. Rodriguez-Montero, and S. Stepanov, "Measurement of the coherence length of diffusely scattered laser beams with adaptive photodetectors", Opt. Commun. 157 (1-6), 105-110 (1998).

[75] S. Stepanov, P. Rodriguez-Montero, S. Trivedi, and C. C. Wang, "Effective broadband detection of nanometer laser-induced ultrasonic surface displacements by *CdTe:V* adaptive photoelectromotive force detector," Appl. Phys. Lett. 84 (3), 446-448 (2004).

[76] J. Castillo-Mixcóatl, "Optimización de un fotodetector adaptivo de *GaAs* basado

en el efecto foto-FEM, para aplicaciones de detección de ultrasonido", Tesis de doctorado, INAOE, 2003.

[77] P. Rodriguez-Montero, S. Trivedi, F. Jin, C. C. Wang, S. Stepanov, G. Elliott, J. F. Meyers, J. Lee, and J. Khurgin, "Pulsed-laser vibrometer using photoelectromotive-force sensors", Appl. Phys. Lett. 83 (9), 1893-1895 (2003).

[78] Y. Ding, I. Lahiri, D. Nolte, G. J. Dunning, and D. M. Pepper, "Electric-field correlation of femtosecond pulses by use of a photo-electromotive force detector", J. Opt. Soc. Am. B 15, (7) 2013-2017 (1998).

[79] Y M. C. Gather, S. Mansurova, and K. Meerholz, "Determining the photoelectric parameters of an organic photoconductor by the photoelectromotrive-force technique", Phys. Rev. B 75, (16) 165203-165212 (2007).

[80] M. Petrov, I. Sokolov, S. Stepanov and G. Trofimov, "Non-steady-state photo-electromotive-force induced by dynamic gratings in partially compensated photoconductors", J. Appl. Phys. 68 (5), 2216-2225 (1990).

[81] S. Stepanov, *Photo-electromotive-force in semiconductors*, Handbook of Advanced Electronic and Photonics Materials and Devices, Vol. II, Academic Press, 2001.

[82] L. Solimar, D. J. Webb, and A. Grunnet-Jepsen, *The physics and application of photorefractive materials*, Claredon Press, Oxford, 1996.

[83] A. Aguirre-López, "Investigación y optimización de un fotodetector adaptivo basado en el efecto foto-FEM", Tesis de maestría, INAOE, 2000.

[84] N. Korneev, S. Mansurova, S. Stepanov, T. J. Hall, and A. K. Powell, "Non-steady-state photo-electromotive force in semiconductor photorefractive crystals biased by dc field", J. Opt. Soc. Am. B 13 (10), 2278-2285 (1996).

[85] I. Sokolov and S. Stepanov, "Non-steady-state photo-electromotive force in crystals with long photocarrier lifetimes", J. Opt. Soc. Am. B 8 (10), 1483-1488 (1993).

[86] J. A. Edminister, *Circuitos electrónicos*, Mc Graw Hill, 2a ed., México (1986).

[87] I. Sokolov and S. Stepanov, "Detection of optical signals with high-amplitude phase modulation by adaptive photodetectors", Appl. Opt. 32 (11) 1958-1964 (1993).

[88] P. Rodriguez-Montero, C. M. Gomez-Sarabia, and J. Ojeda-Castañeda, "Adaptive photodetector for assisted Talbot effect", Appl. Opt. 47 (21), 3778-3783 (2008).

Chapter 3

Experimental Methods

3.1 Introduction

This chapter gives a general description of the experimental arrangements, equipment, and materials used for the localization and analysis of the diffraction patterns generated by a Ronchi grating. Two principle schemes are described: the first one that uses an adaptive photodetector based on the non-steady-state photo-electromotive force (photo-EMF) effect and the second one uses CCD as an input sensor (RMS and semivariogram techniques). The relevant characteristics of devices used in the experiments are presented. The main characteristics of experimental methods for characterizations and localization of the Talbot patterns are discussed.

3.2 Description of experimental setup for self-images generation

A schematic of the experimental arrangement for self-images generation is shown in Fig. 3.2. The experiments were basically performed with a standard Melles Griot *He-Ne* laser linearly polarized with a wavelength $\lambda \approx 633\,nm$ and an output power of approximately $11\,mW$.

Using a $10\,x$ microscope objective the beam from the laser was expanded and pinhole with a diameter equal to $10\,\mu m$ was used to filter out the light. The diverging beam was incident on the collimating lens of focal length $20\,cm$. This collimated beam illuminated the binary grating.

A binary grating, also called Ronchi grating or Ronchi ruling consists in alternate dark and clear stripes. The geometry of a Ronchi grating is illustrated in Fig. 3.1, where A is the amplitude, and Λ is the period of the slit. These gratings usually are used for optical testing purposes. In the experiments, a binary grating with a period of $\Lambda = 100\,\mu m$, i.e. $10{,}000\ lines/m$ is used.

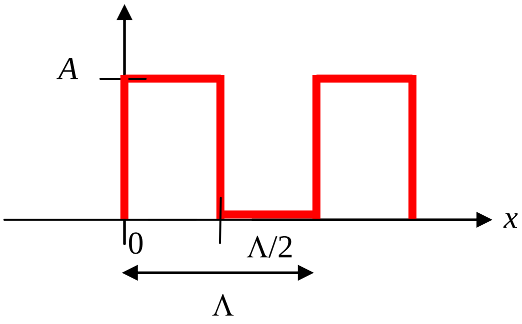

Fig. 3.1. Geometry of a Ronchi grating.

The expected Talbot distance (where the self-images are located) was estimating by the equation $z_T = 2\Lambda^2/\lambda$. Substituting the period of the grating and the wavelength, the value for the Talbot distance is approximately $z_T \approx 31.6\,mm$.

Both detectors (photo-EMF detector or CCD camera) were mounted in a Newport translation stage (the resolution of its milimetric screw was approximately $5\,\mu m$ with steps of $10\,\mu m$) for scanning along the optical axis z, and were placed around $5th$ self-image (approximately $15\,cm$ from the grating where the self-image had better contrast).

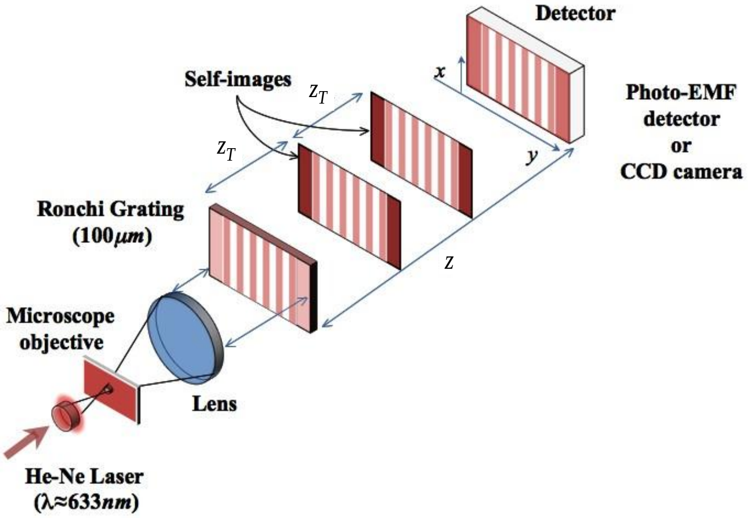

Fig. 3.2. Schematic diagram of experimental set-up for self-images generation.

3.3 Characterization of adaptive photodetectors

The experimental setup for the characterization of adaptive photodetectors is presented in Fig. 3.3. The experiments were performed with the same Melles Griot *He-Ne* laser.

The beam from the laser passed through a beam splitter and was divided into two beams, which intersected on the surface of the photoconductive crystal (adaptive photodetector) and produced interference fringes.

A mirror was attached to the piezo-electric transducer to induce the vibrations of the interference fringes. The piezo-electric was driven by the signal generator, which also provided the reference signal to the lock-in amplifier. Finally, the lock-in amplifier detected the photo-EMF signal.

The frequency of excitation from the function generator was approximately $1\,kHz$ and the amplitude applied to the piezo-electric was approximately $20\,Vpp$, which ensures that the condition $\Delta << 1$ holds in our experiment.

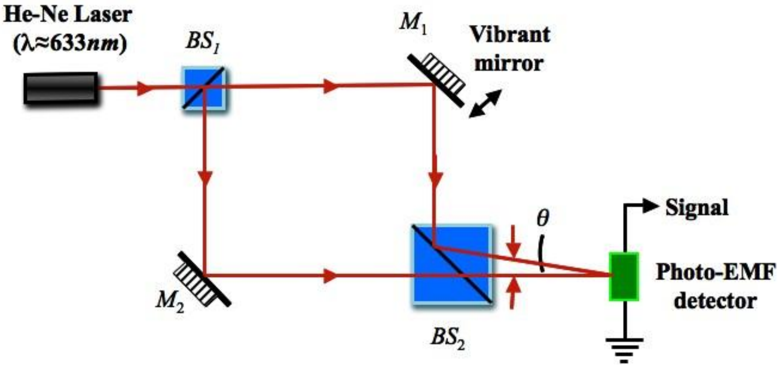

Fig. 3.3. Experimental setup for characterization of photo-EMF detectors. Here M_1 and M_2 are mirrors, BS_1 and BS_2 are beam splitters, and θ is the angle.

The experiments were carried out with two crystals (principally), which consisted in a semi-insulating *GaAs* crystals, with a pair of silver paste electrodes deposited onto the front face. The dimensions of the crystals are shown in the next figures.

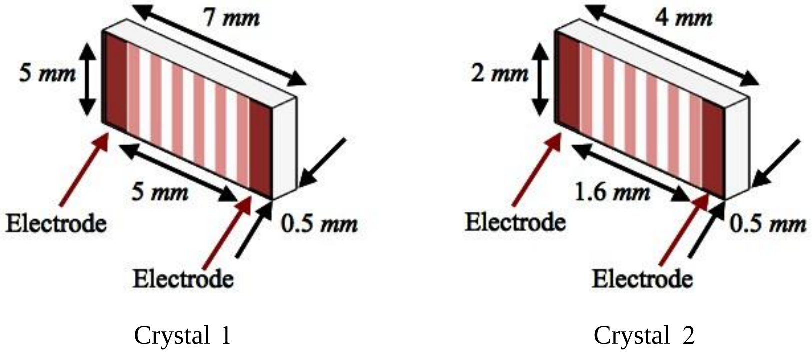

Fig. 3.4. Dimensions of adaptive photodetectors.

In Fig. 3.5 and Fig. 3.6 the dependence of photo-EMF signal as function of the beam crossing angle can be observed.

As it is shown in Fig. 3.5 and Fig. 3.6, the photo-EMF current behavior with the variations of beam crossing angle is consistent with the predictions of standard theory of the photo-EMF effect [1] when the beam crossing angle increases the photo-EMF signal grows up linearly until it reaches a maximum and then the signal decays.

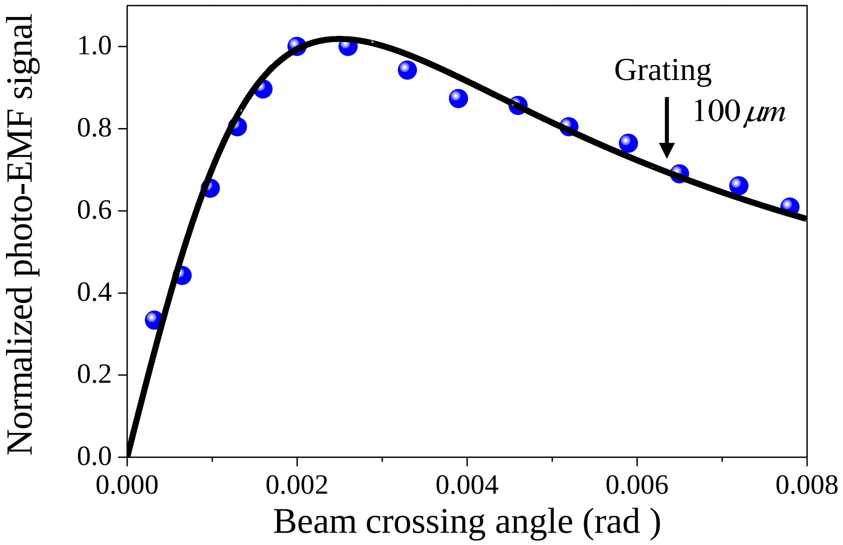

Fig. 3.5 Dependence of the photo-EMF signal as a function of the beam crossing angle for crystal 1.

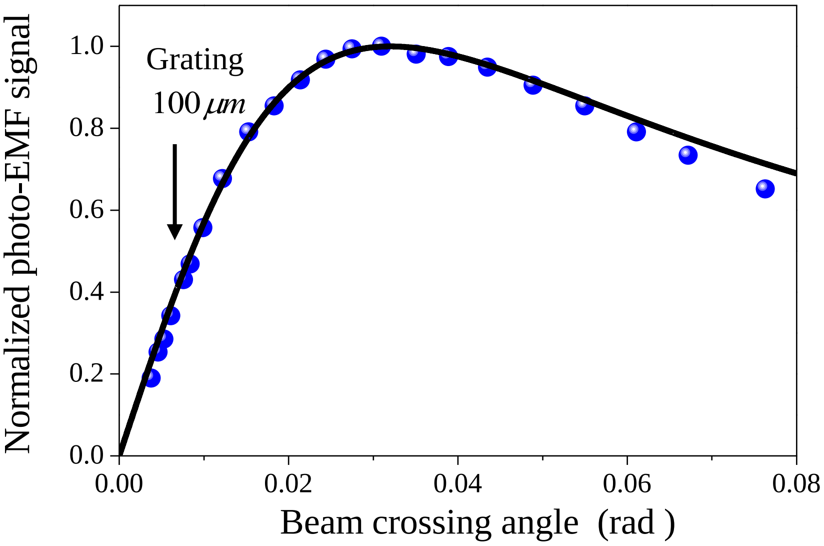

Fig. 3.6. Dependence of the photo-EMF signal as a function of the beam crossing angle for crystal 2.

Solid line in Fig. 3.5 and Fig. 3.6 are the theoretical fitting of experimental data. It is well known (see Ref. 2) that the maximum of the photo-EMF signal occurs when the product of spatial frequency of the interference fringes and diffusion length equals to one $KL_D = 1$, so the carriers' diffusion length can be determined from the maxima position.

$$L_D = K_{\max}^{-1} = \frac{\Lambda_{\max}}{2\pi}. \qquad \textbf{(3.1)}$$

In paraxial approximation (for small angles) the period of fringes can be approximated as $\Lambda \approx \lambda / \theta$, obtaining $L_D = \lambda / 2\pi\theta_{\max}$.

Fitting of theoretical results gave the values of 0.0025 rad and 0.032 rad for the values of beam crossing angles at which maximal photo-EMF signal have been observed. Using the expression (Eq. 3.1), the carriers' diffusion length L_D was approximately 40 μm for crystal 1 and 3 μm for crystal 2.

3.4 Description of detection system of self-images

Two kinds of experiments were performed: first one consists in acquiring images by CCD camera with posterior image processing and analysis by RMS and semivariogram-based methods, and the second one uses the adaptive photo-EMF detector.

3.4.1 CCD

For CCD-based experiments (see Fig. 3.7) the light distribution was scanned along the optical axis z (moving the translation stage) with steps of $1mm$.

In each step an image of the light pattern (512 x 480 pixels in size) was recorded by a CCD video camera. This is a SONY device and corresponds to XC-75 series. The XC-75 is a monochrome instrument with a total number of pixels of [811(H) x 508(V)].

All the images recorded, were processed using software of CCD camera [beam analyzer (Spiricon)] in order to determine the intensity distributions generated by binary grating. These data (the intensity distributions) were processed using RMS and semivariogram algorithms. Finally, the numerical computations of these algorithms were realized with two different programs (Octave [3] and Matlab).

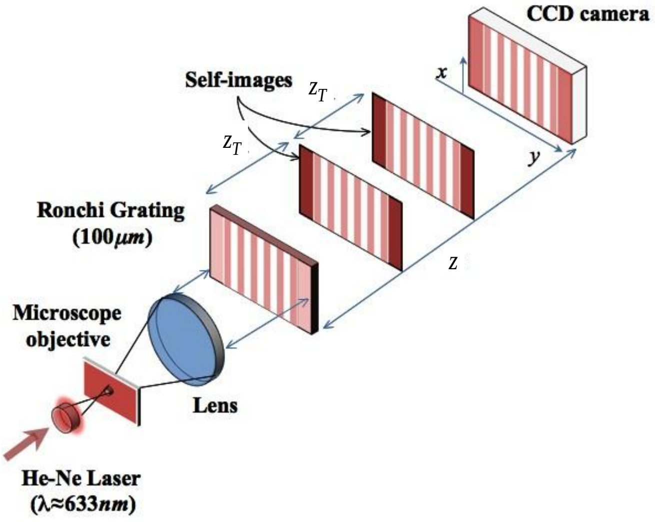

Fig. 3.7. Schematic diagram of experimental set-up for CCD camera.

In Fig. 3.8, as an example, the image captured by CCD camera at a distance $z = 5z_T$ that corresponds to a self-image of the binary grating is shown.

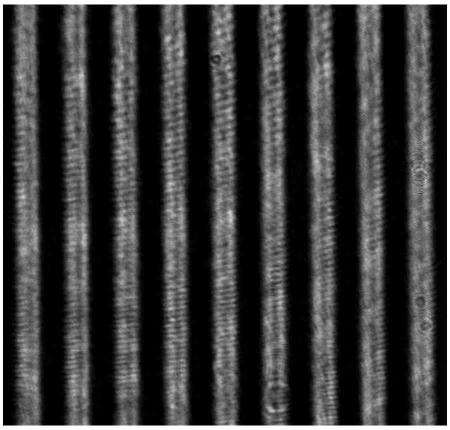

Fig. 3.8. Image of Talbot self-image for the binary grating recorded by CCD camera.

It is important to mention that for CCD experiments, a filter was used for avoid saturation of the camera.

3.4.2 Photo-EMF

In the photo-EMF experiments (see Fig. 3.9) the binary grating was attached to the piezo-electric transducer to induce vibrations of the light patterns.

To achieve the requisite of small phase modulation $\Delta << 1$ the piezo-electric transducer was set to generate amplitude of vibrations smaller than the wavelength of the laser. Therefore, the piezo-electric was exited with a frequency of $600 Hz$ and with amplitude of $11 Vpp$ by the function generator.

The ac current induced by a vibrating light pattern was detected by an adaptive photodetector placed on a translation stage. The crystal 1 described in Section 3.3 was used as photodetector.

The photo-EMF signal was scanned along the optical axis z with steps of $1\,mm$ and $250\,\mu m$ moving the translation stage. A SR530 lock-in amplifier detected photo-EMF current generated by the photodetector, with an input resistance of $100\,M\Omega$ and an input capacitance of $25\,pF$, by a coaxial cable connected to the silver electrodes of the photodetector. The SR530 is an instrument that can measure AC signals as nanovolts in the presence of much larger noise levels.

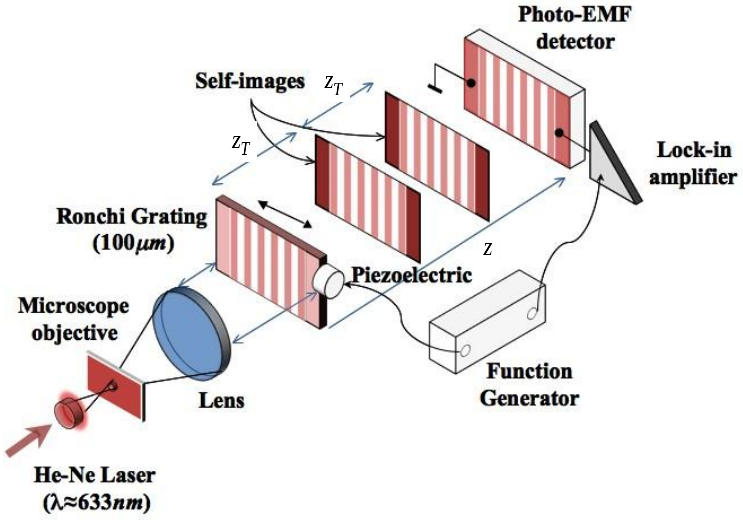

Fig. 3.9. Details of photo-EMF based arrangement.

3.4.2.1 Characterization of the piezo-electric

In Fig. 3.10 the results of the dependence of photo-EMF signal as a function of the peak to peak voltage Vpp applied to the piezo-electric are observed. In this case the frequency of excitation from the function generator was fixed in $600\,Hz$ and the Vpp applied to the piezo-electric varied from 1 to 20.

The behavior of the results (Fig. 3.10) shows that when the Vpp increase the photo-EMF signal grows linearly.

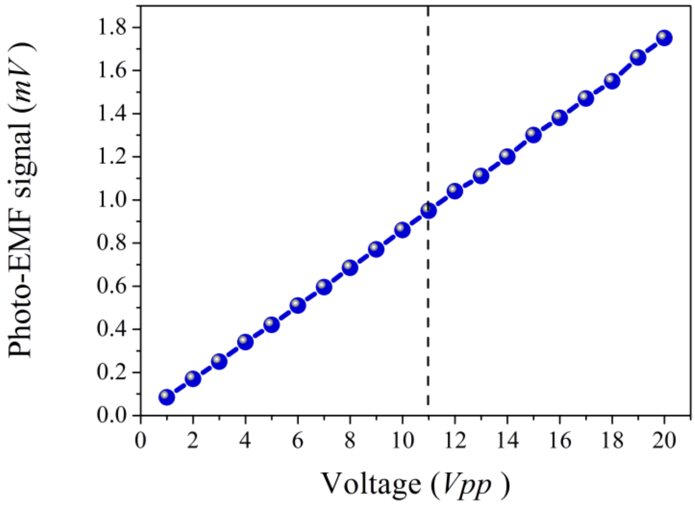

Fig. 3.10. Dependence of photo-EMF signal as a function of the Vpp. Here the wavelength $\lambda \approx 633\,nm$, the output power of $\approx 11\,mW$, and with a frequency of $600\,Hz$.

In Fig. 3.11 the results of the dependence of photo-EMF signal as function of the frequency applied to the piezo-electric are observed. In this case the amplitude from the function generator was fixed on $11Vpp$. The frequency of excitation varies from $400\,Hz$ to $800\,Hz$. Here, the maximum of the signal is located at approximately $600\,Hz$ i.e. the frequency approaches to resonance frequency of piezoelectric transducer. In our experiments this frequency of modulation was used, since it ensures the large modulation amplitudes.

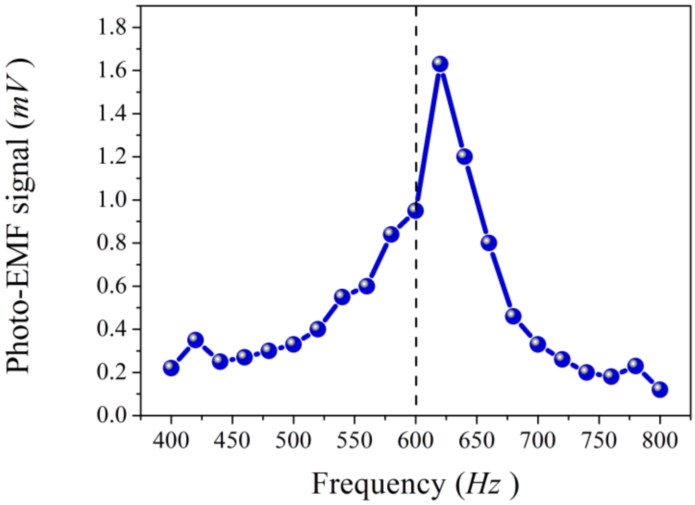

Fig. 3.11. Dependence of photo-EMF signal as a function of the frequency. Here the wavelength $\lambda \approx 633\,nm$, the output power of $\approx 11\,mW$, and with amplitude of $11\,Vpp$.

In Fig. 3.12 the results of the dependence of photo-EMF signal as a function of the output power are shown. In this case the amplitude from the function generator was fixed on $11 Vpp$ and the frequency in $600\ Hz$. A filter modified the output power and it varies from $1\,mW$ to approximately $11\,mW$. Here, the photo-EMF signal grows linearly as a function of the output power.

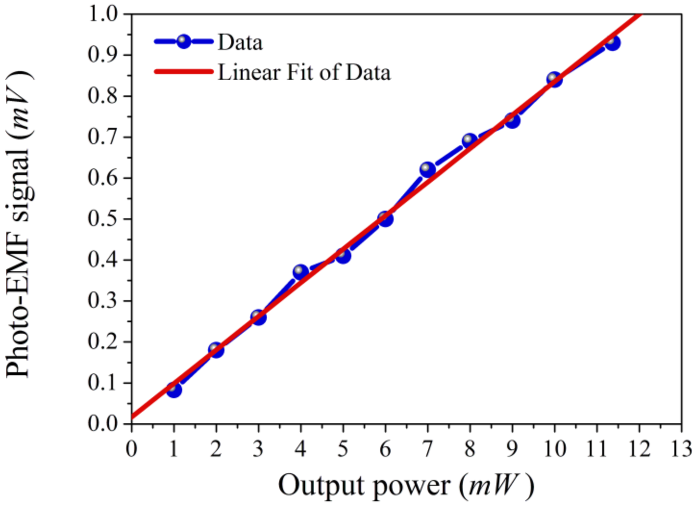

Fig. 3.12. Dependence of photo-EMF signal as a function of the output power. Here the wavelength $\lambda \approx 633\,nm$, with a frequency of $600\,Hz$, and with amplitude of $11\,Vpp$.

In Fig. 3.13 the results of the dependence of the distance between self-images versus position of the collimation lens are shown.

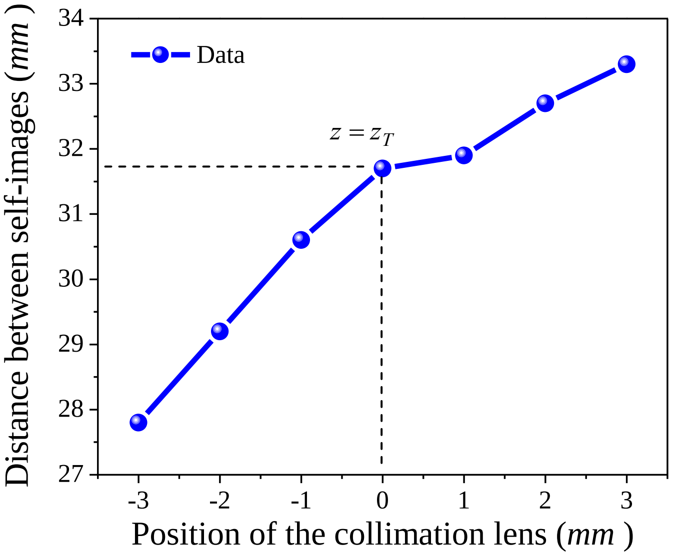

Fig. 3.13. Dependence of the distance between self-images versus position of the collimation lens. Here the wavelength $\lambda \approx 633\,nm$, the output power of $\approx 11\,mW$, with a frequency of $600\,Hz$,

and with amplitude of $11\,Vpp$.

In this case the amplitude from the function generator was fixed on $11Vpp$ and the frequency in $600\,Hz$. The collimation lens was mounted in a translation stage for scanning along the optical axis z, and was placed close to $5th$ self-image (approximately $15\,cm$ from the grating where the self-image had better contrast). The distance was scanned along the optical axis z with steps of $1\,mm$ moving the translation stage.

Here, the distance between self-images has a linear trend as function of the position of the collimation lens.

3.5 Description of detection system of self-images for turbid media

The possibility for localization of self-images in turbid media was also investigated. A turbid media can be defined as a medium that contain suspended particles that scattering light in all directions under illumination.

To carry out the experiments of the localization of Talbot self-images, a glass cell that contained different concentrations of semi-skimmed milk (Parmalat brand), as a strongly-scattering or turbid media, diluted in deionized water was used.

Milk is an opaque white fluid. The chemical composition of the milk is complex, is a colloid of butterfat globules within a water-based fluid, and shows analogy with blood [4]. The appearance of the milk is determined by its optical properties. Light scattering by fat globules and caseins micelles causes milk to appear turbid and opaque [5].

Hence, the experimental arrangement for localization of self-images in turbid media for photo-EMF detector is observed in Fig. 3.14.

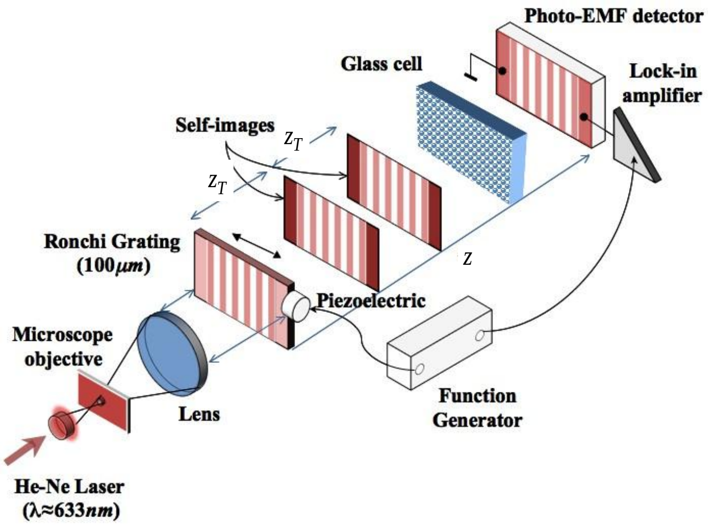

Fig. 3.14. Details of photo-EMF based arrangement with glass cell.

3.6 Analysis of diffraction orders collected by system

If a screen or detector is placed some distance away from the grating, the light intensity coming from the grating produces several spots, which corresponding to different orders of diffraction (see Fig. 3.15). In fact, for a grating a mathematical relationship can be derived which relates the angle of the diffraction θ, the period of the grating Λ, the wavelength λ, and the diffraction orders m, this is called the grating equation [6,7] and is given by:

$$m = \frac{\Lambda \sin\theta}{\lambda}, \tag{3.2}$$

where $\theta = \tan^{-1}(y/5z_T) = \tan^{-1}(y/158\,mm)$. For the experimental analysis the number of diffraction orders collected by the system (both detectors) was calculated using Eq. (3.2), and substituting the period of the grating $\Lambda = 100\ \mu m$, the wavelength $\lambda = 633\,nm$, and the angle θ.

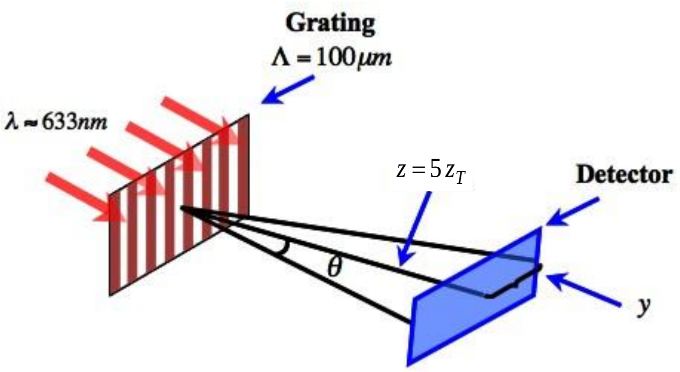

Fig. 3.15. Diagram for calculation of the diffraction orders collected by the system.

It was found that in general three diffraction orders were collected ($m = \pm 3$) [see Fig. (3.16)].

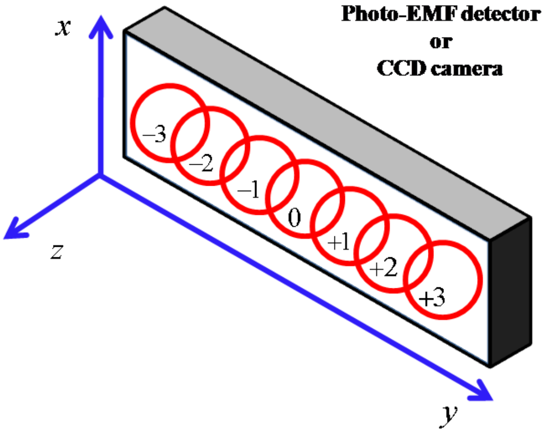

Fig. 3.16. Diagram of the diffraction orders collected by the system.

3.7 References

---

[1] S. Stepanov, *Photo-electromotive-force in semiconductors*, Handbook of Advanced Electronic and Photonic Materials and Devices, Vol. II, Academic Press, 2001.

[2] M. Petrov, I. Sokolov, S. Stepanov and G. Trofimov, “Non-steady-state photo-electromotive-force induced by dynamic gratings in partially compensated photoconductors”, J. Appl. Phys. 68 (5), 2216-2225 (1990).

[3] Gnu Octave is a high-level language, primarily intended for numerical

---

computations (www.octave.org).

[4] Ch. Alais, *Ciencia de la leche: Principios de técnica lechera*, Editorial Reverté, 4a ed., España, 2003.

[5] M. C. Y M. Peña-Gomar, “Reflectometría laser de barrido en ángulo cerca del ángulo crítico”, Tesis de maestría, INAOE, 2002.

[6] E. Hetch, *Óptica*, Addison Wesley Iberoamericana, 3ra ed., Madrid, 2000.

[7] R. D. Guenter, *Modern optics*, John Wiley & Sons, Canada, 1990.

Chapter 4

Non-steady-state photo-EMF effect induced by an arbitrary periodical one-dimensional light pattern

4.1 Introduction

In this chapter detailed theoretical analysis for non-steady-state photo-EMF effect induced by a periodical one-dimensional (1-D) light pattern in a photoconductive sample is developed. As a result of this analysis the expression for photo-EMF current density induced by light distribution containing only odd harmonics is derived. This expression was used to analyze an axial distribution of photo-EMF current produced by light pattern generated by diffraction in binary grating on near field. Next to the theoretical analysis, experimental results on investigation of photo-EMF effect induced by light patterns produced by Fresnel diffraction on Ronchi grating using *GaAs* detector at different experimental conditions are presented. Finally, the discussion of the obtained results is performed.

4.2 Theoretical analysis

4.2.1 Incident light distribution

First, an infinite photoconductor illuminated by an arbitrary one-dimensional (1-D) periodical (with a period Λ) light pattern with the intensity distribution $I(x)$ is considered. The periodical function $I(x)$ can be represented in terms of Fourier [1,2] series:

$$I(x,t) = \sum_{l=-\infty}^{\infty} A_l e^{ilKx}, \tag{4. 1}$$

where $K = 2\pi/\Lambda$ is the fundamental spatial frequency, l is the number of spatial harmonic and the coefficients A_l are defined as:

$$A_l = \frac{1}{\Lambda} \int_0^{\Lambda} I(x)\, e^{-ilKx}\, dx. \tag{4. 2}$$

If the light pattern is oscillating periodically in time with a frequency Ω and amplitude Δ, then the resulting spatial and temporal dependence of $I(x,t)$ can be written as [3]:

$$I(x,t) = \sum_{l=-\infty}^{\infty} A_l e^{il\,(Kx+\Delta\,\sin\Omega t)} = \sum_{l=-\infty}^{\infty} A_l e^{ilKx}\, e^{il\,\Delta\,\sin\Omega t}, \tag{4. 3}$$

Considering small amplitude of vibrations $\Delta << 1$, the exponential function can be expanded on Taylor series [4] where only the linear term is left:

$$e^{il\,(\Delta\,\sin\Omega t)} \cong 1 + il\,\Delta\,\sin\Omega t + \ldots \tag{4. 4}$$

Using Euler's formula [5]:

$$\sin\Omega t = \frac{e^{i\Omega t} + e^{-i\Omega t}}{2i}. \tag{4. 5}$$

The expression for the intensity distribution can be represented by the following series:

$$\begin{aligned} I(x,t) &= \sum_{l=-\infty}^{\infty} \left[A_{l0} e^{ilKx} + A_{l0} \frac{\Delta l}{2} e^{i(lKx+\Omega t)} + A_{l0} \frac{\Delta l}{2} e^{i(lKx-\Omega t)} \right], \\ &= \sum_{l=-\infty}^{\infty} [A_{l0} e^{ilKx} + A_{l1} e^{i(lKx+\Omega t)} + A_{l-1} e^{i(lKx-\Omega t)}], \end{aligned} \tag{4. 6}$$

where

$$A_{l1} = A_{l0} \frac{\Delta\, l}{2}, \text{ and } A_{l-1} = -A_{l0} \frac{\Delta\, l}{2}, \tag{4. 7}$$

here the first sub-index indicates the number of spatial harmonic and the second one is the number of temporal harmonic.

4.2.2 Main equations of the theoretical description of the photo-EMF effect in monopolar photoconductor

Next, let us consider the main equations, which we are planning to use in our theoretical analysis. For the simplicity the widely assumed model of a monopolar (*n*-type) photoconductor with a single deep impurity level is used. The recombination that occurs through the same deep trap level is used. Dark conductivity (due to the thermal excitation) and saturation of the impurity centers are neglected. Besides, no external bias is applied to the sample $\left(E_0 = 0\right)$.

Absorption of light photon leads to the excitation of the mobile electron from the impurity center with the generation rate g. The mobile carriers are driven by drift and/or diffusion and they are redistributed on the conduction band. After some time, defined as a recombination time τ, their recombine on available acceptor level.

The standard set of equations [(2.54) - (2.58)] – balance equation, current equation, continuity and Poisson equations – have been used in order to describe the processes of charge generation transport and trapping, as well as the process of space charge field formation.

Once again, in order to simplify the solution of the set of equations [(2.54) - (2.58)], the quasi-stationary condition, which is valid when the carriers' lifetime τ is negligible compared to any other characteristic time of the process: period of oscillations T and dielectric relaxation time τ_{di} is assumed. This approximation allows neglecting the temporal derivatives $\partial n / \partial t \approx 0$ and, combining the equations [(2.54) - (2.58)], two master equations are obtained:

$$0 = g(x,t) - \frac{n(x,t)}{\tau} + \left(\mu n(x,t) \frac{\partial E}{\partial x} + \mu E \frac{\partial n}{\partial x} + D \frac{\partial^2 n}{\partial x^2} \right). \qquad \textbf{(4. 8)}$$

$$\frac{\partial^2 E(x,t)}{\partial x \partial t} = \frac{e}{\varepsilon \varepsilon_0} \frac{\partial N^+}{\partial t} = \frac{e}{\varepsilon \varepsilon_0} \left(g - \frac{n}{\tau} \right) = -\frac{e}{\varepsilon \varepsilon_0} \left(\mu n \frac{\partial E}{\partial x} + \mu E \frac{\partial n}{\partial x} + D \frac{\partial^2 n}{\partial x^2} \right). \qquad \textbf{(4. 9)}$$

4.2.3 Solution in linear approximation

The set of equations [(4.8) and (4.9)] cannot be solved analytically. The usual approach is to get analytical solution applying a linearization procedure assuming an approximation of **low (or small) contrast** of spatial modulation:

$$A_l / A_0 << 1. \tag{4. 10}$$

The value of contrast can be controlled by an additional uniform illumination or if the grating with the transmittance different from 0 and 1.

Then, all unknown variables can be written in a similar way to that of the input excitation [Eq. (4.3)]. This allows writing [6]:

$$E(x,t) = \sum_{l=0}^{\infty} E_{l0}\, e^{ilKx} + E_{l1}\, e^{i(lKx+\Omega t)} + E_{l-1}\, e^{i(lKx-\Omega t)} + c.c., \tag{4. 11}$$

$$n(x,t) = \sum_{l=0}^{\infty} n_{l0}\, e^{ilKx} + n_{l1}\, e^{i(lKx+\Omega t)} + n_{l-1}\, e^{i(lKx-\Omega t)} + c.c.. \tag{4. 12}$$

The next step is to find the complex amplitude of space charge field $E(x,t)$ and the concentration distribution $n(x,t)$.

Here, the input light distribution contains only odd harmonics $l = 1, 3, \ldots$ (like e.g. in case of a binary grating). Substituting Eq. (4.8) and (4.9) to Eq. (2.57) and (2.58) the expressions for n_{lm} and E_{lm} can be obtained.

4.2.4 Steady-state solution

The solution for steady-state distribution of charge carriers' concentration yields:

$$n_{l0} = g_{l0}\ \tau, \tag{4. 13}$$

where n_{l0} is the average concentration of photoelectrons, and g_{l0} is the average photogeneration rate of the carriers.

Next, the expression for E_{l0} can be obtained. Since odd harmonics only are presented Eq. (4.9) can be written in a following way:

$$\mu n_0 \frac{\partial E_{l0}\, e^{ilKx}}{\partial x} + \mu E_0 \frac{\partial n_{l0}\, e^{ilKx}}{\partial x} + D \frac{\partial^2 n_{l0}\, e^{ilKx}}{\partial x^2} = 0. \qquad \textbf{(4. 14)}$$

Applying the partial derivative $\partial/\partial x$ one can obtain:

$$\mu n_0\, E_{l0}\, iKl + D\, n_{l0}\, (iKl)^2 = 0, \qquad \textbf{(4. 15)}$$

$$E_{l0} = -iKl \frac{D}{\mu} \frac{A_{l0}}{A_{00}}. \qquad \textbf{(4. 16)}$$

One can see that this result is quite similar to that obtained in case of sinusoidal light distribution: the $l\,th$ spatial harmonic of space-charge field is proportional to the modulation depth of the corresponding intensity distribution harmonic, and to the diffusion field $E_{Dl} = (KlD/\mu)$.

4.2.5 Solution for the first temporal harmonics

Now, the expression for first temporal harmonics of space charge field distribution E_{l1} and carriers' concentration n_{l1} can be obtained. Using master equations and applying temporal and spatial derivatives, one can get:

$$E_{l1}(iKl)(i\Omega) = -\frac{e}{\varepsilon\varepsilon_0}[\mu n_0 E_{l1} iKl + D n_{l1} (iKl)^2], \qquad \textbf{(4. 17)}$$

$$E_{l1} = -il \frac{n_{l1}}{n_0} \frac{1}{[i\Omega\tau_{di} + 1]} E_D, \qquad \textbf{(4. 18)}$$

where $E_D = (KD/\mu)$ is the diffusion electric field.

Using the first master equation [Eq. (4.8)] and Eq. (4.9), the expression for n_{l1} can be written as following:

$$0 = g_{l1} - \frac{n_{l1}}{\tau} + [\mu n_0 E_{l1} iKl + D n_{l1} (iKl)^2], \qquad \textbf{(4. 19)}$$

$$\frac{n_{l1}}{n_0} = \frac{A_{l1}}{A_0}\left[\frac{(i\Omega\tau_{di} + 1)}{(i\Omega\tau_{di} + 1)(1 + L_D^2 K^2 l^2) - L_D^2 K^2 l^2}\right] = \frac{A_{l1}}{A_0} \frac{(i\Omega\tau_{di} + 1)}{1 + i\Omega\tau_{di}(1 + L_D^2 K^2 l^2)}. \qquad \textbf{(4. 20)}$$

The result of Eq. (4.20) can be substituted into Eq. (4.18), and E_{l1} can be finally expressed as:

$$E_{l1} = -ilE_D\left[\frac{A_{l1}}{A_0}\frac{1}{1+i\Omega\tau_{di}\left(1+L_D^2K^2l^2\right)}\right] = \left(-ilE_D\right)\frac{A_{l1}}{A_0}\frac{1}{\left(1+i\Omega\tau_{scl}\right)}, \qquad \textbf{(4. 21)}$$

where

$$\frac{A_{l1}}{A_0} = \frac{A_l}{A_0}\frac{\Delta l}{2}, \qquad \textbf{(4. 22)}$$

and the term τ_{scl} is the space charge field build-up time to $l\,th$ harmonic given by the expression $\tau_{scl} = \tau_{di}\left(1+K^2L_D^2l^2\right)$.

Note, that in case of short diffusion lengths $lKL_D << 1$ the characteristic time of space charge electric field recording is the same for all spatial harmonics and it is determined by the dielectric relaxation time $\tau_{scl} \cong \tau_{di}$. For the opposite case of large diffusion lengths $lKL_D >> 1$ the expression for the characteristic time becomes $\tau_{scl} \cong \tau_{di}\left(K^2L_D^2l^2\right)$ and it is clear that higher harmonics possess longer recording time.

4.2.6 Photo-EMF current density

Total current flowing through the short-circuited photoconductor with Ohmic contacts can be calculated using the equation derived in reference [3]:

$$J_{photo\text{-}EMF} = \frac{e\mu}{\Lambda}\int_0^{\Lambda} E(x,t)\,n(x,t)\,dx. \qquad \textbf{(4. 23)}$$

It can be shown that substituting Eq. [(4.11) and (4.12)] into Eq. (4.23) three components of current appear, corresponding to DC current, to the fundamental and to the second temporal harmonic:

$$J_{photo\text{-}EMF} = e\mu\sum_{l=-\infty}^{\infty}\left[E_{l0}\,e^{ilkx} + E_{l1}\,e^{i(lkx+\Omega t)} + E_{l-1}\,e^{i(lkx-\Omega t)} + c.c\right]\times$$

$$e\mu\sum_{l=-\infty}^{\infty}\left[n_{l0}\,e^{ilkx} + n_{l1}\,e^{i(lkx+\Omega t)} + n_{l-1}\,e^{i(lkx-\Omega t)} + c.c\right] \qquad \textbf{(4. 24)}$$

$$J_{photo\text{-}EMF} = J_0 + J^{\Omega}_{photo\text{-}EMF}\,e^{i\Omega t} + J^{2\Omega}_{photo\text{-}EMF}\,e^{i2\Omega t} + c.c.$$

Now, the interest is the analysis of photo-EMF current at fundamental temporal harmonic. Reducing Eq. (4.24) one can show that the complex amplitude of photo-EMF total current density is given by the expression:

$$\begin{aligned} J^{\Omega}_{photo\text{-}EMF} &= e\mu\left\{\sum_{l=-\infty}^{\infty}\left[E_{l0}n_{l-1} + E_{l0}n_{l1} + E_{l-1}n_{l0} + E_{l1}n_{l0}\right]\right\}, \\ &= \sum_{l=-\infty}^{\infty}\left[J^{\Omega}_{l}\right] \end{aligned} \qquad \textbf{(4. 25)}$$

Inserting the equations that correspond to n_{l0} [Eq. 4.15)], E_{l0} [Eq. (4.16)], n_{l1} [Eq. (4.20)], and E_{l1} [Eq. (4.21)] into Eq. (4.25) the expression for the photo-EMF current component induced by the $l\,th$ spatial harmonic of the input light distribution can be obtained [7]:

$$J^{\Omega}_{l} = \frac{\Delta l^2}{2}\left(\frac{A_l}{A_0}\right)^2 \sigma_0 E_D \frac{\Omega\tau_{di}}{1 + i\Omega\tau_{scl}}, \qquad \textbf{(4. 26)}$$

It can be seen that the current amplitude J^{Ω}_{l} is proportional to modulation amplitude Δ, the square of the number of harmonic l, the square of input harmonic contrast A_l/A_0, the photoconductivity σ_0, and the electric diffusion field E_D.

4.2.7 Analysis of the dynamics of photo-EMF current in the presence of multiple spatial harmonics

It is clear from the Eq. (4.26) that the frequency transfer function of each spatial harmonic possesses a high pass filter shape observed for a sinusoidal input light distribution: i.e. the current amplitude grows linearly up to some cut-off frequency and keeps constant at higher frequencies.

However, as it was mentioned above (section 4.2.5) that the characteristic time of recording for each spatial harmonic depends on the product number of harmonic, spatial frequency and diffusion length (lKL_D): for $lKL_D << 1$ all spatial harmonics are recorded with the same speed and for $lKL_D >> 1$ the higher spatial harmonic is, the slower is its rate of recording.

The dynamic of the first, third and fifth component of photo-EMF current can be observed in figures 4.1(a) and 4.1(b). It can be seen that for a case of short diffusion length $lKL_D << 1$ the cut off frequency is independent on the number of harmonics [Fig. 4.1(a)], while for a case of long diffusion length $lKL_D >> 1$ the cut of frequency Ω_l of higher harmonics is shifted to the lower frequency region and it is proportional to the inverse square of the number of harmonic $\Omega_l \propto \left(1/l^2\right)$ [Fig. 4.1(b)].

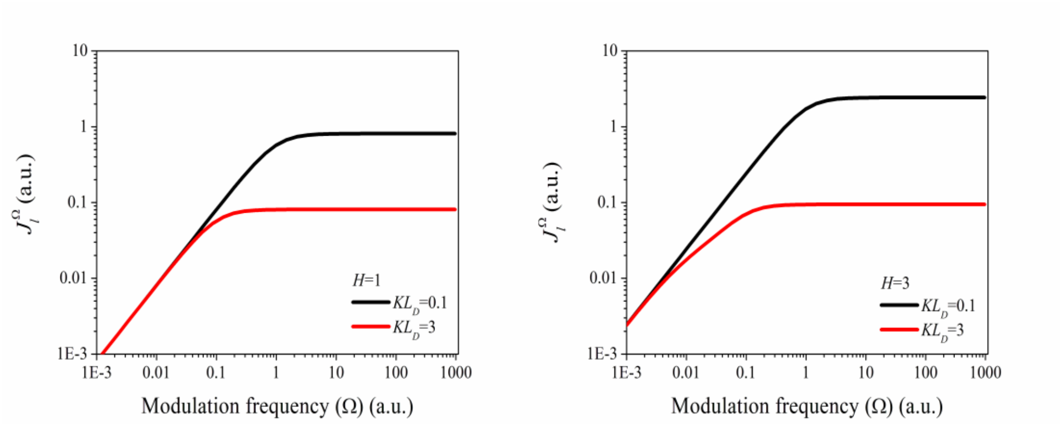

(a) $l = 1$ **(b)** $l = 1,3,5$

Fig. 4.1. Theoretical dependence of the photo-EMF current J_l^Ω amplitude versus modulation frequency Ω for different values of $KL_D = 0.1, 3$ and different harmonic number $H = 1, 3$.

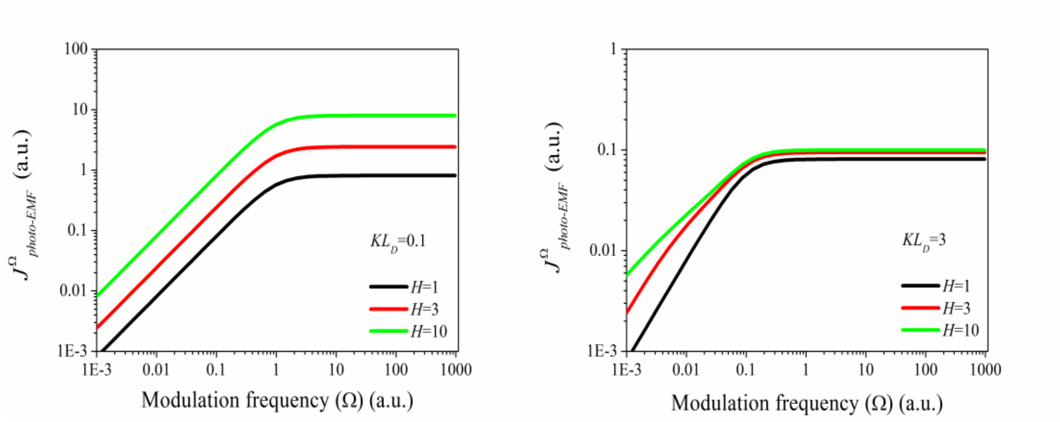

(a) $KL_D = 0.1$ **(b)** $KL_D = 3$

Fig. 4.2. Theoretical dependence of the total photo-EMF current $J^\Omega_{photo\text{-}EMF}$ amplitude versus modulation frequency Ω for different values of $KL_D = 0.1, 3$ and different harmonic number $H = 1, 3, 10$.

As to the total photo-EMF current amplitude, which is composed by the sum of the current component induced by corresponding harmonic of spatial distribution of light intensity, its dynamics for a different limiting cases is shown in Fig. 4.2.

Once again at the limiting case of short diffusion length $lKL_D << 1$ the characteristic cut off frequency is independent on the total number of harmonics being presented in the input intensity distribution and the frequency transfer function possess a classical high pass filter form [Fig. 4.2(a)]. For a case of long diffusion length $lKL_D >> 1$, however, even when the cut of frequency is independent on the harmonic content of the input signal, the different speed of recording for higher harmonics leads to the dispersion of the photo-EMF current at low modulation frequency $\Omega\tau_{scl} << 1$ and the dependence of the $J^{\Omega}_{photo-EMF}$ vs. Ω is not linear anymore [Fig. 4.2(b)].

Next, the obtained equation [Eq. (4.26)] $l\,th$ component of photo-EMF current amplitude is analyzed under the simplifying assumption of high modulation frequency $\Omega\tau_{scl} >> 1$:

$$J^{\Omega}_{l} = \frac{\Delta l^2}{2}\left(\frac{A_l}{A_0}\right)^2 \sigma_0 E_D \frac{1}{1 + l^2K^2L_D^2}, \qquad \textbf{(4. 27)}$$

It can be seen from the Eq. (4.27) that two limiting cases may be distinguished depending on relation between carriers' diffusion length L_D, spatial frequency K and harmonic number l:

a) Short diffusion length $(lKL_D << 1)$:

$$J^{\Omega}_{l} \approx \frac{\Delta l^2}{2}\left(\frac{A_l}{A_0}\right)^2 \sigma_0 E_D, \qquad \textbf{(4. 28)}$$

as a consequence total photo-EMF current:

$$J^{\Omega}_{photo-EMF} \approx \sum_{l=-\infty}^{\infty} J^{\Omega}_{l} = \frac{\Delta}{2}\sigma_0 E_D \sum_{l=-\infty}^{\infty} l^2\left(\frac{A_l}{A_0}\right)^2. \qquad \textbf{(4. 29)}$$

One can see [Eq. (4.29)], that the complex amplitude of photo-EMF total current density is proportional to the sum of the square of input harmonics contrasts times square of the number of harmonic l, for spatial harmonic whose period $\Lambda = 2\pi / Kl$ is shorter than inverse diffusion length. Therefore, in this regime, for higher spatial harmonics in the input illumination pattern the photo-EMF current response is amplified by factor l^2.

b) Large diffusion length $(lKL_D >> 1)$:

$$J_l^\Omega \approx \frac{\Delta l^2}{2}\left(\frac{A_l}{A_0}\right)^2 \sigma_0 E_D \frac{1}{l^2 K^2 L_D^2}, \qquad \textbf{(4. 30)}$$

as a result:

$$J_{photo-EMF}^\Omega \approx \sum_{l=-\infty}^{\infty} J_l^\Omega = \frac{\Delta}{2}\sigma_0\left(\frac{E_D}{K^2 L_D^2}\right)\sum_{l=-\infty}^{\infty}\left(\frac{A_l}{A_0}\right)^2. \qquad \textbf{(4. 31)}$$

One can observe [Eq. (4.31)], that for a limiting case of large diffusion length the signal (the complex amplitude of photo-EMF total current density) is proportional to the sum of squares of corresponding harmonics contrasts $V_l = (A_l / A_0)$.

Next the expression obtained above can be applied to the light distribution corresponding to the specific case of a binary grating with the complex amplitude of $l\,th$ harmonic $A_l = 2 / l\pi$.

a) Short diffusion length $(lKL_D << 1)$:

For the case of a binary grating with the period of fundamental harmonic Λ much bigger than the carriers' diffusion length L_D two factors (l^2 and A_l^2) cancel each other, as a result the relative contributions of different harmonics to $J_{photo-EMF}^\Omega$ are exactly the same, i.e.:

$$J_{photo-EMF}^\Omega \approx \sum_{l=-\infty}^{\infty} J_l^\Omega = \frac{\Delta}{2}\sigma_0 E_D \sum_{l=-\infty}^{\infty} l^2 \left(\frac{2}{l\pi}\right)^2 \left(\frac{1}{A_0}\right)^2. \qquad \textbf{(4. 32)}$$

One can see that the obtained solution in this case has no physical meaning because the infinite sum at $l \to \infty$ diverges $J_{photo-EMF} \to \infty$. However, one has to keep in mind that at $l \to \infty$ at least two conditions at which the above analysis has been performed are no longer valid. First of all at $l \to \infty$ the above inequality $lKL_D << 1$ does not hold. Second, the condition of small vibration amplitude $l\Delta << 1$ is violated and the linearization procedure described above cannot be applied. And finally, in real optical system the number of harmonic is always finite.

b) Large diffusion length $(lKL_D >> 1)$:

For a limiting case of large diffusion length:

$$J^{\Omega}_{photo-EMF} \approx \sum_{l=-\infty}^{\infty} J^{\Omega}_{l} = \frac{\Delta}{2}\sigma_0\left(\frac{E_D}{K^2L_D^2}\right)\sum_{l=-\infty}^{\infty}\left(\frac{A_l}{A_0}\right)^2 = \frac{\Delta}{2}\sigma_0\left(\frac{E_D}{K^2L_D^2}\right)\sum_{l=-\infty}^{\infty}\left(\frac{2}{l\pi}\right)^2\left(\frac{1}{A_0}\right)^2. \quad \textbf{(4. 33)}$$

The complex amplitude of photo-EMF total current density is proportional to the sum of squares of corresponding harmonics contrasts $V_l = (A_l/A_0)$. Note, that in this case the sum of squares of Fourier coefficients converges and its value can be easily calculated using Parseval’s theorem [8]. By this theorem the sum of squares of Fourier coefficients is equal to the integral (on an interval equal to the period) of the original function (intensity distribution):

$$\sum_{l=-\infty}^{\infty}\left|A_l\right|^2 = \frac{1}{2\pi}\int_{-\pi}^{\pi}\left|I(x)\right|^2 dx. \quad \textbf{(4. 34)}$$

For a case of binary grating with transmission amplitude 1, the above integral equals to $I_0^2/2$. Since zero order coefficient of Fourier series representing intensity distribution is $A_0 = I_0/2$, the total sum in Eq. (4.33) become unit. The physical meaning of this result is clear, if one reminds another possible formulation of Parseval’s theorem [8], namely that the normalized power of a periodic signal is equal to the sum of squares of the amplitudes of its harmonic components. Taking all this into account the expression for a total photo-EMF current becomes:

$$J^{\Omega}_{photo-EMF} \approx \frac{\Delta}{2}\sigma_0\frac{E_D}{K^2L_D^2}, \quad \textbf{(4. 35)}$$

and its value does not depend on the shape of the input intensity distribution.

Next the main dependencies of the photo-EMF current amplitude can be analyzed in details.

4.3 Graphs of the limiting cases

Graphs of the theoretical dependence of both limiting cases (depending on carriers' diffusion length) applied to a binary grating were performed in Perl and the results are shown in the next figures. The expression for $l\,th$ harmonic of the photo-EMF current amplitude J_l^{Ω} and the complex amplitude of photo-EMF total current density $J_{photo\text{-}EMF}^{\Omega}$ for the limiting cases were programmed. For the simplicity the following conditions have been assumed: $\Delta = 1$ and $\sigma_0 E_D = 1$.

In Fig. 4.3 the results of the dependence of photo-EMF total current versus number of harmonic l for different values of diffusion length L_D can be observed. Here $K = 1$ in all cases.

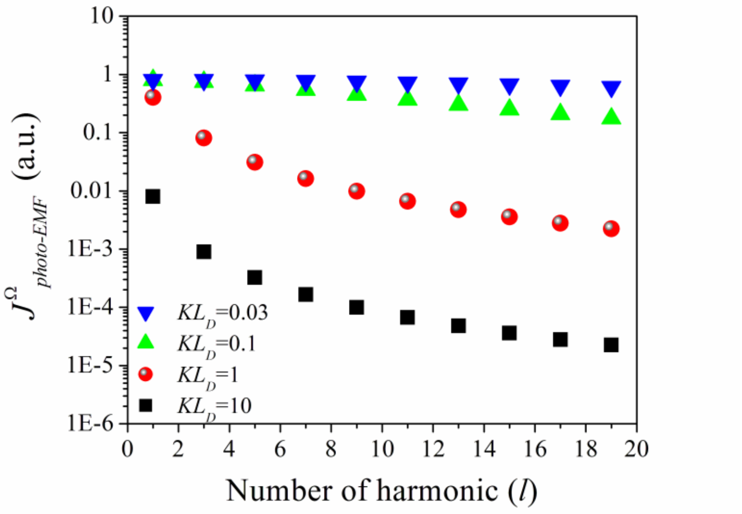

Fig. 4.3. Theoretical dependence of the photo-EMF total current $J_{photo\text{-}EMF}^{\Omega}$ versus number of harmonic l for different values of $KL_D = 0.03, 0.1, 1, 10$.

For a case of $KL_D = 0.03$ [see Fig. 4.3 where relation $lKL_D << 1$ holds] the response is constant (i.e. the intensity distribution varies as the grating) which illustrates that at this condition photo-EMF response depends on number of harmonic but not as strongly as the others.

At the increasing diffusion length the signal is constant at low harmonic and it decays as $1/l^2$ at higher harmonics. At large diffusion length $lKL_D >> 1$ the signal decays at the increasing the number of harmonic l.

The dependence of photo-EMF total current on spatial frequency K for different harmonic number $H = 1,2,3,10$ being presented in the input intensity distribution is shown in Fig. 4.4. Here $L_D = 1$, and K represent the spatial frequency of the fundamental harmonic.

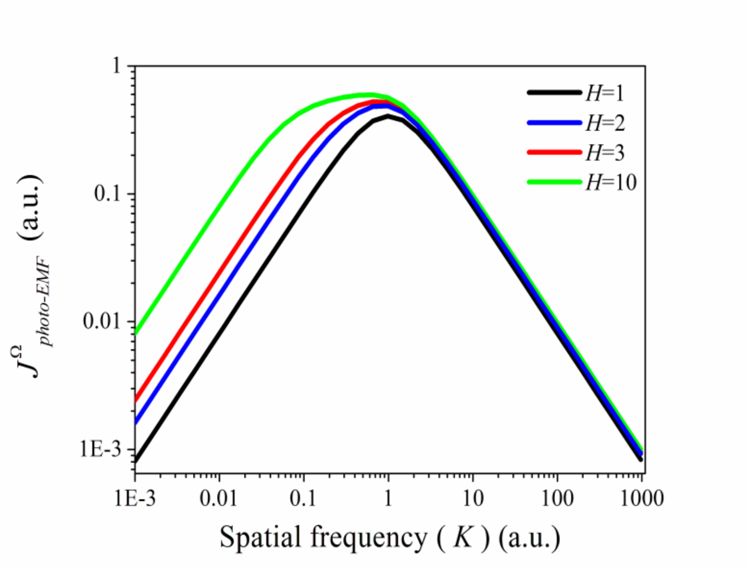

Fig. 4.4. Theoretical dependence of the photo-EMF total current versus spatial frequency K for different harmonic number $H = 1,2,3,10$ where $L_D = 1$.

One can observe that the $J_{photo-EMF}$ vs. K dependencies present some common features, namely: the signal first grows linearly at low spatial frequencies, when $K = L_D^{-1}$ the photo-EMF current reaches its maximum absolute and then it starts to decay as the inverse of the spatial frequency $1/K$.

All this features are well described by the standard theory of photo-EMF current [6]: the linear growth occurs due to the increasing diffusion field E_D, while the decay at high spatial frequencies is due to the diffusion-induced decay of contrast of the mobile carriers' grating. In difference from the conventional theory when the harmonic content of the input light illumination increases the maximum of the graphs in the vicinity of $lKL_D = 1$ flattens more and more. It means that increasing the harmonic number H, there is a region where the photo-EMF current does not depend on the period of the input grating.

It is important to note, that at in agreement with our theory, at low spatial frequency the amplitude of the photo-EMF current is bigger for a cases when more spatial harmonics are presented in the input illumination (Fig. 4.3), while for a high spatial frequencies all curves converges, independently on the harmonic content of the input intensity distribution.

4.4 Theoretical analysis of axial distribution of the photo-EMF current produced by light pattern generated by diffraction on binary grating on near field

In order to be able to analyze the axial distribution of the photo-EMF current produced by light pattern generated by diffraction on binary grating on near field the complex amplitude of the $l\,th$ harmonic A_l at a different z should be evaluated.

Using Eq. (2.45) the amplitude of $l\,th$ spatial harmonic of light intensity distribution can be written as:

$$A_l(z) = \exp\left(-\frac{i2\pi\, z\, l^2}{z_T}\right)\sum_{n=-\infty}^{\infty} a_{l+n}\, a_n^* \exp\left(-\frac{i2\pi\, z\, l\, 2n}{z_T}\right), \qquad \textbf{(4. 36)}$$

where $a_{n,l+n}$ are the Fourier coefficients of the transmission function of a binary grating [Eq. (2.45)]. For ideal binary grating the coefficients $a_{n,l+n}$ are non-zero only for odd values of sub index n and l: $l = 2s+1$, $n = 2t+1$, $s = t = 0,1,2,3\ldots$. Since the sum $l + n = 2(s+t+1)$ produce an even number, practically all coefficients of the sum in Eq. (4.36) are zero, except for two terms with $n = 0$ and $n = -l$. Thus Eq. (4.36) reduces to:

$$A_l(z) = \exp\left(-\frac{i2\pi\, z\, l^2}{z_T}\right)\left[a_l a_0^* + a_0 a_{-l}^* \exp\left(\frac{i2\pi\, z\, l\, 2n}{z_T}\right)\right]. \qquad \textbf{(4. 37)}$$

Since the Fourier coefficients are real, and they are even function of l, $a_l = a_{-l}^*$ Eq. (4.37) can be rewritten as:

$$
\begin{aligned}
A_l(z) &= \exp\left(-\frac{i2\pi z l^2}{z_T}\right) a_l a_0^* \left[1 + a_0 a_{-l}^* \exp\left(\frac{i2\pi z 2l^2}{z_T}\right)\right], \\
&= 2a_l a_0 \cos\left(\frac{2\pi z l^2}{z_T}\right).
\end{aligned}
\qquad \textbf{(4. 38)}
$$

Finally, the expression for $l\,th$ component of photo-EMF current amplitude [Eq. (4.26)] is:

$$
J_l^{\Omega}(z) = \frac{\Delta l^2}{2}\left[2a_l \cos\left(\frac{2\pi z l^2}{z_T}\right)\right]^2 \sigma_0 E_D \frac{1}{1 + l^2 K^2 L_D^2}, \qquad \textbf{(4. 39)}
$$

and the total current density [Eq. (4.25)] is given by:

$$
J_{photo-EMF}^{\Omega}(z) \approx \sum_{l=-\infty}^{\infty} J_l^{\Omega}(z) = \frac{\Delta l^2}{2} \sigma_0 E_D \frac{1}{1 + l^2 K^2 L_D^2} \sum_{l=-\infty}^{\infty} \left[2a_l \cos\left(\frac{2\pi z l^2}{z_T}\right)\right]^2. \qquad \textbf{(4. 40)}
$$

In the following, the axial dependencies of the photo-EMF current $J_{photo-EMF}(z)$ are discussed.

The evolution of the photo-EMF current amplitude as a function of the position along the optical axis z normalized to the Talbot distance z_T for a grating with only one spatial harmonic (sinusoidal distribution), for different $KL_D = 0.1, 1, 3$ is presented in Fig. 4.5.

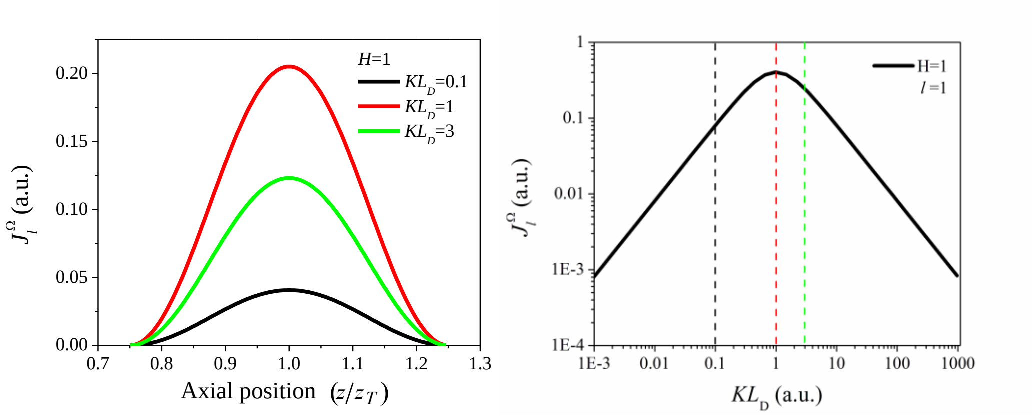

(a) **(b)**

Fig. 4.5. Theoretical dependence of the photo-EMF current amplitude (a) versus axial position z/z_T and (b) versus KL_D for $H = 1$ $(l = 1)$.

One can see that, when only one harmonic is present the signal varies sinusoidally and exhibits a maximum at z_T, where the Talbot self-image should be situated, and it is zero at $3z_T/4$ and $5z_T/4$ when minimal visibility is expected. The largest signal is observed at $lKL_D=1$ as it is expected from the standard photo-EMF theory.

When an additional harmonic is introduced to the input grating transmittance function ($1st$ and $3rd$ harmonics are now presented) the axial dependence of the photo-EMF current is changed in a way shown in Fig. 4.6. Again [Fig. 4.6(a)] the signal exhibits a maximum at z_T i.e. where the Talbot self-image should be situated, and it is almost zero at $3z_T/4$.

One can see that the presence of the $3rd$ spatial harmonic in the grating transmittance function leads to the appearance of nine peaks superposed to the fundamental sinusoidal distribution shown in Fig. 4.5. These peaks correspond to a nine secondary Talbot self-images, produced by a third harmonic of the input grating at distances: $z_T^{(3)}/2=(\Lambda/3)^2/\lambda$.

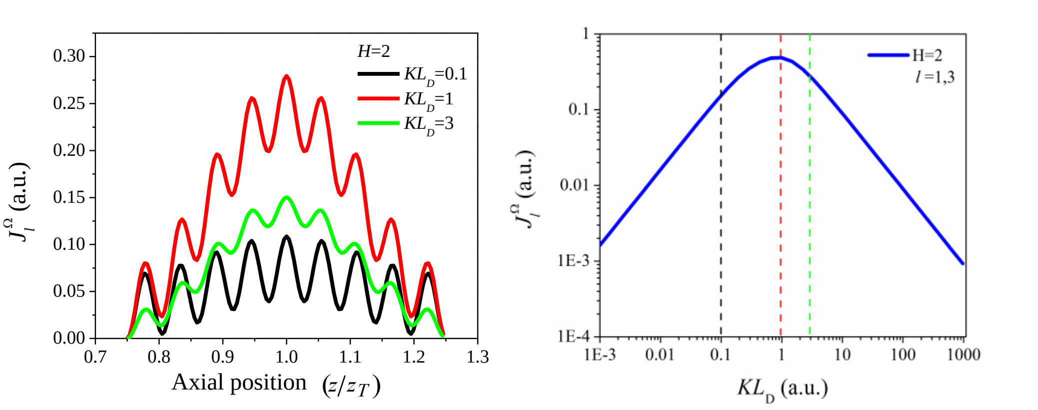

(a) **(b)**

Fig. 4.6. Theoretical dependence of the photo-EMF current amplitude (a) versus axial position z/z_T and (b) versus KL_D for $H=2$ $(l=1,3)$.

As in the previous case the signal amplitude is maximal at $lKL_D=1$. At small diffusion length $lKL_D<<1$ the shape of the signal is the same, though the overall amplitude is reduced in accordance with the theoretical predictions (Fig. 4.4 and Eq.

4.37). However at large diffusion length $lKL_D >> 1$ one can see that the relative contribution of $1st$ and $3rd$ harmonics is almost the same, again as it is expected from the theoretical analysis (Eq. 4.38 and Eq. 4.40).

Fig. 4.7(a) and Fig. 4.7(b) illustrate the axial dependence of the photo-EMF current in presence of three $(l = 1,3,5)$ and ten $(l = 1,3,5,\ldots 19)$ spatial harmonics in the transmittance function of the input grating.

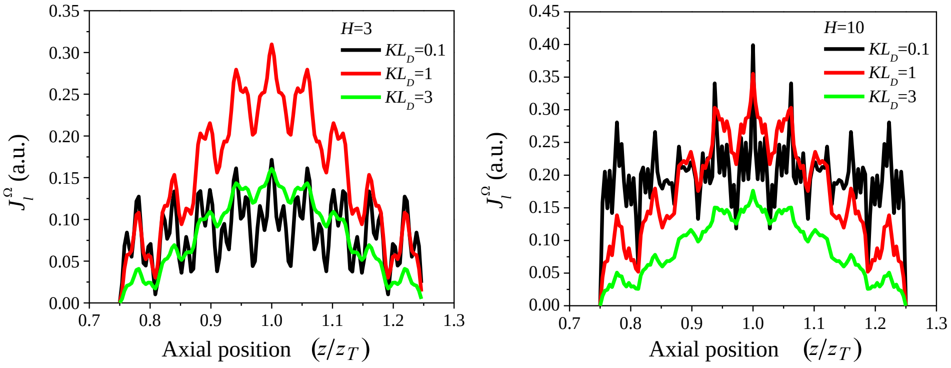

(a) **(b)**

Fig. 4.7. Theoretical dependence of the photo-EMF current amplitude versus axial position z/z_T for (a) $H = 3$ $(l = 1,3,5)$ and (b) $H = 10$ $(l = 1,3,5,\ldots 19)$.

The same features as in the previous cases can be observed, however, the side peaks are sharpened due to the presence of higher harmonics in input grating: there are 25 new Talbot planes $z_T^{(5)}/2 = (\Lambda/5)^2/\lambda$ [Fig. 4.7(a)].

Note that at small diffusion length $lKL_D << 1$ the axial dependence of photo-EMF current possesses sharp peaks and dips, but overall structure seems to be offset. The reason for this once more is that the relative contributions to the photo-EMF current amplitude J_l^Ω produced by different harmonics of the input grating are exactly the same (Eq. 4.37).

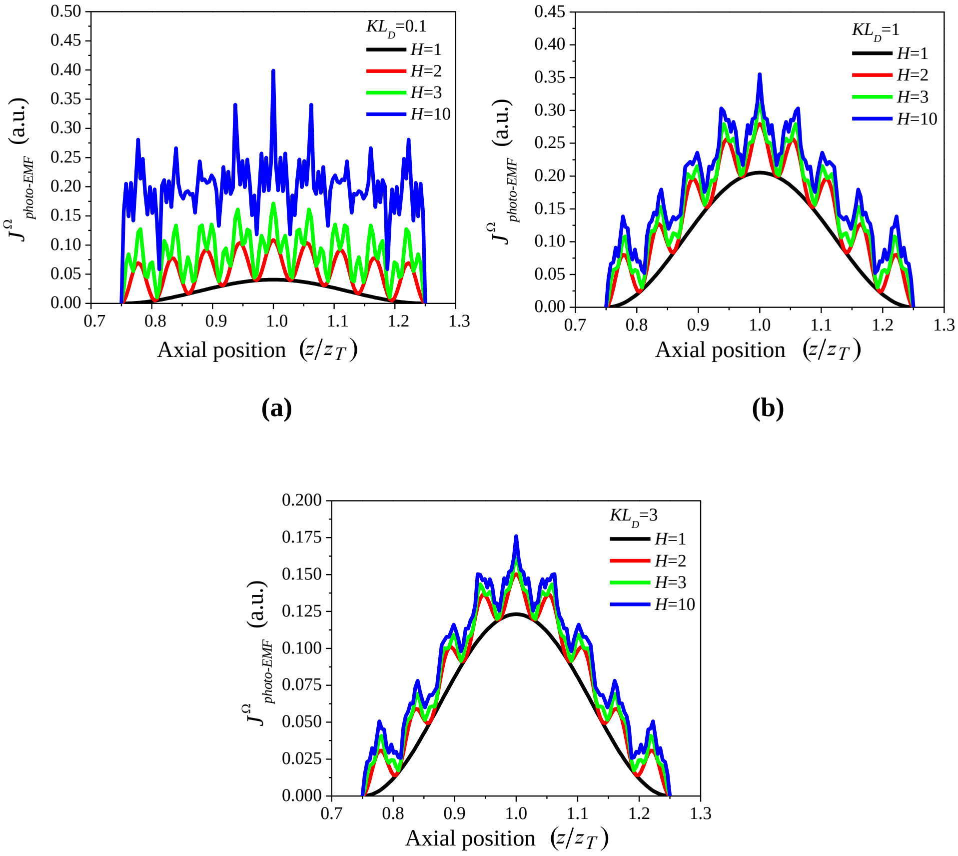

(a) **(b)**

(c)

Fig. 4.8. Theoretical dependence of the photo-EMF total current versus axial position z/z_T for different values of harmonic number $H = 1, 2, 3, 10$ where $KL_D = 0.1, 1, 3$.

Fig. 4.8 illustrates the dependence of the photo-EMF total current versus axial position z/z_T for different values of harmonic number $H = 1, 2, 3, 10$ in the input grating transmittance function and for different product of fundamental spatial frequency and carriers' diffusion length $KL_D = 0.1, 1, 3$. These figures are the compilation of all the results obtained from Fig. 4.5 to Fig. 4.7 and summarize the above results.

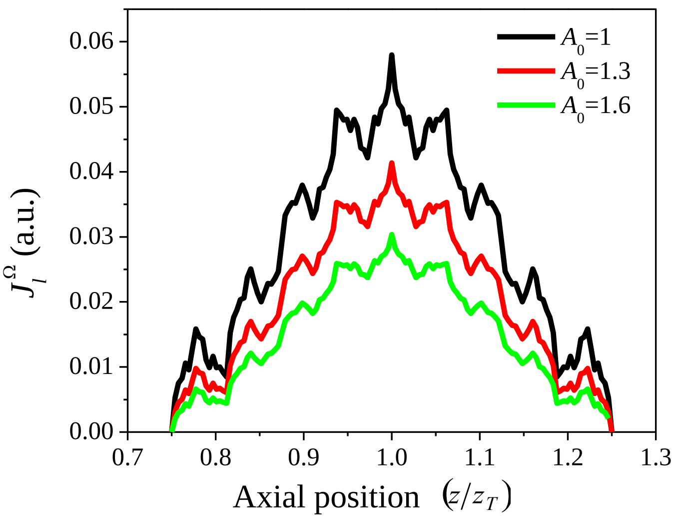

Fig. 4.9. Theoretical dependence of the photo-EMF current amplitude versus axial position z/z_T for different values of A_0 where $KL_D = 10$.

Fig. 4.9 shows the evolution of the photo-EMF current amplitude as a function of the position along the optical axis z for different values of coefficients A_0, which corresponds to different levels of average light intensity transmitted through the grating. Here the product of fundamental spatial frequency and carriers' diffusion length is $KL_D = 10$. As it is expected from the theoretical analysis the reduction of visibility leads to the decrease of the photo-EMF current amplitude: the signal decays proportionally to the inverse square of visibility.

Next, the results of detailed experimental investigation of non-steady-state photo-EMF effect induced by a 1-D periodical light pattern are presented.

4.5 Experimental results of axial distribution of the photo-EMF current produced by light pattern generated by diffraction on binary grating on near field

Here, the experimental results on investigation of photo-EMF effect induced by light patterns produced by Fresnel diffraction on Ronchi grating using *GaAs* detector at different experimental conditions are presented.

Illumination patterns created by diffraction in near field on binary grating are well suited for this purpose: they can be easily generated and modified, and in addition allows applying the results of this investigation to the practical case of detection of Talbot self-images for metrological application [9,10]. *GaAs* based detectors have been used for this investigation.

The choice of active material for the detector was motivated by its fast response (dielectric relaxation time in microsecond range at $633\,nm$ and $0.1\,W/cm^2$ average light intensity) and also by the fact that typical values of carriers' diffusion lengths (ten microns range) are comparable to the period of Ronchi grating used in our experiment, which allow us to check the most important theoretical results shown above.

As a first step the detectors used in our experiment have been characterized.

4.5.1 Experimental results of adaptive photo-detectors

Next the results of experimental investigation on detection of periodical patterns by photo-EMF detectors, using for this purpose Fresnel diffraction patterns of Ronchi grating are presented. The experiments were carried out with the experimental setup described in Fig. 3.10 in Chapter 3.

The experimental dependence of photo-EMF current using the crystal 2 as a detector versus axial position z is presented in Fig. 4.10.

One can observe that the signal is almost zero at $3z_T/4$ and $5z_T/4$ when minimal visibility is expected. In between there are 11 peaks. The amplitude of the peaks is almost constant, except for two peaks (number 4 and 8), whose amplitude is higher.

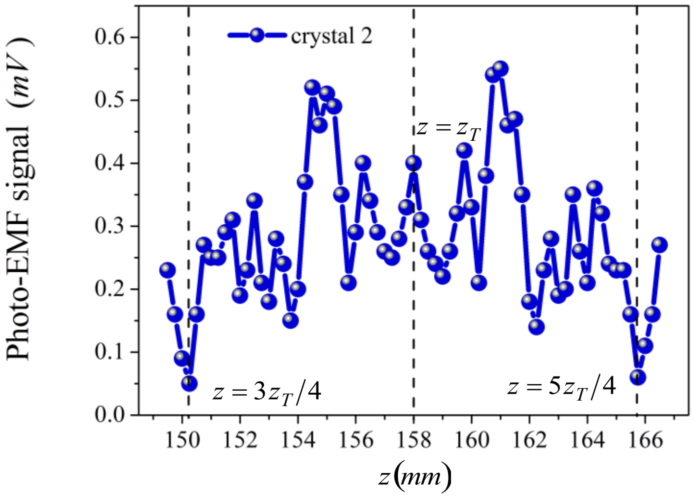

Fig. 4.10. Experimental dependence of the photo-EMF signal versus axial position z for crystal 2 with $L_D \approx 3\mu m$. Here the wavelength $\lambda \approx 633\,nm$, the output power of $\approx 11\,mW$, with a frequency of $600\,Hz$, with amplitude of $11\,Vpp$, and the binary grating with a period of $\Lambda = 100\,\mu m$.

Let us now to compare the obtained dependence with the predictions of our theoretical model. Remember that carriers' diffusion length L_D in this crystal was approximately $3\,\mu m$. For the Ronchi grating used in our experiment (fundamental period $\Lambda = 100\,\mu m$ and spatial period $KL_D = 0.25$) the condition $lKL_D << 1$ holds.

On the other side, the analysis of the numerical aperture of the optical system performed in Section 3.3 in Chapter 3 showed that at the distance where the axial scan has been performed ($z = 5z_T \approx 16\,cm$ from the grating) there are three diffraction orders, and as a consequence three spatial harmonics ($1st$, $3rd$ and $5th$) are involved in formation of periodical light pattern.

Our theory predicts that at these experimental conditions the expected axial dependence corresponds to that shown in Fig. 4.7(a). Indeed, the theory predicts that 25 peaks of almost comparable amplitude due to the condition $lKL_D << 1$, at which photo-EMF effect amplifies higher spatial harmonics, and as a result the relative contribution of all harmonics is almost the same. The disagreement with the theory can be observed in a number of peaks (11 observed vs. 25 expected) and large amplitudes of peaks 4 and 8. The number of peaks is less than expected because of not sufficient resolution of the scanning system.

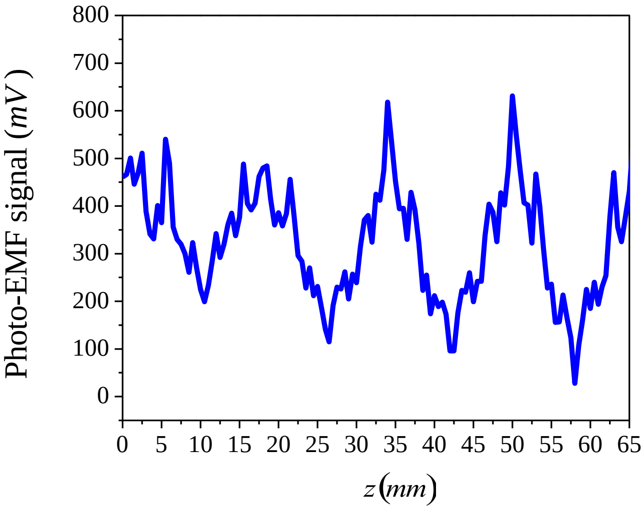

Fig. 4.11. Experimental dependence of photo-EMF signal versus axial position z. Here the wavelength $\lambda \approx 633\,nm$, the output power of $\approx 11\,mW$, with a frequency of $600\,Hz$, with amplitude of $11\,Vpp$, and the binary grating with a period of $\Lambda = 100\,\mu m$.

One can expect that when the detector is situated closer to the grating plane, the higher harmonics can participate on the formation of periodical pattern, which can lead to the formation of multiple peaks in $J_{photo\text{-}EMF}$ dependence. Axial scan of photo-EMF current at the distance equal to $2z_T$ was performed (Fig. 4.11) and indeed, noticed that the photo-EMF output current presented sharp variations along the scan which can be attributed to the superposition of multiple Talbot planes due to the presence of higher harmonics.

Fig. 4.12 shows the experimental dependence of photo-EMF in *GaAs* crystal 1. It can be observed that, besides the common feature of pronounced dips at the position z, which corresponds to the expected plains of minimal visibility ($3z_T/4$ and $5z_T/4$), the qualitative behavior of non-steady-state photo-EMF current as a function of axial position is rather different from that observed in crystal 2. Indeed, there are several peaks but their amplitude varies significantly, being the central peak the highest one.

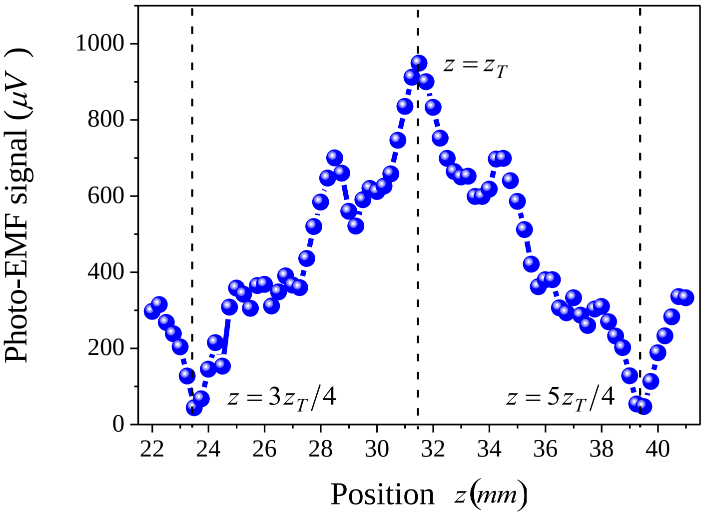

Fig. 4.12. Experimental dependence of photo-EMF signal versus axial position z in steps of $250\,\mu m$ for crystal 1 with $L_D \approx 40\,\mu m$. Here the wavelength $\lambda \approx 633\,nm$, the output power of $\approx 11\,mW$, with a frequency of $600\,Hz$, with amplitude of $11\,Vpp$, and the binary grating with a period of $\Lambda = 100\,\mu m$.

The explanation for this difference relays in the fact that crystal 1 possess much larger carriers' diffusion length (approximately $40\,\mu m$) than crystal 2. It means that for this crystal the opposite condition $lKL_D >> 1$ is valid, which, as it was shown by the above theoretical analysis, remarkably changes the axial dependence of the non-steady photo-EMF current.

Indeed, at this condition the signal is proportional to the sum of the squares of the harmonics contrasts, and as a result the axial dependence is the superposition of fundamental, third and fifth harmonic diffraction patterns $z_T^{(5)}/2 = (\Lambda/5)^2/\lambda$ [Fig. 4.7(a) and Eq. (4.33)]. This leads to the appearance of 25 peaks (produced by 25 secondary Talbot planes) offset by fundamental sinusoidal distribution with the period equal to the Talbot distance z_T. This behavior is quite similar to that observed experimentally, except for a number of peaks: there are five pronounced peaks, instead of 25 and another four can barely be distinguished on the experimental dependence (Fig. 4.12).

The same experiment was repeated in *GaAs* crystal 1, but with a grating with bigger spatial period $\Lambda = 508\,\mu m$, such as $KL_D \cong 0.5$ and the previous condition

$lKL_D >> 1$ is inverted. It can be observed (Fig. 4.13) that the axial dependence of the photo-EMF signal changes drastically: instead of the absolute maximum there are multiple peaks of comparable amplitude (the difference is within a factor of 2) in a way similar to that predicted by the theory. The remarkable feature, for which it is not feasible to provide a reasonable explanation, is that the central peak is almost absent, while two lateral are quite pronounced.

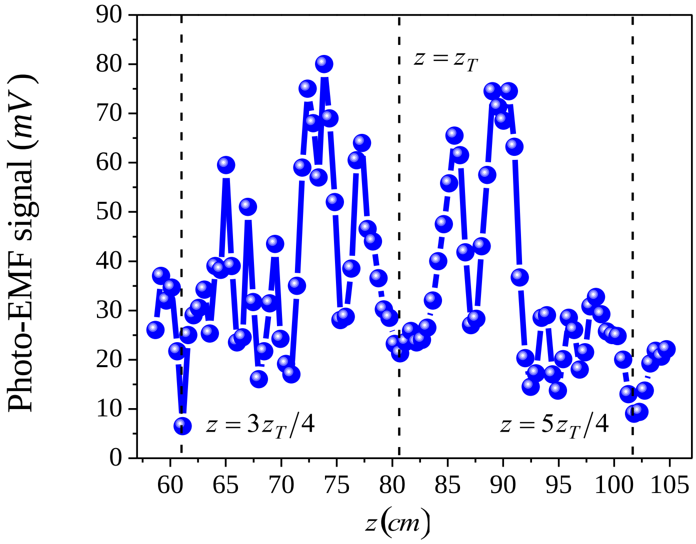

Fig. 4.13. Experimental dependence of photo-EMF signal versus axial position z for crystal 1 with $L_D \approx 40\,\mu m$. Here the wavelength $\lambda \approx 633\,nm$, the output power of $\approx 11\,mW$, with a frequency of $600\,Hz$, with amplitude of $11\,Vpp$, and the binary grating with a period of $\Lambda = 508\,\mu m$.

Fig. 4.14 shows experimental dependence of photo-EMF current at the condition $lKL >> 1$ in two different $GaAs$ crystals (like crystal 1), aiming to prove that theoretical results are valid independently on the crystal geometry and its photoconductive properties. The crystals possess different inter-electrode distance: $1\,mm$ and $2.5\,mm$.

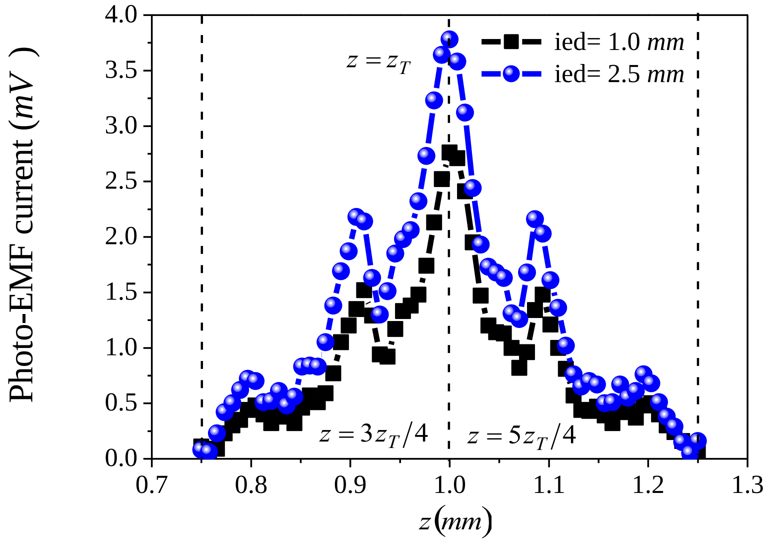

Fig. 4.14. Experimental dependence of the photo-EMF signal versus axial position z of two crystals with different inter-electrode distances: $1\,mm$ and $2.5\,mm$. Here the wavelength $\lambda \approx 633\,nm$, the output power of $\approx 11\,mW$, with a frequency of $600\,Hz$, with amplitude of $11\,Vpp$, and the binary grating with a period of $\Lambda = 100\,\mu m$.

One can see that photo-EMF dependence on z is qualitatively the same in both crystals, the only difference is the absolute value of signal amplitude: the signal is higher for the crystal with bigger inter-electrode spacing.

Summarizing, theoretical analysis of non-steady-state photo-EMF current induced by arbitrary 1-D periodical pattern have been performed using the model of monopolar photoconductor with a single impurity center. Analytical expression for complex amplitude of the photo-EMF current density has been derived in a general case of periodical light pattern containing only odd harmonics.

The analysis of this expression showed that for a case of small diffusion length $lKL_D << 1$ photo-EMF current is proportional to the sum of square of harmonics contrasts times square of the number of harmonic l, i.e. the higher harmonics are amplified. In the opposite case of large diffusion length $lKL_D >> 1$ the photo-EMF current is proportional to the sum of squares of harmonics contrasts.

As to the dynamics of the photo-EMF current, it was demonstrated that at $lKL_D << 1$ the characteristic time of space charge grating rebuilt is not sensitive to the harmonic content, while at $lKL_D >> 1$ this characteristic time is larger for a higher harmonics, leading to a sub-linear dependence of photo-EMF current at low frequency of modulation.

The results of this analysis have been applied to the specific case of axial dependence of the photo-EMF current induced by the illumination patterns produced by the diffraction of light on binary grating. Theoretical dependencies of photo-EMF current on axial position have been derived and analyzed in details.

Theoretically predicted axial dependencies of photo-EMF current have been observed at different experimental conditions using different *GaAs* detectors and main results of the theoretical analysis have been confirmed. It was shown that the observed axial dependence rely strongly on the relation between the fundamental spatial frequency K of Ronchi ruling and the transport properties of the semiconductor used for the detector, namely on its carriers' diffusion length L_D.

Depending on lKL_D product, two qualitatively different kinds of axial dependencies can be observed. At $lKL_D << 1$ the sequence of peaks of comparable amplitude produced by different Talbot planes appears on axial dependence of photo-EMF current. As a consequence the main Talbot plane, produced by the fundamental harmonic cannot be identified unambiguously. At $lKL_D >> 1$ the peaks produced by higher harmonic are offset by the large sinusoidal signal produced by the fundamental spatial frequency, hence the main Talbot plane can be detected directly from the position of absolute maximum.

Aiming the use of adaptive photo-EMF detectors for a purpose of Talbot interferometry it is feasible to realize that as a result of the above analysis, that the main criteria for a choice of detectors operation regime is that the condition $lKL_D << 1$ should be avoided. The condition $lKL_D \approx 1$ seems to be the best optimal one since in this case the condition for unambiguous identification of Talbot plane is still observed, while signal-to-noise ratio is maximized.

4.6 References

---

[1] J. W. Brown and R. V. Churchill, *Fourier series and boundary value problems*, Mc Graw Hill, 6th ed., N. Y., 2001.

[2] J. D. Gaskill, *Linear systems, Fourier transforms and Optics*, John Wiley & Sons, Inc., 1st ed., N. Y., 1978.

[3] S. Stepanov, *Photo-electromotive-force in semiconductors*, Handbook of Advanced Electronic and Photonic Materials and Devices, Vol. II, Academic Press, 2001.

[4] M. Abramowitz and I. A. Stegun, *Handbook of mathematical functions with formulas, graphs, and mathematical tables*, Dover publications, 9th ed., N. Y., 1972.

[5] J. W. Brown and R. V. Churchill, *Variable compleja y aplicaciones*, Mc Graw Hill, 7th ed., España, 2004.

[6] M. Petrov, I. Sokolov, S. Stepanov and G. Trofimov, "Non-steady-state photo-electromotive-force induced by dynamic gratings in partially compensated photoconductors", J. Appl. Phys. 68 (5), 2216-2225 (1990).

[7] **I. Guízar-Iturbide**, L. G. de la Fraga, P. Rodríguez-Montero and S. Mansurova, "Non-steady-state photo-EMF effect induced by an arbitrary 1-D periodical light distribution", SPIE, San Diego, California, EU. August 1-5 (2010). Proc. SPIE, Vol. 7790, 779011 (2010).

[8] H. P. Hsu, *Análisis de Fourier*, Prentice Hall, 1ra ed., México, 1998.

[9] G. S. Spagnolo, D. Ambrosini, and D. Paoletti, "Displacement measurement using the Talbot effect with a Ronchi grating", J. Opt. A: Pure Appl. Opt. 4, S376-S380 (2002).

[10] P. Singh P, M. S. Faridi, C. Shakher, and R. S. Sirohi, "Measurement of focal length with phase-shifting Talbot interferometry", Appl. Opt. 44, 1572-1576 (2005).

Chapter 5

Comparative analysis: photo-EMF versus CCD methods

5.1 Introduction

In this chapter the comparative analysis (numerical simulations and the experimental study) of three methods that are used for localization and analysis of the Talbot patterns generated by a Ronchi grating is performed.

The first method uses an adaptive photodetector based on the non-steady-state photo-electromotive force (photo-EMF), the second and third ones are conventional CCD-based methods (RMS and semivariogram techniques) for the localization and analysis of the Talbot patterns.

Numerical simulations of light patterns created in near field by the diffraction on binary grating object are performed in order to generate an input data for the three proposed methods. These data are processed using RMS and semivariogram algorithms and the photo-EMF equation.

The comparative experimental analysis of the technique based on photo-EMF effect against the CCD-based methods using RMS and semivariogram function is performed.

Finally, the possibility for localization of self-images in turbid media is also investigated, using a milk solution as a strongly-scattering media.

5.2 Theoretical comparison of axial dependence of contrast distribution evaluated by RMS, semivariogram, and photo-EMF effect

5.2.1 Numerical simulations of diffraction intensity distributions generated by binary grating

First, the input images for the comparative analysis of the three proposed methods are generated. Since the goal of this work is the Talbot self-images localization problem, the convenient source of images can be the numerical simulation of light patterns created by the diffraction of periodical object (binary grating) in near field.

For the numerical computation of diffraction intensity distributions generated by binary grating, the complex amplitude $U(x,z)$, and the image intensity distribution $I(x,z)$ of the Fresnel diffraction pattern [see Eq. (2.42) and Eq. (2.43) in Chapter 2] were programmed in Octave or Matlab and the results are shown in Fig. 5.1.

In Fig. 5.1, the intensity distributions created by diffraction on a binary grating which only contains 3 spatial harmonics $(l = 1,3,5)$ at different axial positions in units of Talbot distances z_T (between $z_T = 3z_T/4$ and $z = z_T$ in steps of $z_T/32$) are shown. Note that because of the symmetry of the effect, only a quarter part of Talbot period was scanned.

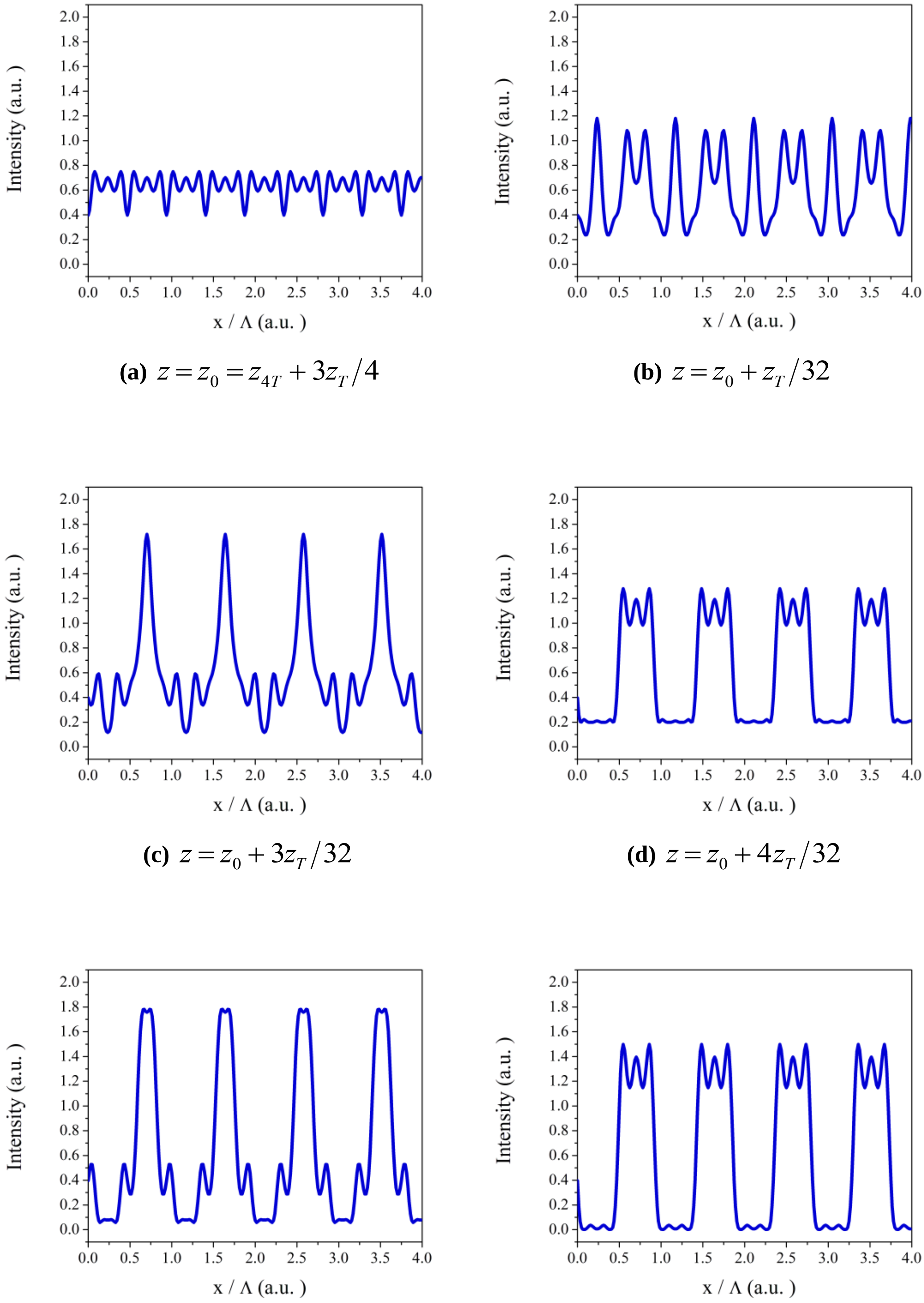

(a) $z = z_0 = z_{4T} + 3z_T/4$

(b) $z = z_0 + z_T/32$

(c) $z = z_0 + 3z_T/32$

(d) $z = z_0 + 4z_T/32$

(e) $z = z_0 + 6z_T/32$

(f) $z = z_0 + 8z_T/32 = 5z_T$

Fig. 5.1. Numerical simulations of intensity distributions generated by a binary grating which contains 3 harmonics at different positions of z-axis.

5.2.2 Axial dependence of contrast using the RMS and semivariogram methods

Using the above input data (intensity distributions), RMS and semivariogram of a given data array (I_i) at different z positions were calculated applying the RMS contrast equation and the semivariogram function [see Eq. (2.35) and Eq. (2.38) in Chapter 2] programmed in Matlab. The axial dependence of the contrast evaluated using these methods are shown in the next figures [1]:

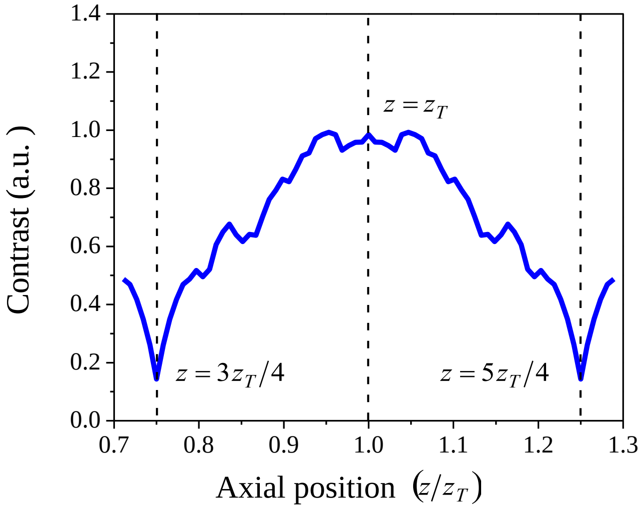

(a)

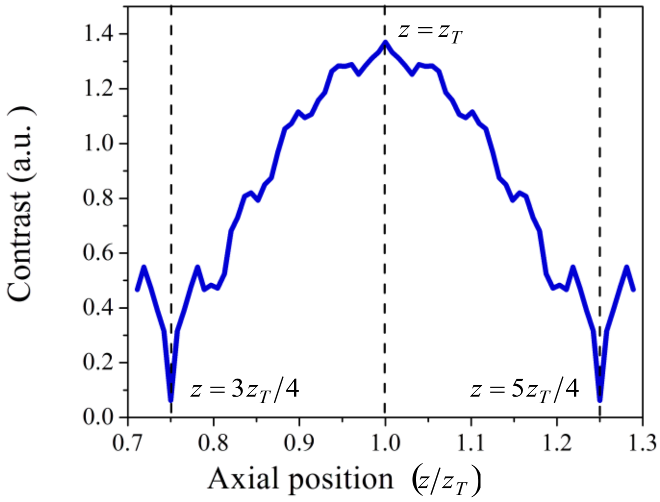

(b)

Fig. 5.2. Contrast dependence versus axial position using (a) RMS and (b) semivariogram function.

In Fig. 5.2, the planes where the Fresnel diffraction patterns have minimum visibility or contrast at $z = 3z_T/4$ and maximum contrast at $z = z_T$ and side peaks are identified.

In case of the numerical simulation with RMS method Fig. 5.2(a), the maximum position cannot be defined clearly, since there are two other side lobes with the same amplitudes, while in case of semivariogram-based method Fig. 5.2(b), there is an absolute maximum.

5.2.3 Axial dependence of contrast using the photo-EMF effect

The photo-EMF response for a given intensity distribution $I(x)$ was analytically calculated in previous Chapter, and here the axial dependence of photo-EMF signal generated by Eq. (4.33) (for the case of $KL_D \geq 1$) shown in Section 4.4 for comparison purposes is presented (see Fig. 5.3). Note that the array of data for statistical analysis is not created, as in previous cases, since analytical solution is known.

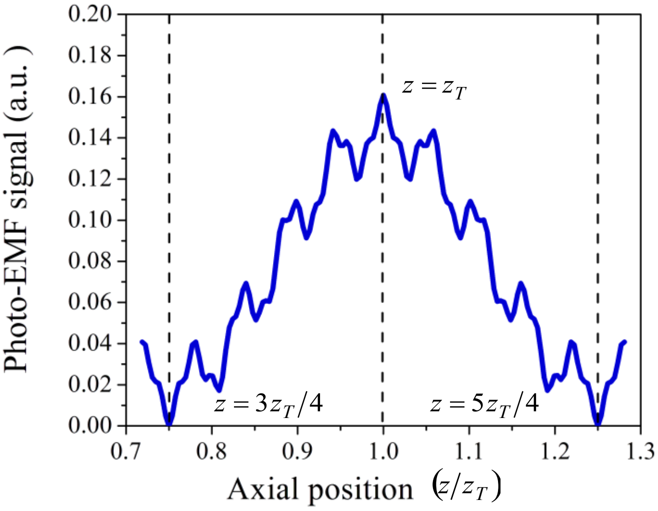

Fig. 5.3. Contrast dependence versus axial position using Eq. (4.33) for photo-EMF effect.

Fig. 5.3 presents resembles dependencies shown in Fig. 5.2. The signal is almost zero at $z = 3z_T/4$, i.e. when minimal visibility is expected. There is a maximum at $z = z_T$, i.e. where the Talbot self-images should be located, and nine side peaks are identified. These peaks correspond to a 25 secondary Talbot self images, produced by the fifth harmonic of the input grating at distances $z_T^{(5)}/2 = (\Lambda/5)^2/\lambda$ superimposed to the fundamental one $z_T/2 = \Lambda^2/\lambda$. One can observe only nine side peaks because of the resolution of the graph.

These side peaks are barely distinguished in RMS and semivariogram axial dependencies methods while they are very well pronounced in the theoretical curve generated by photo-EMF equation.

5.3 Experimental analysis of axial dependence of contrast distribution evaluated by RMS, semivariogram, and photo-EMF effect

5.3.1 Experimental intensity distributions generated by a binary grating

The input images used in the experimental analysis for the RMS and semivariogram methods were generated by recording the diffracted light pattern by CCD camera. The 2-D image was processed averaging the intensity on y direction to obtain the intensity patterns in one dimension (1-D).

The experimental set up is shown in Fig. 3.7 in Chapter 3. The examples of intensity distribution $I(x)$ averaged in y at different axial positions z are shown in Fig. 5.4.

It is important to notice that the distance z at which the CCD camera started the scanning corresponds to the position, $z_0 \approx z_{4T} + 3z_T/4$, where $z_{4T} \approx 126.4\ mm$ is the position of $4th$ Talbot plane.

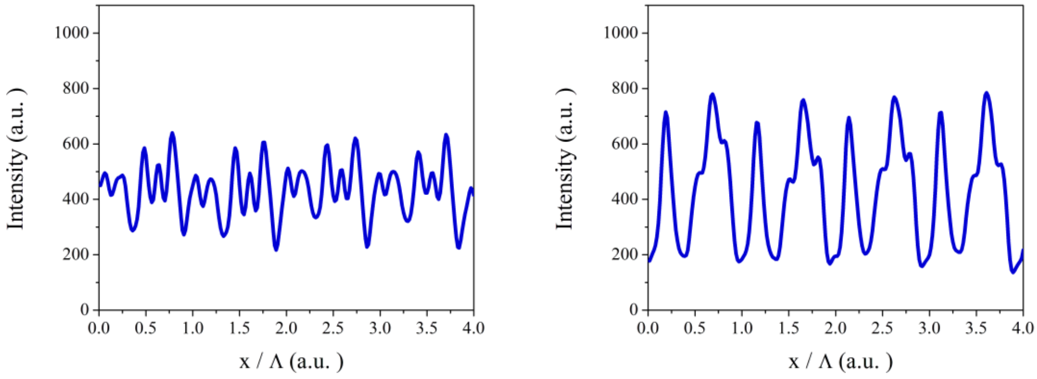

(a) $z = z_0 \approx 150\,mm$ **(b)** $z = z_0 + z_T/32 \approx 151\,mm$

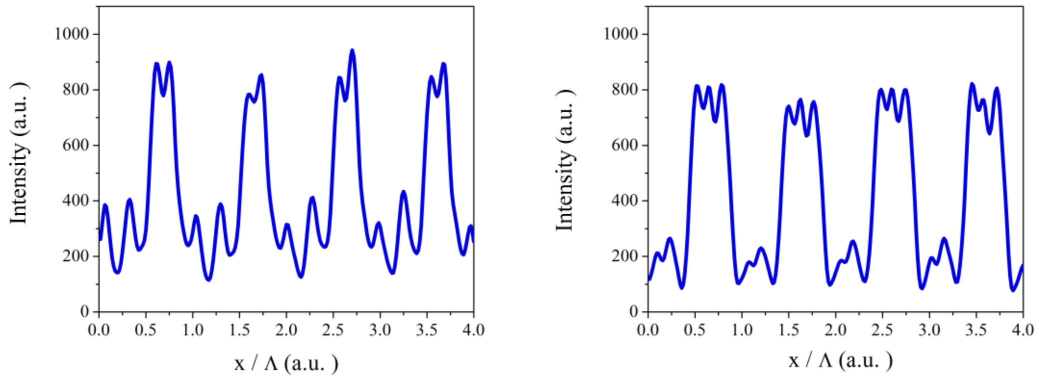

(c) $z = z_0 + 3z_T/32 \approx 153\,mm$ **(d)** $z = z_0 + 4z_T/32 \approx 154\,mm$

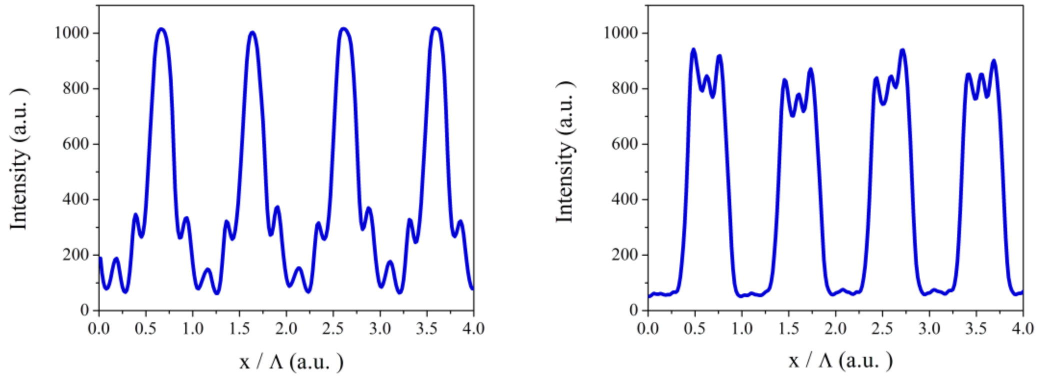

(e) $z = z_0 + 6z_T/32 \approx 156\,mm$ **(f)** $z = z_0 + 8z_T/32 = 5z_T \approx 158\,mm$

Fig. 5.4. Experimental 1-D intensity distributions generated by a binary grating recorded by CCD at different positions of z-axis.

Comparing Fig. 5.4 with Fig. 5.1, the same general characteristics are observed. At a distance equal to $z = 3z_T/4$ the intensity of the image of the grating, is practically uniform. At a distance equal to $z = z_T$ the intensity of the image of the grating corresponds to Talbot self-image. In between there are some complicated structures [Fig. 5.4(b)-5.4(e)] due to the superposition of different harmonics.

One can observed from the intensity distributions, that the system acts as low-pass spatial filter cutting all spatial harmonics higher than fifth. This can be explained by the fact that at the given axial position (distance from the grating to the detector) and the optics used only three first diffracted orders are collected by the system.

5.3.2 Experimental results in free space

5.3.2.1 RMS and semivariogram methods

Applying the experimental 1-D intensity distributions (see Fig. 5.4), RMS and semivariogram at different z positions were determined. In the case of RMS method, the RMS contrast equation was employed and for convenience the program Excel was used. On the other case, the semivariogram function was used, and it was programmed in Matlab. The results are shown in Fig. 5.5 [2].

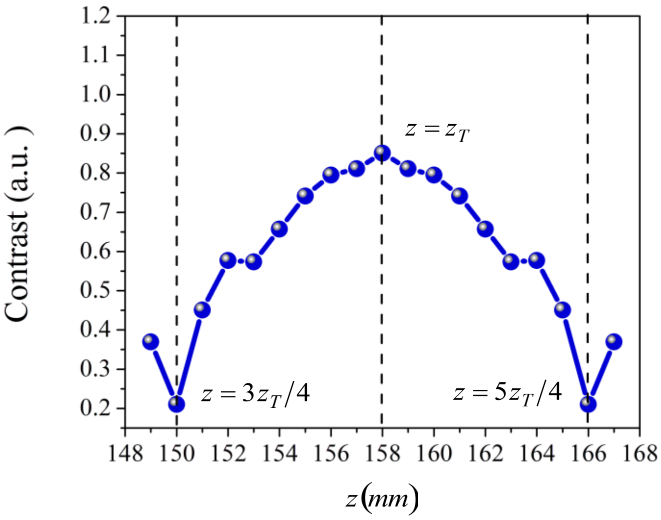

(a)

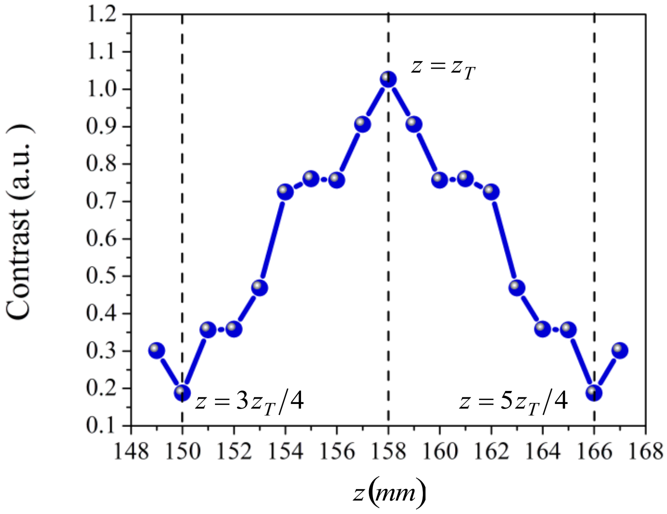

(b)

Fig. 5.5. Experimental dependence of contrast estimated by (a) RMS and (b) semivariogram using the data generated by CCD camera as a function of the axial position z. Here the wavelength $\lambda \approx 633\,nm$, the output power of $\approx 11\,mW$, and the binary grating with a period of $\Lambda = 100\,\mu m$.

The difference obtained experimentally between the position of planes of minimal and maximal contrast are in good agreement with the estimations of Talbot distance z_T for a grating with a $100\,\mu m$ period that is approximately $31.6\,mm$.

Comparing these experimental results with the contrast estimated by numerical simulations (see Fig. 5.2), one can recognize that at $z = 3z_T/4$ the Fresnel diffraction patterns have the lowest level of contrast and at $z = z_T$ the upper level of contrast. The maximum is clearly visible, with both techniques, but is more pronounces in the case of semivariogram.

The ratio between minimal (at $3z_T/4$) and maximal (at z_T) value of the contrast is approximately 4.2 for RMS and 5.5 for semivariogram. However, the axial dependence of contrast determined in our experiment also presents some secondary periodical structure (side peaks: 3 for RMS and 5 for semivariogram), though this structure is less pronounced than that predicted by the theory.

Comparing the experimental results obtained in Ref. [3] against our experimental results, there is a good agreement between them: the planes of minimal and maximal (where the Talbot self-image should be located) contrasts are well defined for RMS, and semivariogram methods. However, is clearly visible that the secondary peaks in the axial distribution are almost imperceptibles in Ref. [3]. It can be explained considering that in our experiment a better overlapping of the diffracted orders is achieved.

5.3.2.2 Photo-EMF

The experimental results obtained by axial scanning of the adaptive photodetector based on the photo-EMF effect instead of CCD camera, are presented in Fig. 5.6.

Here, the results are obtained directly the lock-in amplifier (the integration time of the lock-in amplifier was set at $1s$) and an image processing is not necessary. Note, however, that photo-EMF measurements does not provide the absolute value of the contrast (value between 0 and 1) in difference from the methods discussed above.

Fig. 5.6 shows the photo-EMF signal as a function of the axial position of the detector, scanning a range where the $5th$ Talbot self-image is located [Fig. 5.6 (a)] in steps of $50\mu m$ [Fig. 5.6 (b)], $250\mu m$ [Fig. 5.6 (c)], and $1mm$ [Fig. 5.6 (d)]. Again, the planes of maximal and minimal contrasts can be easily identified on this figure and their position coincides very well with the numerical estimations.

In Fig. 5.6, the sharp maximum is well defined, and the value of the ratio of the signal amplitude at the plane of maximal (at z_T) and minimal (at $3z_T/4$) contrast is approximately 12. The amplitude of the signal at the plane of minimum contrast is a result of two components: due to the vibrating speckle pattern, which cannot be avoided and electric noise of the detection system. In our experiment, the second component was the dominating one, and by proper grounding the signal-to-noise ratio as large as 50 can be obtained.

Note, that in addition to the main periodical structure defined by fundamental harmonic (main Talbot planes) with a period $z_T/2$ there are secondary periodical structure (5 peaks) that are related with higher harmonics of the input grating, as it was shown in previous Chapter. Note that similar to the case of RMS and semivariogram this secondary structure is less pronounced than the predicted by the theory.

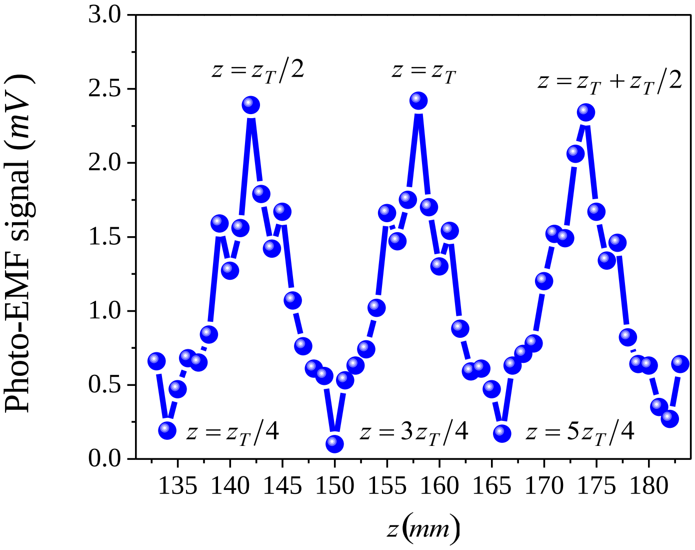

(a)

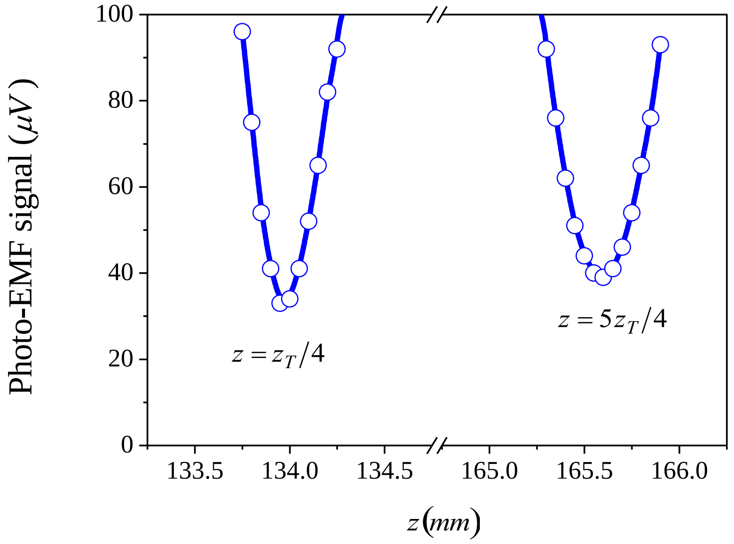

(b) steps of $50\,\mu m$

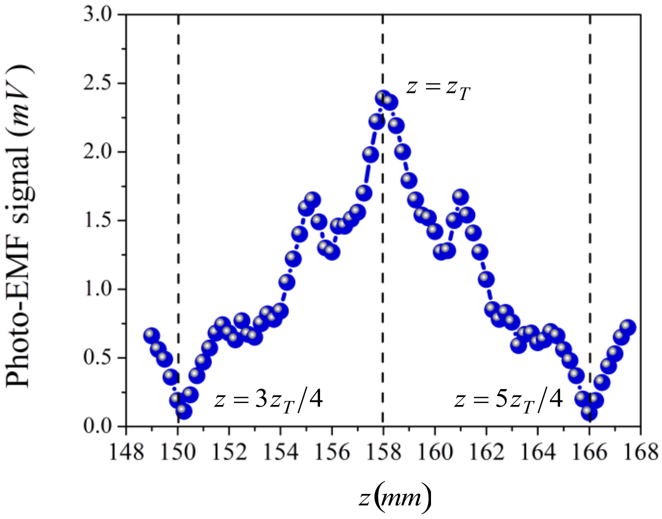

(c) steps of $250\,\mu m$

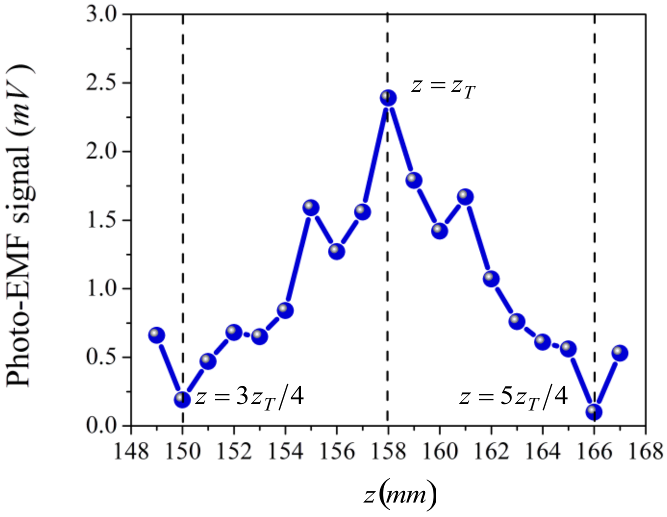

(d) steps of $1\,mm$

Fig. 5.6. Experimental dependence of photo-EMF signal as a function of the axial position of the detector. Here the wavelength $\lambda \approx 633\,nm$**, the output power of** $\approx 11\,mW$ **, with a frequency of** $600\,Hz$**, with amplitude of** $11\,Vpp$**, and the binary grating with a period of** $\Lambda = 100\,\mu m$**.**

5.3.2.3 Discussion

Considering the experimental results (Fig. 5.5 and Fig. 5.6), one can verified that the three methods are suitable for effective localization of Talbot self-images, since the planes of minimal and maximal visibility can be identified. Next, the comparative analysis of advantages and limiting factors of these techniques is performed.

First of all, CCD based techniques needs image recording and posterior signal processing, so its response time is limited by the CCD acquisition time and the velocity of the signal processing which can be as fast as video rate, as stated in Ref. [3]. In its turn, the response time of the photo-EMF based photodetector is limited by the dielectric relaxation time of the crystal which can be as short as few nanoseconds in semiconductor illuminated by light with the wavelength at which band-to-band absorption occurs.

It can be an important advantage in applications which require fast response time, for instance for measurements of vibrations or axial displacements, as is described in following Chapter 6.

Next, the sensitivity of the techniques to the changes of contrast is discussed. The ratio of the maximum and minimum signal obtained by the photo-EMF technique is larger than that observed in CCD-based experiments, even when in CCD-based experiments a bandpass filter at the wavelength of the *He-Ne* laser was used, while the photo-EMF experiment was performed with environment lighting on.

We believe that the possible explanation can be drawn if one takes into account the photo-EMF signal is proportional to the square of the contrast, while the CCD-based techniques are linearly dependent on the contrast. Also, note that the maximum of the photo-EMF signal is determined by the square of the contrast of the fundamental harmonic, and this contrast is larger than unit (≈ 1.2). The minimum signal (if one controls the electrical noise) is proportional to the square of the background illumination contrast. This latter is speckle-like and it is produced by the grating imperfections and random fluctuations in its transmission and it is always much less than unit. So, the ratio of maximal to minimal signal will always be larger for the case of photo-EMF since its output is the square of this ratio.

It means that photo-EMF technique is more sensitive to the small variations of contrast compared to CCD-based techniques. The resolution (i.e. the minimal changes in contrast which can be detected by the system) of photo-EMF based detectors will be discussed in next chapter. It worth to note that CCD based techniques, in exchange to relatively low sensitivity to the contrast variations, can work efficiently at very low illumination levels (few μW), while photo-EMF based detectors needs higher intensities (one order of magnitude larger, at least).

Finally, the experimental data against theoretical predictions are compared. In general terms (related with the propagation of fundamental spatial harmonic) there is a good agreement between them: the planes of minimal and maximal contrasts are well defined. However the “fine structure”, i.e. secondary peaks in the axial distribution of contrast obtained experimentally is less pronounced than that predicted by theory (this is especially noticeable in case of CCD-based techniques). We believe, that it can be explained considering that in theory a perfect overlapping of the diffracted orders is assumed, while experimentally there is a small shift between them.

5.3.3 Experimental results in turbid media

Light propagation through of a strongly-scattering media is a field that has been studied (analytically and numerically) for many authors [4], because of the need for the development of biomedical imaging techniques [5]. The research in this area had given promising results in optical coherence tomography [6], and in diffusing wave spectroscopy [7]. In many of these cases is necessary to analyze the contrast of the images and its relation with the turbidity of the media.

The interest of this work is to analyze the problem of self-images localization in presence of strong scattering using photo-EMF based method.

The experimental evolution of the contrast as a function of the position along the optical axis z, scanning a range where the $5th$ Talbot self-image is located in steps of $1mm$, for different concentrations of semi-skimmed milk diluted in deionized water (expressed as volume ratio) contained in a glass cell, is presented in Fig. 5.7. Again, the results are obtained directly the lock-in amplifier, and an image processing is not necessary.

One can notice that the photo-EMF technique (Fig. 5.7) is still able to identify the planes of maximal $(z = z_T)$ and minimal contrast $(z = 3z_T/4)$ of the Fresnel diffraction patterns even at the condition of strong contrast degradation.

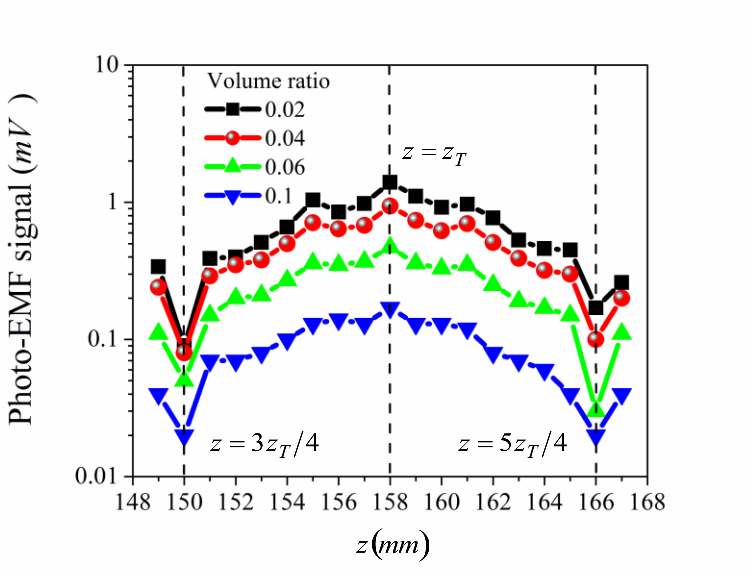

Fig. 5.7. Experimental dependence of photo-EMF signal as a function of the axial position of the detector in turbid media. Here the wavelength $\lambda \approx 633 nm$, the output power of $\approx 11 mW$, with a frequency of $600 Hz$ and with amplitude of $11 Vpp$, and the binary grating with a period of $\Lambda = 100 \mu m$.

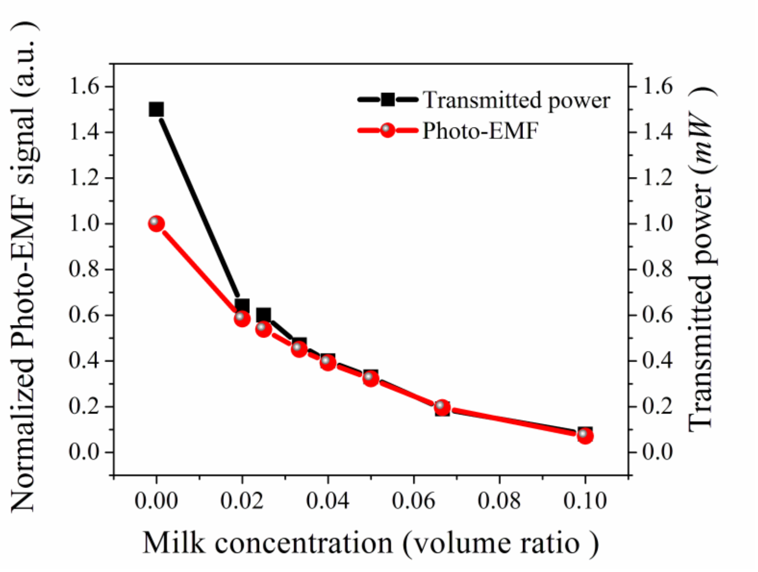

Fig. 5.8. Behavior of the maximum obtained by photo-EMF signal and the transmitted power versus milk concentration on the solution.

The increase of the turbidity of the media leads mainly to the decrease average light intensity arriving to the detector, as well as to the contrast degradation.

Both of these factors, intensity and contrast, affect the photo-EMF response at Talbot plane. The amplitude of the photo-EMF signal (Fig. 5.8) decays exponentially with the increasing milk concentration, at the same rate as it does the average light intensity (I_0) transmitted through the turbid media (Fig. 5.8), which is in agreement with the theoretical predictions [see Ref. [8] or Eq. (2.43) in Chapter 2] $\left(J^{\Omega} \propto \sigma_0 \propto I_0\right)$, and with the experimental dependence shown in Fig. 3.12 in Chapter 3.

At our experimental conditions cannot be separated the contribution of the intensity and contrast to the decay of the maximal signal.

The contrast degradation is evident mainly in the less pronounced fine structure of the axial distribution with the increased turbidity since the spatial coherence loss affects mainly higher spatial harmonics.

Theoretical analysis of Talbot images under illumination of the partially coherent light was reported by Yoshimura *et al*. [9], and they found that the contrast of Talbot images is dependent on spatial coherence length. Furthermore, theoretical degradation of coherence by turbulence was estimated based on the measurement of spatial coherence by Ho [10] and Andrews *et al.* [11]. Experimentally this was verified by Okoyama *et al*. [12]. Finally the theoretical behavior of intensity distribution on self-images systems into turbulent media were reported by Pérez *et al*. [13], and they described that the degradation on image formation is influenced by turbulence.

We believe that photo-EMF detectors can be potentially used to address and quantify the problem of contrast degradation due to the coherence loss in the scattering media, analyzing its fine structure and measuring the decay of higher spatial harmonics. This problem requires, however, more detailed theoretical and experimental investigation.

Summarizing, the experimental results confirmed that the three methods (photo-EMF effect, RMS, and semivariogram) are suitable for effective localization of Talbot self-images. The photo-EMF based detector potentially has shorter response time since it does no need image processing. In addition, they possess higher sensitivity to the contrast variations, but it needs higher light intensity, while CCD can work efficiently at very low illumination levels (few μW). Finally, the photo-EMF detectors can be potentially used for analyzing the spectral content of periodical objects since the fine structure of axial distribution of contrast is better defined comparing with that of CCD-based methods.

5.4 References

---

[1] **I. Guízar-Iturbide**, L. G. de la Fraga, P. Rodríguez-Montero and S. Mansurova, “Problem of Talbot self-images localization: adaptive photo-EMF based detector vs. CCD-based methods”, Photonics North, Niagara Falls, Ontario, Canada. June 1-3 (2010). Proc. SPIE, Vol. 7750, 77500Y (2010).

[2] **I. Guízar-Iturbide**, L. G. de la Fraga, P. Rodríguez-Montero and S. Mansurova, “Adaptive photodetector versus conventional method for localization of the Talbot

self-images", SPIE, San Diego, California, EU. August 1-5 (2010). Proc. SPIE, Vol. 7790, 779018 (2010).

[3] J L. M. Sanchez-Brea, F.J. Torcal-Milla, and E. Bernabeu, "Variogram-based method for contrast measurement," Appl. Opt. 47 (22), 5027–5033 (2007).

[4] A. Ishimaru, *Wave propagation and Scattering in Random Media,* IEEE Press, Piscataway, N.J. (1997).

[5] S. K. Gayen and R. R. Alfano, "Biomedical imaging techniques", Opt. Photon. News 7, 17-22 (1996).

[6] I. Kholodnykh, I. Y. Petrova, K. V. Larin, M. Motamedi, and R. O. Esenaliev, "Precision of Measurement of Tissue Optical Properties with Optical Coherence Tomography", Appl. Opt. 42, 3027-3037 (2003).

[7] D. J. Pine, D. A. Weitz, P. M. Chaikin, and E. Helbolzheimer, "Diffusing-wave spectroscopy", Phys. Rev. Lett. 60, 1134-1137 (1988).

[8] S. Stepanov, *Photo-electromotive-force in semiconductors,* Handbook of Advanced Electronic and Photonics Materials and Devices, Vol. II, Academic Press, 2001.

[9] H. Yoshimura, N. Takai, and T. Asakura, "Effects of amplitude and phase fluctuations of the Ronchi grating on Talbot images under illumination of the partially coherent light", J. Modern Opt. 40 (5), 825-839 (1993).

[10] T. L. Ho, "Coherence degradation of gaussian beams in turbulent", J. Opt. Soc. Am. 60 (5), 667-673 (1970).

[11] L. C. Andrews, W. B. Miller and J. C. Ricklin, "Spatial coherence of a gaussian-beam wave in weak and strong optical turbulence", J. Opt. Soc. Am. A 11 (5), 1653-1660 (1994).

[12] H. Okayama and L. Z. Wang, "Measurement of the spatial coherence of light influenced by turbulence", Appl. Opt. 38 (12), 2342-2345 (1999).

[13] D. G. Pérez and M. Garavaglia, "Intensity distribution behavior of self-image systems into turbulent media", J. Opt. Soc. Am. A 16 (4), 916-918 (1999).

Chapter 6

Displacement measurement using the adaptive photodetectors and the Talbot effect

6.1 Introduction

Measurements of distances, displacement or axial shifts are very important tasks in different technological applications and there are many well established optical techniques to measure it, which can be grouped as: time of flight techniques [1,2], geometrical or triangulation techniques [3,4], and phase or interferometric techniques [5,6].

Talbot effect [7] has been proposed in several and different metrological applications [8,9,10] including the measurement of displacements or axial shifts of a target [11]. Unlike the previous techniques, here the phenomenon exploited is the diffraction and the measured variable is the contrast of the light pattern.

Fig. 6.1 shows a typical setup to measure distance:

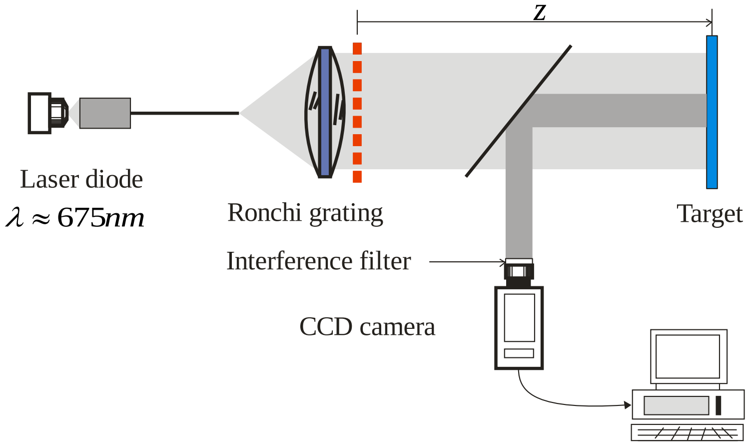

Fig. 6.1. Typical setup to measure distance (image from reference 11).

The experiments were performed with a laser diode with a wavelength $\lambda \approx 675\,nm$ and an output power of $15\,mW$, and a Ronchi grating with a period of $\Lambda = 0.254\,mm$.

In the proposed technique by Spagnolo et al. [11] the procedure to measure the distance z from the grating to the target is the following: the light pattern diffracted from a Ronchi grating is projected to a target and a CCD camera is focused to this target. The grating is mounted in a translation stage and the target is located at different distances from the grating. The image is recorded, and then an image processing with the fast Fourier transform (FFT)-based algorithm is performed. Finally, a band-pass filtering of this signal to decode the distance is realized.

Here in this chapter a novel technique based on the adaptive photodetectors and the Talbot effect to measure distance or the axial shifts of a mirror-like target is proposed.

6.2 Displacement measurement by adaptive photodetector and Talbot effect

First is needed to consider the effect of the aperture of the diaphragm on our system used to localize the Talbot or self-images planes (see Fig. 3.9 in Chapter 3).

The next figure (Fig. 6.2) shows the photo-EMF signal as a function on the aperture of the diaphragm, scanning a range where the $5th$ Talbot self-image is located in steps of $1\,mm$.

One can observe that as the aperture is reduced (from $12.7\,mm$ to $5.8\,mm$) the details (side peaks) of the signal are lost and that the signal becomes “softer”. In fact as the aperture is reduced less orders of diffraction passes through the aperture; when only the $+1$ and -1 (besides the order cero) passes through the diaphragm, the image of the grating becomes a sinusoidal grating in the Talbot plane [11,12].

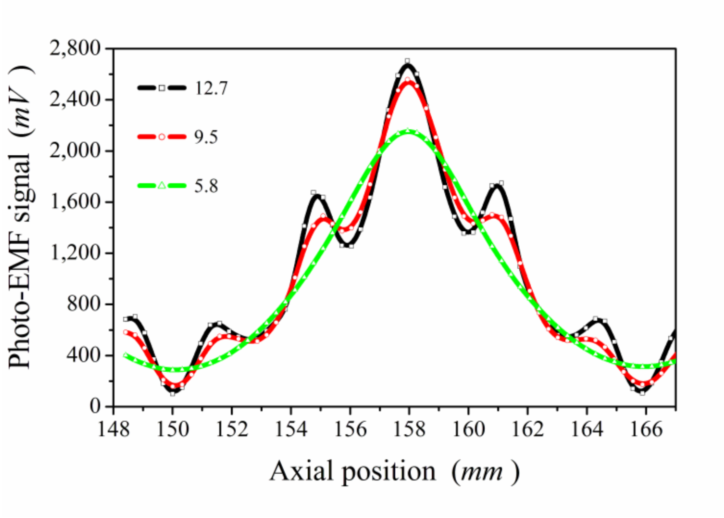

Fig. 6.2. The amplitude of photo-EMF signal as a function of the aperture of the diaphragm. Here the wavelength $\lambda \approx 633\,nm$, the output power of $\approx 11\,mW$, with a frequency of $600\,Hz$, with amplitude of $11\,Vpp$, and the binary grating with a period of $\Lambda = 100\,\mu m$.

For a sinusoidal grating it can be shown that the axial visibility [13] is given by:

$$V(z) = V_0 + V_S \cos\left(\frac{2\pi z}{z_T/2}\right), \tag{6.1}$$

where V_0 is the average visibility, V_S is the amplitude of the visibility, and the Talbot distance is $z_T = 2\Lambda^2/\lambda$.

Therefore is expected that the photo-EMF signal would be given by:

$$J^{\Omega}(z) \propto [V(z)]^2. \tag{6.2}$$

This property has to be used to implement a system to measure distances or axial displacements of a mirror. The experimental arrangement is shown in Fig. 6.3.

The experiments were basically performed with a *He-Ne* laser linearly polarized with a wavelength $\lambda \approx 633\,nm$ and an output power of approximately $11\,mW$. Using a $10\,x$ microscope objective the beam from the laser was expanded and pinhole with a diameter equal to $10\,\mu m$ was used to filter out the light. The diverging beam was incident on the collimating lens of focal length $20\,cm$. This collimated beam illuminated the binary grating.

After illumination with a collimated beam, the diffracted light from the grating (with a period $\Lambda = 100\ \mu m$) is sent to a mirror by a beam splitter. The adaptive photodetector is illuminated by the light reflected from the mirror, which was mounted in a translational stage. The aperture of the diaphragm was adjusted to produce a photo-EMF signal proportional to square of a sinusoidal function (as a function of the axial distance).

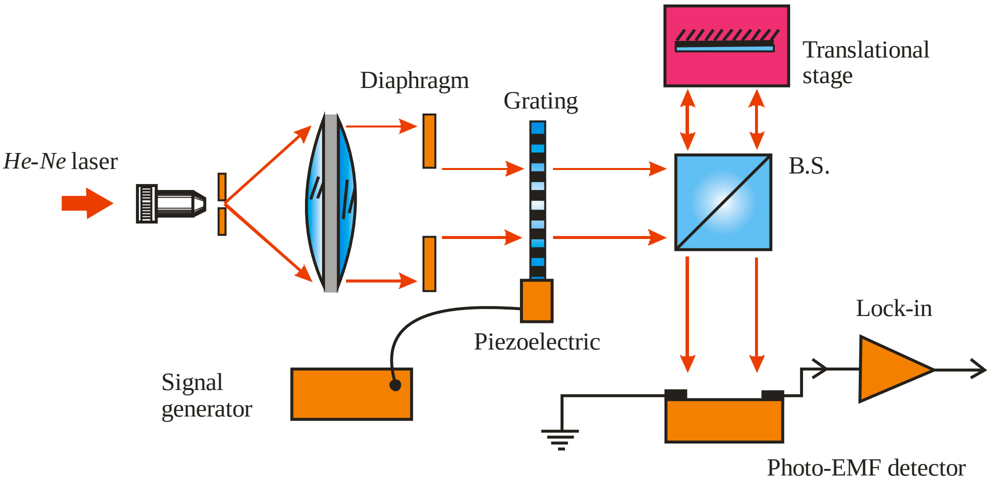

Fig. 6.3. Experimental setup to measure distances or axial displacements of a mirror. Here BS is the beam splitter.

For the geometry of the setup: 3 Talbot distances $(3z_T)$ from the grating to the beam splitter, 3 Talbot distances $(3z_T)$ from the beam splitter to the mirror, and 2 Talbot distances $(2z_T)$ from the beam splitter to the adaptive photodetector are used.

The next figure shows the experimental dependence of the photo-EMF signal as a function of the axial displacement of the mirror. In this case, the value of the aperture of the diaphragm is $5.8\ mm$.

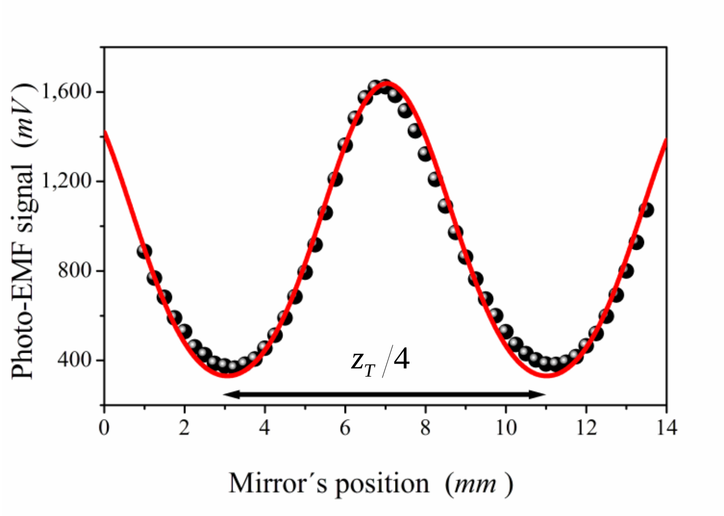

Fig. 6.4. The amplitude of photo-EMF signal as a function of the mirror's position. Here the wavelength $\lambda \approx 633\,nm$, the output power of $\approx 11\,mW$, with a frequency of $600\,Hz$, with amplitude of $11\,Vpp$, and the binary grating with a period of $\Lambda = 100\,\mu m$.

In Fig. 6.4 the circles are the experimental points and the solid line is the theoretical fit. In this plot one can observe that the photo-EMF signal corresponds very well to the theoretical estimate:

$$J(z) = \left[J_0 + J_S \cos\left(\frac{2\pi z}{z_T/4} \right) \right]^2 . \tag{6.3}$$

Note also that the signal has a periodical dependence with the period $z_T/4 \approx 8\,mm$. This property can be useful to calibrate the displacements.

The maximum of the signal corresponds to the position of the mirror where the $6\,th$ self-image is located, and the minimum in the signal corresponds to the plane of minimum visibility.

Between these points there is a linear region, which extension depends on the binary grating utilized. For the grating used this region proves to be around $5\,mm$ in an interval of approximately $1.5\,mm$. A close up to this linear region is shown in Fig. 6.5.

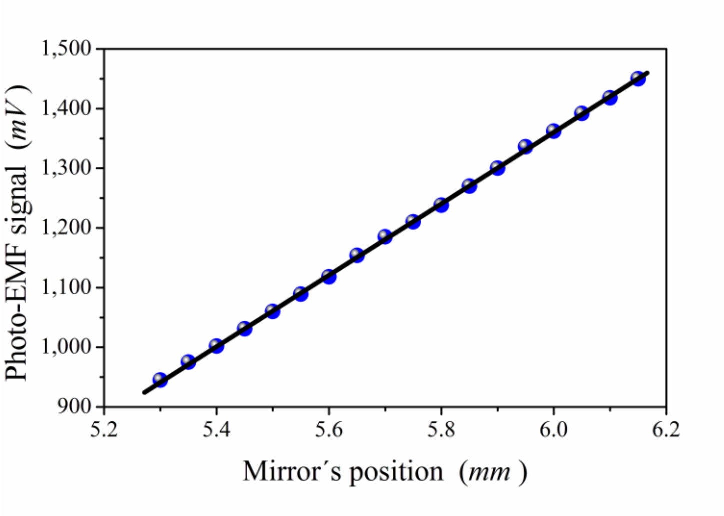

Fig. 6.5. The amplitude of photo-EMF signal as a function of the mirror's position. Here the wavelength $\lambda \approx 633\,nm$, the output power of $\approx 11\,mW$, with a frequency of $600\,Hz$, with amplitude of $11\,Vpp$, and the binary grating with a period of $\Lambda = 100\,\mu m$.

To test the resolution of the proposed system the signal was measured even between closer points. The limit in this case is the resolution of the screw of the translation stage, which was $10\,\mu m$. In the next figure is plotted the result:

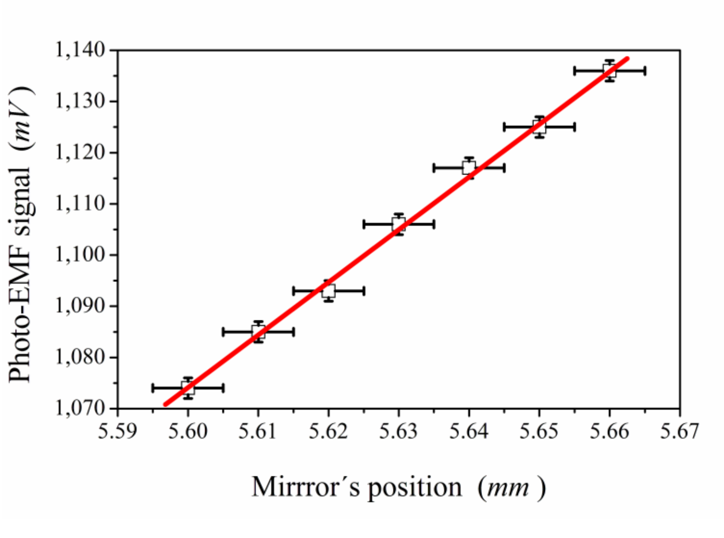

Fig. 6.6. The amplitude of photo-EMF signal as a function of the mirror's position. Here the wavelength $\lambda \approx 633\,nm$, the output power of $\approx 11\,mW$, with a frequency of $600\,Hz$, with amplitude of $11\,Vpp$, and the binary grating with a period of $\Lambda = 100\,\mu m$.

Note that main uncertainty in the plot corresponds to that of the translation stage, while the photo-EMF signal proved to be very stable (integration time $1s$). From these results one can state that the technique has a resolution higher than $10\,\mu m$. The proposed technique can be self-calibrated in terms of the Talbot distance.

The analysis can be simplified assuming that $J_0 >> J_S$ in Eq. 6.3, and that photo-EMF current is measured with a trans-impedance amplifier (amplifier that converts current to voltage) and an oscilloscope. In this case the photo-EMF current is given by:

$$J(z) = J_0^2 + 2J_0 J_S \cos\left(\frac{2\pi z}{z_T/4}\right) \qquad \textbf{(6.4)}$$

If J_0 (the DC term) is removed by an electronic filtering, if the operating point is set of on, and if the optical setup halfway between the maximum and minimum signal, then for displacements $z << z_T/4$:

$$J(z) \approx 16\pi\, J_0 J_S \left(\frac{z}{z_T}\right) \qquad \textbf{(6.5)}$$

from this equation the displacement of the target can be determined as:

$$z \approx J(z)\left[\frac{z_T}{16\pi\, J_0 J_S}\right] \qquad \textbf{(6.6)}$$

which is valid whenever $z << z_T/4$.

6.3 Discussion

Considering the experimental results (see Fig. 6.5 and Fig. 6.6), one can observe that the technique based on the adaptive photodetectors and the Talbot effect is suitable for effective distance measurements of a mirror-like target, if the aperture of the diaphragm is adjusted to produce a photo-EMF signal proportional to square of a sinusoidal function (as a function of the axial distance).

Comparing our technique with the method used in Ref. [11], one can verify that both systems are simple and the results are obtained in real time, but an important advantage of our technique is that there is not any image recording by a CCD-camera and a posterior signal processing.

From the experimental results (Fig. 6.6), one can state that the resolution of the technique (i.e. the minimal changes in contrast which can be detected by the system) is higher than 10 μm, and that in terms of the Talbot distance the technique can be self-calibrated. It means that photo-EMF technique is very sensitive to the small variations of distance.

6.4 References

---

[1] J. Lee, Y. J. Kim, K. Lee, S. Lee, and S. W. Kim, “Time-of-flight measurement with femtosecond light pulses”, Nature Photonics 4 (10), 716-720 (2010).

[2] K. Sasaki, H. Tsuritani, Y. Tsukamoto, and S. Iwatsubo, “Air-coupled ultrasonic time-of-flight measurement system using amplitude-modulated and phase inverted driving signal for accurate distance measurements”, IEICE Electronics Express 6 (21), 1516-1521 (2009).

[3] N. A. Riza, and S. A. Reza, “Noncontact distance sensor using signal processing”, Opt. Lett. 34 (4), 434-436 (2009).

[4] C. C. Jeng, C. H. Wu, C. Z. Li, and J. H, Chen, “Monitoring and dynamic control of distance and tilt angle measurements in micro-alignment instrument using an imaging approach”, Opt. Exp. 17 (17), 14722-14728 (2009).

[5] S. Le Floch, Y. Salvadé, M. Rostand, and F. Patrick, “Radio frequency controlled synthetic wavelength sweep for absolute distance measurement by optical interferometry”, Appl.Opt. IP 47 (16), 3027-3031 (2008).

[6] K. N. Joo, Y. Kim, S. W. Kim, “Distance measurements by combined method based on a femtosecond pulse laser”, Opt. Exp. 16 (24), 19799-19806 (2008).

[7] H. F. Talbot, “Facts relating to optical science No. IV”, Philos. Mag. 9, 401-407 (1836).

[8] P. Chavel P. and T. C. Strand, “Range measurement using Talbot diffraction imaging of gratings”, Appl. Opt. 26(3), 862-871 (1984).

[9] J. R. Leger and M. A. Snyder, “Real-time depth measurement and display using Fresnel diffraction and white-light processing”, Appl. Opt. 23, 1655-1670 (1984).

---

[10] B. F. Oreb and R. G. Dorsch, “Profilometry by phase-shifted Talbot images”, Appl. Opt. 33, 7955-7962 (1994).

[11] G. S. Spagnolo, D. Ambrosini, and D. Paoletti, “Displacement measurement using the Talbot effect with a Ronchi grating”, J. Opt. A: Pure Appl. Opt. 4, S376-S380 (2002).

[12] S. Teng, T. Zhou, and C. Cheng, “Influence of the size of the grating on Talbot effect”, Opt. Int. J. Light Electron. Opt. 119 (14), 695-699 (2008).

[13] J. W. Goodman, Introduction to Fourier Optics, McGraw-Hill international editions, 2nd ed., 1996.

Chapter 7

Conclusions

The use of non-steady-state photo-EMF effect for measuring the contrast distribution and its application as an adaptive detector for Talbot interferometry have been investigated both theoretically and experimentally. The main results of this investigation can be summarized as follows:

1) For the first time detailed theoretical analysis of non-steady-state photo-EMF current induced by arbitrary 1-D periodical light pattern using the model of monopolar photoconductor with a single impurity center was performed.

   - Analytical expression for complex amplitude of the photo-EMF current density generated by a periodical light pattern containing only the odd harmonics was obtained.
   - Two qualitatively different regimes were identified on non-steady-state photo-EMF effect depending on the relation between carriers' diffusion length and spatial frequency of the fundamental harmonic. For a case of large diffusion length $lKL_D >> 1$ the photo-EMF current is proportional to the sum of squares of the harmonics contrasts, that is, the fundamental harmonics contribution is the largest one. In the opposite case of small diffusion length $lKL_D << 1$ this last factor (square of harmonic contrast) is multiplied by the square of harmonic number, which means that the higher spatial harmonics are amplified.
   - Using the results of this analysis, the axial dependence of the photo-EMF current induced by the illumination patterns produced by the diffraction of light of a binary grating in the near field was studied.
   - The optimum regime for localization and analysis of Talbot self-images is when the detector response is proportional to square of the harmonics

contrasts, i.e. when the condition of large diffusion length (compared to the grating's fundamental spatial period) was met.

2) Theoretically predicted axial dependencies of photo-EMF current were observed at different experimental conditions using different *GaAs* detectors. The main results of the theoretical analysis for two limiting cases (large and small diffusion length) were confirmed experimentally.

3) The comparative analysis (theoretical and experimental) of the photo-EMF based-method against the conventional CCD-based methods (RMS and semivariogram techniques) for measuring contrast distribution and for localization of Talbot self-images was realized.

- The photo-EMF based detector potentially has shorter response time since it does no need image processing.
- The photo-EMF based detector possess higher sensitivity to the contrast variations, but it needs higher light intensity, while CCD can work efficiently at very low illumination levels (few μW).
- The photo-EMF detectors can be potentially used for analyzing the spectral content of periodical objects since the fine structure of axial distribution of contrast is better defined comparing with that of CCD-based methods.

4) The possibility of practical application of the adaptive photo-EMF detectors and the Talbot effect for effective distance measurements from a mirror-like target was demonstrated experimentally.

- The photo-EMF signal amplitude depends linearly on the displacement within a range of displacement $\approx z_T / 32$. The proposed method is self-calibrated in terms of Talbot distance.
- For our particular experimental scheme, the resolution of the photo-EMF technique was better than $10\mu m$ for a maximal displacement of $1mm$.